

**Improving Cranial Vault Remodeling for Unilateral Coronal Craniosynostosis –  
Introducing Automated Surgical Planning**

by

Emilie Robertson

A thesis submitted in partial fulfillment of the requirements for the degree of

**Master of Science**

in

Rehabilitation Science

Faculty of Rehabilitation Medicine  
University of Alberta

## **Abstract**

### **Background**

Craniosynostosis is a condition that occurs in about one in 1000 infants. Unicoronal craniosynostosis (UCS) is a common subtype of craniosynostosis that results in an abnormal head shape, and can lead to brain growth impairment, visual problems, and psychosocial disturbance. Surgery is the mainstay of treatment for UCS and involves removing the abnormal skull bones and reshaping them. Cranial vault remodeling (CVR) is an invasive and often lengthy procedure that can result in significant blood loss. It also involves surgeon guesswork in an effort to create a normal appearing skull. Virtual surgical planning (VSP) is becoming popular as a method to reduce the subjectivity of these procedures and potentially improve outcomes for patients. There is limited data comparing conventionally planned and virtually planned CVR surgeries. The lack of a reliable, easy to use, and objective method to measure the deformity in UCS may contribute to this paucity.

### **Objectives**

The goal of the research presented in this thesis was to improve surgical planning for UCS by developing a deformity index measure, investigating perceptions of the deformity in UCS, and developing a virtual surgical procedure that could be used to develop an automated VSP algorithm for CVR in UCS. These goals were addressed in three studies.

### **Methods**

3D Slicer, Geomagic FreeformPlus, Geomagic Control, and KeyShot were the software programs used. The deformity index in the first study was assessed using test-retest reliability. Chi-squared analysis and mixed methods regression model were used to analyze the perceptual

data in the second study. Hausdorff surface distances were used to assess the virtual workflows in the third study.

## **Results**

A novel, user-friendly deformity index was developed that was highly reliable (ICC = 0.93). Members of the general public were good at distinguishing between normal and abnormal skulls ( $\chi^2(1) = 281.97, p < 0.001$ ), and laypersons' responses were predicted by the deformity index in the perception study ( $b = -0.10, z = -2.6, p = 0.010, CI: [-0.18, -0.02]$ ). In the third study, two virtual fronto-orbital advancement workflows were developed that required varying degrees of surgeon participation. In both workflows, reconstruction skull models were created that were closer in shape to a normal skull than the preoperative skull.

## **Conclusion**

Several tools were developed that can be used by surgical teams to improve planning for CVR procedures for patients with UCS. A deformity index can be used to assess the severity of skull dysmorphology and quantify reconstruction outcomes. New data regarding the general public's perception of UCS deformity assists in developing a meaningful reconstruction target for surgical planning. Finally, virtual workflows can be a useful tool for surgical teams to prepare for complex operations and introducing automation into the surgical planning can reduce the subjectivity of CVR even further. Future work in this area will focus on using the partially automated surgical planning framework to develop a fully automatic computer algorithm to further enhance the planning procedure for this complex problem.

## Preface

This thesis is an original work by Dr. Emilie Robertson. The research presented in this thesis received research ethics approval from the University of Alberta Research Ethics Board, project name, “Virtual surgical planning in pediatric patients with unicoronal synostosis: Development and implementation of a computer-based optimization algorithm,” no. 85524, Sept 30, 2019, and project name, “Detecting skeletal deformities in unilateral coronal craniosynostosis – perceptions of the general public,” no. 85714, December 11, 2019.

The work presented in chapter two of this thesis is in the second round of revisions and has been re-submitted on March 11, 2020 as Robertson, E., Louie, G., Kwan, P., Boulanger, P., & Aalto, D., “Test-retest validation of a cranial deformity index in unilateral coronal craniosynostosis,” in *Computer Methods in Biomechanics and Biomedical Engineering*.

The work presented in chapter three of this thesis has been published as Robertson, E., Louie, G., Kwan, P., Boulanger, P., & Aalto, D., “Skeletal deformity in patients with unilateral coronal craniosynostosis - Perceptions of the general public,” in *Journal of Craniomaxillofacial Trauma and Reconstruction*, published online March 25, 2020 (<https://doi.org/10.1177/1943387520911873>). I was responsible for data collection, analysis, and manuscript preparation. G. Louie, P. Kwan, and P. Boulanger were involved in concept formation and manuscript revision. D. Aalto was the supervisory author and was involved in concept formation, data analysis, and manuscript composition.

## **Acknowledgements**

Firstly, thank you to Dr. Aalto for his supervision during this program. I am greatly appreciative for his unwavering encouragement and support throughout the research process. I learned a tremendous amount about research methodology, statistics, and surgical design under his supervision. His ability to lead with kindness, enthusiasm, and humour promoted a uniquely positive learning environment. Learning under his supervision was an extremely enjoyable and invaluable experience.

Thank you to Dr. Boulanger for co-supervising this thesis and providing very important insight from a computer science perspective. I never thought it would be impossible to pass, let alone understand and enjoy, a graduate level course in computing science without any background in the subject. Quite oppositely, I developed a passion for medical imaging science. His ability to apply and explain complex topics in computing science to a surgical problem was integral to the research presented in this thesis.

Thank you to Dr. Louie for being my clinical mentor and provider of sweet treats. Dr. Louie's ideas regarding the current practice of cranial vault reconstruction at the study institution were the motivation behind the presented research. Many after-work hours were spent with Dr. Louie going over research progress and reviewing surgical workflows for applicability to real life. Dr. Louie embodies the rare combination of an expert clinician, thoughtful researcher, and dedicated teacher. Understanding cranial vault reconstruction through operating room experiences and frequent discussions with Dr. Louie has been a highlight of this program.

Thank you to Dr. Kwan for his unique perspective as a clinician scientist with a computer engineering background. Dr. Kwan's insights clarified the research direction of my thesis and resulted in the development of a specific research career focus. His thoughtful questions and feedback stimulated the refinement of the presented work and ensuring results were applicable to both a technical and clinical audience. His in depth knowledge of both computer processes and surgical technique were instrumental in idea conception.

Thank you to Dr. Wilkes for his clinical and research mentorship in the beginning years of my residency. His encouragement and enthusiasm sparked my interest in the Surgical Design and Simulation program. The importance of surgical design work was realized while operating

with him, as well as the many discussions we had about the role of the Institute for Reconstructive Sciences in Medicine in his life and in the lives of his patients. I will cherish the time we spent operating together, and am grateful for the many research, clinical and life lessons I learned under his guidance.

I would also like to thank Gail Schaffler from the University of Alberta Department of Radiology for her assistance and countless hours spent de-identifying and copying imaging data for the studies in this thesis, and Dr. Nathaniel Maeda who has been instrumental in preparing the work presented in the third study for automation.

Thank you to the Covenant Health Research Centre for providing SEED Grant funding for this study (#13949).

## Table of Contents

<b>Abstract .....</b>	<b>ii</b>
<b>Preface .....</b>	<b>iv</b>
<b>Acknowledgements.....</b>	<b>v</b>
<b>Examining Committee .....</b>	<b>Error! Bookmark not defined.</b>
<b>Chapter 1: Introduction .....</b>	<b>1</b>
<b>1.1 Overview .....</b>	<b>1</b>
1.1.1 Outline of Studies.....	1
<b>1.2 Background.....</b>	<b>2</b>
1.2.1 Background of Condition .....	2
1.2.2 Involvement of Surgery.....	3
1.2.3 Surgical Challenges.....	4
1.2.4 Virtual Surgical Planning for Craniosynostosis Surgery.....	5
1.2.5 Analyzing Deformity and Outcome Measurements .....	5
1.2.6 Barriers to VSP in CVR.....	7
1.2.7 Using Computer Automation to Assist in Virtual Surgical Planning.....	8
1.2.8 Clinical Relevance .....	10
<b>1.3 Thesis objectives.....</b>	<b>11</b>
<b>Chapter 2: Validating a Novel Deformity Index .....</b>	<b>12</b>
<b>2.1 Abstract .....</b>	<b>12</b>
<b>2.2 Background.....</b>	<b>13</b>
<b>2.3 Objectives .....</b>	<b>16</b>
<b>2.4 Materials and Methods .....</b>	<b>16</b>
2.4.1 Participants .....	16
2.4.2 Design Considerations .....	17
2.4.3 Deformity Index Workflow Design.....	18
2.4.3.1 Alignment.....	18
2.4.3.2 Registration.....	19
2.4.3.3 Segmentation.....	20
2.4.3.4 Surface Distance Calculation .....	23
2.4.3.5 Confirmation.....	24
2.4.4 Reliability .....	24

<b>2.5 Results .....</b>	<b>25</b>
<b>2.6 Discussion .....</b>	<b>28</b>
2.6.1 Limitations.....	31
2.6.2 Future Direction .....	32
<b>2.7 Conclusion .....</b>	<b>32</b>
<b>Chapter 3: Perception Study.....</b>	<b>33</b>
<b>3.1 Abstract.....</b>	<b>33</b>
<b>3.2 Background.....</b>	<b>34</b>
<b>3.3 Objectives .....</b>	<b>34</b>
<b>3.4 Materials and Methods .....</b>	<b>35</b>
3.4.1 Participants .....	35
3.4.2 Experimental Design .....	37
3.4.3 Surface Distance Measurement.....	39
3.4.4 Analysis .....	40
<b>3.5 Results .....</b>	<b>41</b>
<b>3.6 Discussion .....</b>	<b>42</b>
3.6.1 Limitations.....	43
3.6.2 Future Direction .....	44
<b>3.7 Conclusions.....</b>	<b>44</b>
<b>Chapter 4: Computer Automation in Surgical Planning .....</b>	<b>45</b>
<b>4.1 Abstract.....</b>	<b>45</b>
<b>4.2 Background.....</b>	<b>47</b>
<b>4.3 Objectives .....</b>	<b>49</b>
<b>4.4 Materials and Methods .....</b>	<b>49</b>
4.4.1 Participants .....	50
4.4.2 Manual Workflow Design .....	50
4.4.2.1 Step 1: Importing Skull Models .....	50
4.4.2.2 Step 2: Isolating the SOB.....	51
4.4.2.3 Step 3: Isolating the Frontal Bones .....	51
4.4.2.4 Step 4: Virtual Osteotomies.....	52
4.4.2.5 Step 5: Bone Manipulation .....	53
4.4.3 Partially Automated Workflow Design .....	54
4.4.3.1 Frontal Bone Region of Interest .....	55

4.4.3.2 Supra-Orbital Bar Region of Interest .....	57
4.4.3.3 Registration of Regions of Interest .....	60
4.4.4 Analysis .....	64
<b>4.5 Results .....</b>	<b>66</b>
4.5.1 Manual Workflow Design .....	66
4.5.2 Automated Workflow Design.....	67
<b>4.6 Discussion .....</b>	<b>73</b>
4.6.1 Limitations.....	79
4.6.2 Future Work.....	79
<b>4.7 Conclusion .....</b>	<b>80</b>
<b>Chapter 5: Conclusion.....</b>	<b>81</b>
<b>Thesis References .....</b>	<b>83</b>
<b>List of Tables .....</b>	<b>96</b>
Chapter 1.....	96
Chapter 2.....	97
Chapter 3.....	98
Chapter 4.....	100
<b>List of Figures .....</b>	<b>105</b>
Chapter 1.....	105
Chapter 2.....	106
Chapter 3.....	112
Chapter 4.....	115
<b>Appendices .....</b>	<b>131</b>
Appendix A: Glossary of Terms.....	131
Appendix B: Hausdorff Surface Distance Explanation .....	132

## Chapter 1: Introduction

### 1.1 Overview

The research in this thesis is presented in a study-based format. Chapter 1 is a general introduction to the topic of virtual surgical planning in craniosynostosis surgery. Subsequent chapters in this document outline the background, objectives, methods, results, discussions and summaries for the three studies. The first study is presented in Chapter 2, and outlines the development and validation of a deformity index to quantify frontal bone morphology in unicoronal synostosis (UCS). The second study is presented in Chapter 3, and outlines a public perception study, examining laypersons' perceptions of UCS deformity. The third and final study is presented in Chapter 4, and outlines the preliminary work for the development of an automated virtual surgical workflow.

#### 1.1.1 Outline of Studies

**Table 1.1** An outline of the studies presented in this thesis.

Chapter 2 – Study #1	<ul style="list-style-type: none"><li>• Development of deformity index workflow</li><li>• Using the novel workflow to quantify deformity in a series of UCS patients</li><li>• Test-retest reliability testing</li><li>• Case example: using workflow to quantify reconstruction success in pre and postoperative patient</li></ul>
Chapter 3 – Study #2	<ul style="list-style-type: none"><li>• Assessing general public's perceptions of skull deformity</li></ul>
Chapter 4 – Study #3	<ul style="list-style-type: none"><li>• Manual and partially automated virtual workflow development for CVR surgery for UCS</li></ul>

## 1.2 Background

### 1.2.1 Background of Condition

Craniosynostosis is a relatively common condition that occurs in infants, affecting up to 1 in 1000 live births (Tahiri et al., 2017). It occurs as a result of the premature fusion of the space that normally exists between the various bones that form an infant skull. Normally, these spaces do not start fusing until around six months of age. Left untreated, craniosynostosis can affect normal brain growth and development, cause visual impairment, and have a significant psychosocial impact on the child (Campbell & Derderian, 2014). Craniosynostosis can be divided into symmetric and asymmetric subtypes, the latter involving unilateral fusion of a cranial suture. The coronal suture separates the forehead from the rest of the skull (Figure 1).

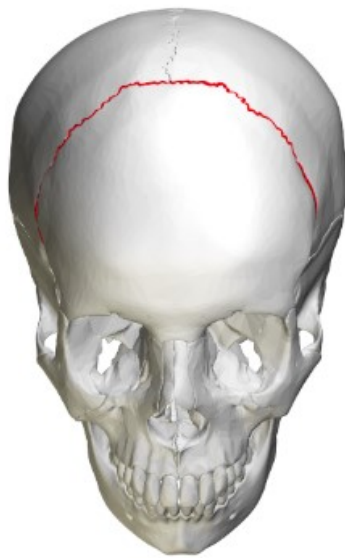


**Figure 1.1** The coronal suture is shown in red. Fusion of the suture on either the left or the right side of the skull leads to anterior plagiocephaly.

Unilateral coronal craniosynostosis (UCS) is the most common asymmetric subtype of craniosynostosis and is a result of the unilateral premature fusion of the coronal suture. This leads to anterior plagiocephaly, which is a phenotype of craniosynostosis characterized in part by flattening of the forehead on the affected side and bossing of the forehead on the contralateral side. UCS is especially difficult to treat due to the asymmetrical nature of the deformity (Alford, Derderian, & Smartt, 2018). UCS affects the frontal bones, which determine the contour of the

forehead, creating a deformity that is difficult to disguise and has a significant impact on aesthetic appearance (Collett et al., 2013).

### ***1.2.2 Involvement of Surgery***

The mainstay of treatment for UCS is surgery. There are minimally invasive and invasive surgical treatment options (Alford et al., 2018). Endoscopic strip craniectomy with helmet therapy, spring-assisted cranioplasty, and distraction osteogenesis are examples of minimally invasive procedures to treat UCS. However, these procedures lack the long-term data that supports their use universally over total cranial vault remodeling. Cranial vault remodeling (CVR) surgery has been the primary method of correcting the forehead deformity resulting from UCS (Alford et al., 2018). CVR involves removing components of the affected skull, reshaping the bones, and securing them back in place in a configuration that gives the skull a more normal shape. Fronto-orbital advancement (FOA) is the specific technique of CVR typically used in the treatment of UCS. FOA surgery involves two components: 1) shaping the supra-orbital bar (SOB), and b) re-contouring the forehead. Figure 2 depicts these areas.

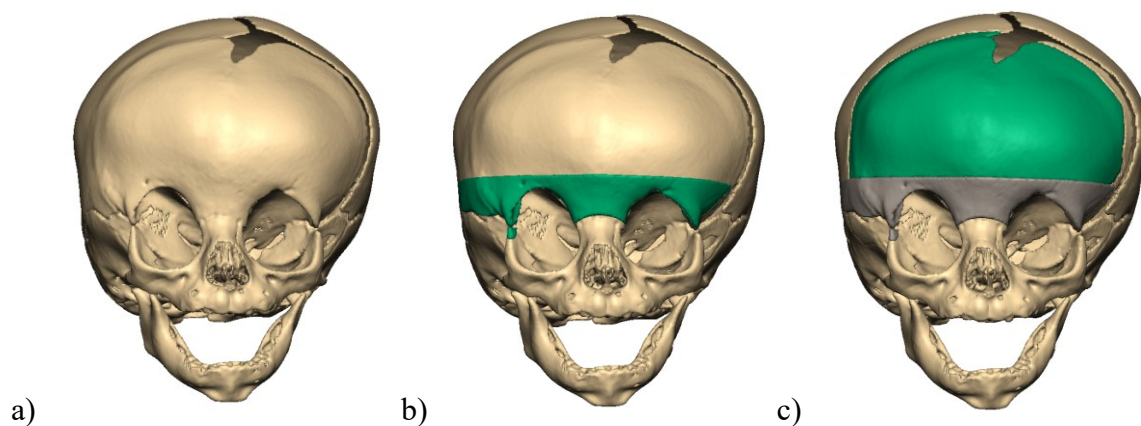


**Figure 1.2** A) Three-dimensional (3D) model of an infant with right-sided UCS. The right coronal suture is fused as demonstrated by the presence of a bony ridge when compared to the left coronal suture that is patent and depicted as an open space. B) The supra-orbital bar region is highlighted in green. This is the area that is above the eye sockets. C) The supra-orbital bar is shown in grey, and the frontal bones that constitute the forehead region are highlighted in green.

In FOA surgery, the SOB and the frontal bones are removed from the anesthetized infant's skull in the operating theatre. The SOB is reshaped to a normal contour and secured back on the infant with absorbable plates and screws. Next, the frontal bones are reshaped, rotated, interchanged, and/or bent in order to achieve a normal forehead appearance, and again secured back on the infant's skull (Vander Sloten, Degryse, Gobin, Van der Perre, & Mommaerts, 1996).

One of the main goals of the surgery is to create a forehead appearance that is closer in shape to a normal skull when compared to the patient's preoperative forehead appearance. CVR surgeries are lengthy procedures and the potential complications are significant, with massive blood loss being the most common cause of intra-operative morbidity and mortality (Lee et al., 2012). In addition, there are vital structures such as the dural sinuses that are at risk of injury (Fisher, Medina, Bojovic, Ahn, & Dorafshar, 2016).

### ***1.2.3 Surgical Challenges***

The goal of CVR surgery for patients with UCS is to transform a 3D shape (the patient's preoperative skull) into a more symmetric 3D shape (postoperative skull) with the same material (bone). Therefore, the procedure relies on surgeon guesswork, experience, and trial and error, in an effort to create a normal-appearing skull. This subjective process is known as the "fitting and chipping" phenomenon, and definitive analysis of the bone shapes can only be made once the bones are irreversibly cut (Vander Sloten et al., 1996). The surgical steps in CVR can be difficult to visualize, and the benefits of surgical planning in complex craniofacial cases were realized many years ago.

The introduction of high-resolution computed tomography (CT) scanning with the ability to produce 3D skull surface models, improved the ability to visualize craniofacial deformities and the surgical steps to correct them (Vannier, 1983). Zonneveld summarizes the introduction of physical 3D models in the early 1980s to address challenging clinical scenarios (1994). Kobayashi, Fujino, Nakajima, and Chiyokura (1993) described pre-surgical planning for craniofacial surgery using such 3D printed skull models. The authors address the downsides of this method, which include the high cost of materials and the time-consuming planning process (Kobayashi et al., 1993). A recent study investigated the benefit of a physical 3D model in the CVR planning process and found it was a helpful adjunct for parent education, but did not reduce the operation length (van Nunen, Janssen, Stubenitsky, Han, & Muradin, 2014). Cutting, Grayson, Bookstein, Fellingham, and McCarthy (1986) compared the use of physical models and virtual, computer models for surgical planning of craniofacial surgery, and concluded that virtual simulation was a superior method for surgical planning due to the decreased cost and the ability to generate quantitative anthropometric value. This is consistent with the current trend of surgical planning for craniostyosis, and the increasing use of virtual surgical planning for this application.

#### ***1.2.4 Virtual Surgical Planning for Craniosynostosis Surgery***

The use of virtual surgical planning (VSP) has been increasing for craniosynostosis reconstruction surgery. By allowing surgeons to pre-plan CVR operations virtually, VSP decreases intra-operative procedure length, reduces the subjectivity of the reconstructive planning process, and yields aesthetic reconstruction results. Vander Sloten et al. (1996) introduced the concept of virtually planning CVR surgery using a mathematical computer model. Since then, several centers have documented their positive experience with the use of computer-assisted design and computer-assisted manufacturing (CAD/CAM) technologies to assist surgical planning, specifically as it pertains to CVR surgery.

Kechoyan et al. (2014) used a pre-fabricated SOB template, derived from normative skull data, to decrease operation length and increase reconstruction accuracy in their study looking at the treatment of metopic craniosynostosis. Chim et al. (2014) describe their experience using VSP to plan CVR surgery, as well as for distraction osteogenesis cases, claiming the advantages include more accurate surgical results, as well as a better understanding of the surgical procedure by the patients' families. Queiros et al. (2017) used VSP to design custom cutting and plating guides to assist in craniofacial reconstruction for adult patients with secondary deformity after craniosynostosis surgery. They objectively demonstrated the high level of accuracy achieved using custom guides to execute the surgical plan (Queiros et al., 2017). Seruya, Borsuk, Khalifian, Carson, Dalesio, and Dorafshar (2013) describe their use of VSP for a series of CVR cases, highlighting additional advantages of this technology include the educational benefits to junior craniofacial surgeons and learners, and the potential to reduce the "fitting and chipping" phenomenon previously attributed to CVR surgery.

#### ***1.2.5 Analyzing Deformity and Outcome Measurements***

With the increased use of CAD/CAM technologies for VSP, the ability to measure surgical outcomes is an important component of assessing the benefit of using advanced technologies and comparing available software and hardware. However, the drawbacks of current methods used for outcome measurement in cranial vault remodeling are that they are subjective, inconsistently reported, require expert skills in image processing, or provide limited information.

Whitaker, Pashayan, and Reichman (1981) made the first attempts to develop a grading system for craniosynostosis. The Whitaker scale is based on surgeons' subjective perception of a patient's deformity following a photographic assessment. Although this scale is still prevalent in recent publications (Taylor et al., 2015), its simplicity comes with limitations. Wes et al. (2017) recently studied the Whitaker scale's utility and found that it does not consistently predict the need for treatment and that its inter-rater reliability is low ( $\kappa = 0.1567$ ). In addition, surgeons are often rating their own patients, potentially biasing the outcome measurement. Regardless, in the absence of an objective, quantitative measurement scale, the Whitaker scale continues to be widely used to report outcome measures in craniosynostosis literature. For example, a recent large series review of over 200 cases of UCS reported outcomes using the Whitaker scale (Taylor et al., 2015). The authors of this study comment on the scale's inherent subjectivity and its inability to produce results that can be meaningfully compared across institutions.

Photographic assessment is another common tool used instead of an objective outcome measure. Chim et al. (2014) presented a case series of novel uses of VSP in CVR. They used preoperative and postoperative photos to present their results, without the use of a standardized measurement system. Soleman, Thieringer, Beinemann, Kunz, and Guzman (2015) presented a similar case series, again using patient photos to display outcomes with no standardized measurements used. Fisher et al. (2016) and Mardini, Alsubaei, Cayci, Chim, and Wetjen (2014) use the same method to report results.

There have been several objective measuring techniques that have been developed. However, there is no one tool that is used consistently. A review of the craniosynostosis literature from the past 25 years revealed 24 articles using inconsistent measures of reporting outcomes (Alford et al., 2018). Only seven of the studies reported outcomes in a quantitative manner, the majority of which used cephalometric and volume measurements calculated from CT scan data. The authors highlight the need for consistent outcomes reporting in the craniosynostosis literature, pointing out that even among the studies that use standard anatomic measurements, rarely are the same measurements reported (Alford et al., 2018).

A potential cause for the variability of reported objective outcome measures is their technical difficulty. Selber, Brooks, Kurichi, Temmen, Sonnad, and Whitaker (2008) comment on the measurement challenges associated with techniques such as cephalometrics and

morphometrics when quantifying craniofacial deformity, potentially leading to their limited use. Queiros et al. (2017) briefly mention their method of measuring outcomes in their series of patients undergoing revision surgery for craniosynostosis. The authors consulted a Ph.D. student studying medical image analysis, who measured the minimum distance between the planned 3D model and the postoperative CT scan. While this presented a novel way of quantitatively measuring outcomes in CVR, the measurements were outsourced to a specialist outside the field and required the use of several software programs. This raises concern about the user-friendliness and reproducibility of this method by other centers.

Khechoyan et al. (2014) introduced the concept of “area under the curve” (AUC) as a quantitative outcome measure in CVR surgeries. Again, this presented a novel method of quantifying postoperative results in comparison to the preoperative skeletal deformity. Unlike some of the procedures mentioned above, the AUC measurement is simple to calculate and intuitively demonstrates an improvement in skull shape. However, CVR involves reshaping the patients’ frontal bones and the SOB, the two skull components that make up the forehead. AUC is limited to measuring the difference between the pre and postoperative SOB only, and provides no information about the postoperative position of the frontal bones.

While there have been many advances in VSP technology for CVR, there is still a need for a reliable, user-friendly, objective outcome measurement procedure. Existing methods do not meet these criteria, and may explain the persistent inconsistency in how outcome measures are reported in this field. In the absence of a novel method, the ability to draw conclusions about the advantages of VSP, and to compare between different planning and surgical techniques, is limited.

### ***1.2.6 Barriers to VSP in CVR***

The technologies involved in VSP are expensive. One group recently quoted the cost of VSP in their study to be 4500 to 6000 American dollars per case, highlighting the potential expense associated with advanced technologies (Soleman et al., 2015). The costs associated with VSP include paid planning time between biomedical engineers and surgeons, computer software costs, and the cost of additive manufacturing of surgical guides (Chim et al., 2014; LoPresti, Daniels, Buchanan, Monson, & Lam, 2017; Mardini et al., 2014). The costs of employing CAD/CAM technology in CVR can be reduced by using locally manufactured cutting guides, for

example, as demonstrated by Burge et al. (2011). In their study, the SOB template was manufactured by the engineering department at the University of Toronto for a cost of 750 Canadian dollars per template (Burge et al., 2011).

Another barrier that may limit the use of VSP is the time associated with preoperative planning. Fisher et al. (2016) highlight that the use of VSP for CVR surgery is often a collaborative effort between surgeons and third party engineers. In their study, planning time ranged from 20 to 60 minutes per session, with some procedures requiring multiple sessions (Fisher et al., 2016). On the other hand, Soleman et al. (2015) did not outsource any VSP components, and their planning workflow took an estimated one to two days for completion. As such, there is a time conserving benefit of outsourcing the production of surgical guides and collaborating with engineers for surgical planning. Still, these may be outweighed by the cost associated with it.

Lopresti et al. (2017) highlight that the number of centers offering VSP for craniosynostosis is small, despite all of the potential advantages previously mentioned and reported in the literature. This suggests that the barriers to utilizing VSP for CVR may prevent its use. This may limit the use of this technology to patients who live near a tertiary center offering this technology (LoPresti et al., 2017). Introducing computer automation to VSP for CVR may present a novel solution to overcoming the time and cost barriers of employing advanced technology in surgical planning.

### ***1.2.7 Using Computer Automation to Assist in Virtual Surgical Planning***

Porras, Zukic, Equobahrie, Rogers, and Linguraru (2016) introduced the concept of computer automation in VSP for CVR. They demonstrated that by registering a patient's preoperative CT scan to a normative skull statistical model, and by defining a set of physical constraints, an algorithm could be developed to produce an automatic surgical plan that would approximate a normal skull shape in series of patients with metopic craniosynostosis. The automated plans derived in their study objectively reduced the degree of malformation in all 11 patients (Porras et al., 2016). A computer-automated plan could reduce planning time, prevent the need for collaboration with third-party engineers, and as a result, reduce the overall cost of VSP for CVR.

Automatically generated surgical plans have the added potential benefit of reducing the subjectivity of surgical decision making in CVR. The surgical correction of UCS is especially challenging due to the asymmetry in the orbits, cranial base, cranium, and face (Alford et al., 2018). A computer algorithm has the ability to plan a reconstruction based on parameters that can be measured objectively and accurately. This reduces the need for manual human input in the planning process and reduces the subjectivity of the surgical decisions (Porras et al., 2016). The desire to reduce the subjectivity in surgical decision making for FOA procedures has been cited as the motivation behind using surgical guides and templates at various centers. Khechoyan et al. (2014) developed SOB templates based on normative skull data to treat patients with metopic and coronal craniosynostosis. Chim, Wetjen, and Mardini (2014) describe their use of CAD/CAM technology to virtually plan craniosynostosis surgeries and print custom cutting and plating guides to reduce the “highly subjective nature” of the procedures, and to reduce the variability in outcomes. Due to the subjective nature of freehand FOA surgical planning, there is a lot of variability in the orbit and forehead reconstruction results in patients with UCS, and a high relapse rate (Soleman et al., 2015). Virtual planning reduces surgical subjectivity with the availability of normal reference skulls to compare virtual plans. However, members of a surgical and engineering team are still guiding the decision-making process for the plan, maintaining a significant degree of subjectivity. Essentially, the “fitting and chipping” phenomenon is moved from the operating room to the virtual environment. Computer automation can reduce the human input in surgical planning and eliminate the guesswork that is attributed to CVR (Porras et al., 2016).

While Porras et al. (2016) demonstrated the potential role of computer automation in VSP for CVR, there are some factors that limit the use of their proposed method to the metopic craniosynostosis population. For example, their algorithm does not allow for the exchange of frontal bones from one side to the other. Exchanging bone from one side to another is a common technique used at the study institution in CVR for UCS to achieve the desired shape. In addition, the algorithm has not yet been applied in a clinical setting, and at this stage represents a possible solution to overcoming barriers of VSP.

### ***1.2.8 Clinical Relevance***

There are many benefits to using VSP and CAD/CAM technology in CVR for patients with craniosynostosis, including reducing the subjectivity of surgical decision making, decreased operation duration, and improved patient and parent education. These benefits may be especially relevant in cases of UCS where asymmetry increases the complexity of surgical reconstruction. Despite these advantages, the primary barriers to the use of VSP for CVR are cost and time consumption. In addition, the lack of a consistently used, objective, and user-friendly deformity measurement process limits the ability to make meaningful comparisons between different planning techniques, and to answer questions regarding the cost-benefit analyses of advanced technologies. Cost-effective and time-efficient methods to employ VSP in CVR might expand its use to multiple centers, allowing more patients with craniosynostosis to reap the benefits of virtual planning. The introduction of computer automation in the VSP process has recently shown to be a potential solution to overcoming barriers of VSP. In addition, automation can reduce the subjectivity of CVR and potentially improve the consistency of surgical outcomes. Ultimately, improved surgical planning techniques have the potential to reduce surgery length, improve surgical accuracy, and decrease surgical complications.

## **1.3 Thesis objectives**

### **Chapter 1**

The first chapter provided an overview of UCS, the surgical treatment for UCS, and the role of VSP in CVR. Gaps in the literature are highlighted and addressed in subsequent chapters.

### **Chapter 2**

Chapter two details the development of a novel deformity index workflow. The primary objective of this study was to develop a step-wise, user-friendly, and accessible workflow to enable clinicians to assess cranial vault morphology in UCS patients quantitatively. Secondary objectives were to assess the reliability of the index, and to demonstrate how the index could be used in an alternative way to quantify reconstruction outcomes.

### **Chapter 3**

The goal of this study was to determine if there is a relationship between an objective value of skull deformity and laypersons' perceptions of skull appearances. Additional objectives were to determine if there were other factors influencing peoples' ratings of skull appearance, as well as to determine if there is a threshold value whereby members of the general public are unable to decipher the difference between a normal and a UCS skull. The primary interest in this study was to simulate and investigate a first impression scenario, thus mimicking a common situation where rapid judgments are made regarding peoples' appearances.

### **Chapter 4**

The concept of automating surgical planning is introduced in Chapter four. The objective of the third study was to develop two virtual surgical planning workflows. The first workflow was developed as a virtual tool for surgeons to plan CVR surgeries prior to the operation. The second virtual workflow was developed with automatic steps introduced in order to create a conceptual framework for the future development of a fully automatic surgical planning algorithm.

## **Chapter 2: Validating a Novel Deformity Index**

### **2.1 Abstract**

#### **Background**

Unilateral coronal craniosynostosis (UCS) affects many infants resulting in abnormalities of the forehead and orbits. As a result, the deformity caused by UCS is very noticeable and there are several surgical treatment options available to normalize the head shape. However, there is a lack of consistently used outcome measures, resulting in difficulty assessing surgical outcomes and on-going debate over optimal treatments. Current techniques to quantify deformity in UCS are cumbersome, provide limited information, or are based on subjective assessments.

#### **Methods**

In this study, a cranial deformity index was developed to quantify abnormality at the frontal bones for UCS that is accessible, user-friendly, and generates objective surface distance measurements. The cranial deformity index is defined as the Euclidean distance at the point of the largest deviation between a deformed skull and a normal reference skull. In addition, the index was successfully used to quantify postoperative changes in a single case of UCS that underwent corrective surgery.

#### **Results**

The reproducibility of the index was assessed using test-retest reliability and was demonstrated to be highly reproducible (ICC = 0.93).

#### **Conclusion**

A user-friendly measurement index that is based on open-source software may be a valuable tool for surgical teams. In addition, this information can augment the consultation experience for patients and their families.

## 2.2 Background

Craniosynostosis is a relatively common condition affecting up to 1 in 1000 live births (Robins et al., 2020). It occurs as a result of the premature fusion of one or more cranial sutures, which are the spaces that normally exist between the bones that form an infant skull. The premature fusion of cranial sutures leads to abnormal skull growth. Infants with craniosynostosis are typically diagnosed with the condition in the first few months of life as a result of an abnormal head shape. If left untreated, craniosynostosis can affect normal brain growth and development, cause visual impairment, and have a significant psychosocial impact on the child (Tahiri et al., 2017). Unilateral coronal synostosis (UCS) is a common subtype of craniosynostosis that is especially difficult to treat due to the asymmetrical nature of the deformity (Alford et al., 2018). This subtype affects the frontal bones that comprise the forehead, creating a noticeable deformity that has a significant impact on aesthetic appearance. There are multiple different surgical interventions to correct UCS deformities, with on-going debate over the superior method (Alford et al., 2018; Fearon, 2014; Tahiri et al., 2017). Cranial vault remodeling (CVR) is one surgical option to correct craniosynostosis deformities. It involves removing portions of an infant's skull, reshaping the abnormal bones, and fixating them back on using plates and screws, for example.

One of the primary goals of treatment for UCS is to correct the noticeable head shape deformity by improving forehead symmetry. Therefore, quantifying the patient's cranial vault shape is important. Geometrical outcomes are an important component of assessing the benefit and risk of surgical procedures. However, there is currently a lack of a consistent method to quantify cranial morphology in UCS, and therefore to measure outcomes for craniosynostosis corrective surgeries, contributing to the debate over surgery selection. The fact that many outcome measures rely on subjective assessments of deformity likely contributes to this variability. Whitaker et al. (1981) made the first attempts to develop a grading system for craniosynostosis. The purpose of this scale was to determine if the patients' aesthetic results were satisfactory or if they would require another corrective procedure. The Whitaker scale is based on surgeons' subjective perspective of a patient's deformity. Although this scale is still prevalent in recent publications, its simplicity comes with limitations (Taylor et al., 2015). Wes et al. (2017) recently studied the Whitaker scale's utility and found that it does not consistently predict the need for treatment and that its inter-rater reliability is low ( $\kappa = 0.16$ ). Photographic

assessment is another standard tool used instead of an objective measure. Multiple centers report their experience with craniostyostosis surgery using preoperative and postoperative photos to demonstrate the improvement in head shape (Chim et al., 2014; Fisher et al., 2016; Mardini et al., 2014; Soleman et al., 2015).

Several objective measuring techniques have been described; however, no single approach to quantify cranial shape has been used consistently. A review of the craniostyostosis literature from the past 25 years revealed 24 articles using a variety of different measures of reporting outcomes (Alford et al., 2018). Only seven of the studies quantitatively reported outcomes, the majority of which used cephalometric and volume measurements calculated from computed tomography (CT) scan data. The authors highlight the need for consistent outcomes reporting in the craniostyostosis literature, pointing out that even among the studies that use standard anatomic measurements, rarely are the same measurements reported.

A potential cause for the variability of reported objective, geometric measures is that they are time-consuming and/or require the assistance of computer software experts. Selber et al. (2008) comment on the measurement challenges associated with techniques such as cephalometrics and morphometrics when quantifying craniofacial deformity, potentially leading to their limited use. In addition, several methods have been described to quantify changes in specific components of a UCS skull. For example, Liu et al. (2019) describe their landmark-based method to measure bandeau shape, craniofacial twist, and orbital morphology on CT scans. While their solution provides precise information regarding these parameters, it relies on a series of manual measurements. Other authors describe their method of obtaining craniometric measurements at the cranial base and forehead (Mazzaferro et al., 2017; Yang et al., 2018). Similarly, Masserano et al. (2017) describe their method of manually quantifying postoperative differences in the temporal region of postoperative UCS patients (2018). Other authors looking at postoperative changes in UCS again used manual, CT scan landmark-based measurements to quantify changes in the orbital region after UCS correction surgery (Beckett et al., 2013; Yu et al., 2020), nasal root deviation (Wes, Mazzaferro, et al., 2017), and brow position (Xu et al., 2017). All of these methods rely on landmark-based measurements taken in single planes with unknown reliability. Visualizing the global cranial vault changes when measurements are reported this way can be more challenging. Queiros et al. (2017) briefly mention their method of

measuring outcomes in their series of patients undergoing revision surgery for craniosynostosis. This technique required expert consultation from a graduate student studying ‘Imaging’ as well as the use of several specialized software programs. This raises concerns about the user-friendliness and reproducibility of this method by other centers with limited access to imaging specialists.

The concept of “Area Under the Curve” (AUC) as a method to quantify forehead shape after metopic craniosynostosis surgery was introduced by Khechoyan et al. (2014). AUC was used to measure geometric outcomes following surgery by calculating the difference in shape between an abnormal skull and a normal reference skull at the inferior portion of the forehead. A skull with a small AUC had a more normal geometry compared to a skull with a large AUC, indicating a postoperative appearance that was more satisfactory. Again, this presented a novel method of quantifying postoperative results in comparison to the preoperative skeletal deformity. Unlike some of the techniques mentioned previously, the AUC measurement is simple to calculate and intuitively demonstrates an improvement in skull shape. However, CVR typically involves reshaping the patients’ frontal bones and supra-orbital bar (SOB), the two skull components that make up the forehead. AUC is limited to measuring the difference between the pre and postoperative SOB only, providing no information about the postoperative position of the frontal bones.

Technological advancements in image analysis and computational methods have allowed for precise craniomorphometric techniques that are partially or fully automated, alleviating the need for tedious manual measurements. The use of statistical shape models as a comparison group for craniosynostosis skulls has allowed for very accurate and reliable head shape analysis (Mendoza et al., 2014; Porras et al., 2016, 2018, 2019; Tu et al., 2019; Wood et al., 2016). These methods rely on the availability or development of a statistical model, which requires an atlas of normative head shapes. The use of specialized technology is a potential deterrent for clinicians without established collaborations with imaging experts, resources to build a multi-atlas, and who may be unfamiliar with the necessary algorithms and image analysis software.

Quantifying cranial vault morphology in craniosynostosis is challenging. The typical phenotype associated with UCS poses additional challenges due to the asymmetric nature of the deformity. As outlined by previous authors, multiple anatomic regions of the affected skull are

dysmorphic (Beckett et al., 2013; Liu et al., 2019; Masserano et al., 2018). What has remained a primary goal for CVR surgery is improvement of the contour of the frontal bones to create a less noticeable forehead deformity in affected patients. The forehead deformity in UCS is a visually salient feature (Robertson et al., 2020). Therefore, a method to quantify cranial vault morphology that focuses on the contour and position of the frontal bones is clinically important, and has been the focus of described methods (Porras et al., 2018, 2019; Wood et al., 2016; Yang et al., 2018). While there have been many advances in the measurement of craniosynostosis deformities, there is still a need for a reliable and user-friendly measurement procedure to quantify the frontal bone deformity in UCS. Existing methods do not meet all of these criteria, and may explain the persistent inconsistency in how outcome measures are reported in this field.

### **2.3 Objectives**

The primary objective of this study was to develop a step-wise, user-friendly, and accessible measurement index workflow to enable clinicians to assess cranial vault morphology in UCS patients quantitatively. Secondary objectives were to assess the reliability of the index and to demonstrate how the index could be used in an alternative way to quantify reconstruction outcomes.

### **2.4 Materials and Methods**

#### ***2.4.1 Participants***

After institutional review board approval (Pro85524), CT head and/or facial bone scans were retrieved from a provincial diagnostic imaging database. Two sets of data were retrospectively obtained. The experimental group consisted of CT scans from infants with UCS. The control group consisted of CT scans from age and sex-matched controls. All of the images used were from preoperative CT scans. Participants whose age at the time of the scan differed by no more than 30 days were considered age-matched. The search strategy was narrowed to the type of image (CT), anatomic location (facial bones/head), and age of the patient ( $\leq 24$  months) to identify scans. For the experimental group, patients that had a single fused coronal suture visible on the 3D reconstruction image were identified, and the diagnosis of UCS was verified with the radiologist report. Participants were excluded if they had syndromic craniosynostosis, multisuture craniosynostosis, skull fractures, or other craniofacial skull abnormalities (i.e. fibrous dysplasia). Common dysmorphic features associated with syndromic UCS, specifically

hypertelorism and midface hypoplasia, were used to identify potential syndromic cases, and cross-referenced with the radiology report. There were no cases of syndromic UCS identified in this study. The control group consisted of infants with normal skull morphology. The average field of view for all scans was 183 mm (SD = 18.7). All of the CT scans used had been helically acquired and reconstructed to 0.6 mm contiguous slices, with the exception of one scan from an older patient (14 months) that was reconstructed to 1 mm slices.

A single case feasibility design was used to pilot the workflow. The workflow was designed using the open-access software 3D Slicer (Version 11.0) (Fedorov et al., 2012). CT scans from a three-month-old female with right-sided UCS and a three-month-old female with normal skull morphology were used. The control skull was the only manipulated image in the workflow to reduce the possibility of artificially exaggerating or muting the deformity in the experimental skull.

#### ***2.4.2 Design Considerations***

Clearly defined design features with justifications are an essential component of computer-assisted design in the medical field to promote future improvements (Burton et al., 2018). The three design criteria selected for the deformity index workflow were user-friendliness, accessibility, and objectivity. Usability in this study was defined as a procedure that a clinician could reasonably execute without additional technical support. This criterion was deemed necessary in order to maximize surgeon engagement with the workflow. The second criterion was accessibility and is a critical component to consider especially when working within the constraints of a publicly funded healthcare system. Open-source software was used to meet the accessibility criterion, a practice that is growing in popularity (Barbero-García et al., 2017; Salazar-Gamarra et al., 2016). Objectivity was the third design element that was incorporated into the workflow. Quantitative values are important in order to draw conclusions about skull geometry and may be more sensitive to subtle changes when compared to qualitative assessment alone. Maximum Hausdorff surface distances in millimeters (mm) were used as the objective measurements in the workflow (Huttenlocher et al., 1993).

### ***2.4.3 Deformity Index Workflow Design***

A five-step measurement index workflow was developed that met all of the design criteria. These steps included alignment, registration, segmentation, surface distance calculation, and confirmation, in that order. A combination of manual and automatic steps are involved, as well as qualitative and quantitative assessment.

#### **2.4.3.1 Alignment**

The UCS and matched control CT scans are imported into 3D Slicer. Using the transforms function, the images are manually aligned in all three dimensions of translation and rotation (anterior-posterior, superior-inferior, right-left). The control skull is assigned as the ‘moving image’ for the alignment and the registration steps. Figure 1 shows the axial, sagittal, and coronal views of the UCS and normal CT scans as they import in 3D Slicer. In panel A, the two images are superimposed. The first step is to translate the skulls in the super-inferior plane, as demonstrated from panel A to panel B. Helpful landmarks for this alignment are the sella turcica and the orbital roof on the non-synostotic side. Next, the normal skull is translated in the anterior-posterior plane to align the contours of the frontal bones. The nasofrontal angle and sella turcica are useful landmarks in the sagittal view to align the cranial vault. Following this step, the normal skull is rotated in the horizontal plane to bring the metopic sutures, as viewed on the axial image, into a parallel relationship. In panels C and D, a dashed white line bisecting the frontal bone at the metopic suture on each skull demonstrates this improvement. After this, the normal skull is translated again in the right-left dimension to align the frontal bones at the metopic suture.

The deformity index is a calculation derived from the discrepancy at the frontal bones between a UCS and a normal skull. For this reason, the goal of the manual alignment step is to have the non-synostotic frontal bones line up on the axial and sagittal views as best as possible. Additional rotational and translational adjustments in the dimensions mentioned above can be used as necessary to achieve this goal before progressing to the subsequent registration step.

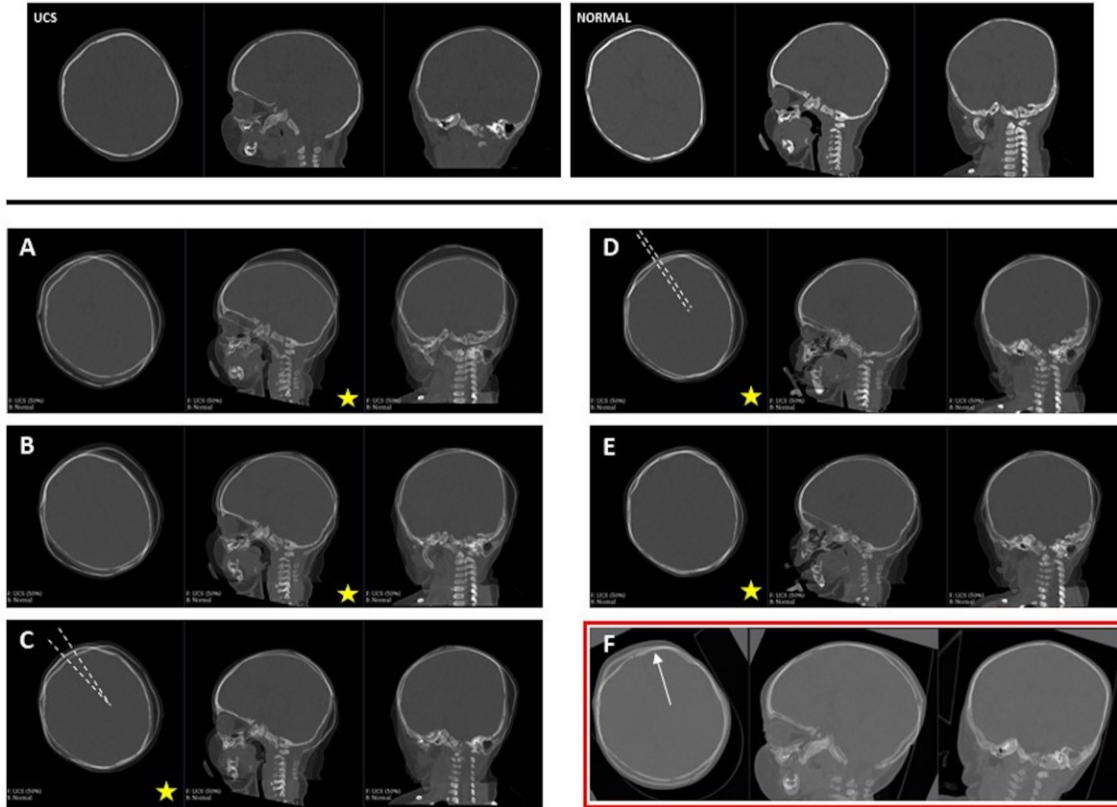


**Figure 2.1** CT scans are imported into 3D Slicer with axial, sagittal, and coronal views visible (top row). Panels A to E demonstrate the manual alignment process. The star indicates which view the described changes are best visualized. From A to B, the anterior cranial vault and the sella turcica are aligned with an inferior translation, as best viewed on the sagittal view. From B to C, the frontal bone contours are aligned with an anterior translation, again best viewed on the sagittal view. In panel C, a line that bisects the frontal bones of each skull is imagined at the metopic suture in the axial view. The goal from steps C to D is to rotate the normal skull image in an axial plane so that these lines assume a parallel relationship. Then, the normal skull is translated in the left-right dimension to align the metopic sutures (D to E). Panel E demonstrates the end result of the manual alignment step. Panel F demonstrates the end result after the registration step. It is clear here that the non-synostotic frontal bones (patient's left in this case) align well (white arrow). A subjective assessment of good bony overlap of the non-synostotic frontal bones in the axial slices is the endpoint of the registration step in this workflow. Once registered, the discrepancy in the forehead region on the synostotic side between the two skulls is apparent.

### 2.4.3.2 Registration

The control skull is registered to the normal skull using the general BRAINS registration function. The alignment saved in the previous step is used as the initialization transform for the registration. A rigid registration with scaling function with seven degrees of freedom is selected in the drop-down list and executed. Affine registration was not used to avoid asymmetric deformation of the normal skull. Once registered, the discrepancy in the forehead region between the two skulls at the synostotic side is very apparent (Figure 1, panel F). If the frontal bones do not line up after this step, the initial alignment is repeated with the goal of improving the

alignment of the anterior cranial vault.

### 2.4.3.3 Segmentation

There are a number of features associated with the UCS deformity, one of which is the flattening of the forehead on the fused side. The goal of this step is to isolate the flattened area and automatically calculate the point of maximum deformity. This point will be located where there is the greatest distance between the UCS skull and the registered reference skull. On the side with the prematurely fused suture, the UCS forehead bone will appear flattened and positioned further back compared to the normal reference skull. If, based on a qualitative visual assessment, the two skulls line up well at the anterior cranial vault after the previous registration step, this point of maximum discrepancy between the two skulls at the forehead region will be apparent (Figure 2). First, bone is segmented from each scan using the thresholding function. Small bone irregularities and foreign objects such as endotracheal tubes and nasal prongs can be segmented out in this step using the ‘erase’ and ‘delete island’ functions. Once the whole skull is segmented from each image, the frontal bone on the synostotic (fused) side and the corresponding frontal bone on the control skull are segmented (Figure 2).

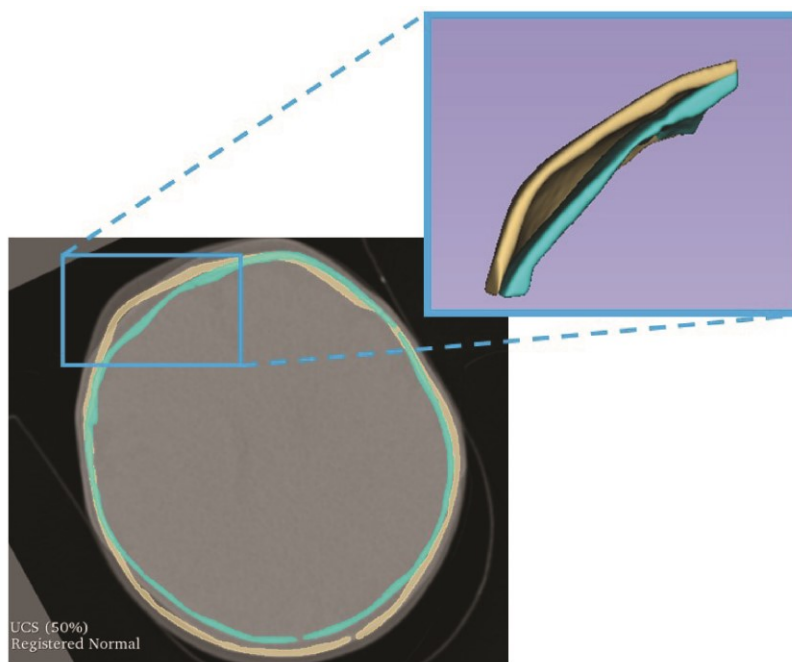


**Figure 2.2** In this image, the frontal bones corresponding to the synostotic side of the UCS skull are segmented. The blue skull is the UCS skull and the beige skull is the age and sex matched control skull. Surface models are generated representing the segmented frontal bones. The point

where there is the largest distance between the segments is automatically identified and the distance is calculated in subsequent steps. This represents the area where there is the largest deviation in the UCS skull from a normal control skull.

In this step of the workflow, there are two important constraints to consider when determining the margins of the segmented frontal bone. The superior, inferior, medial and lateral limits of the segment are a) areas that are restricted to the frontal bones, and/or b) areas with significant bony overlap between the two registered skulls. The degree of bony overlap is a visual, qualitative assessment by the user. Qualitative assessment of registration accuracy has been described to confirm registration accuracy (Dangi et al., 2017). It is possible, especially when defining the superior and inferior limits that the second constraint is not met. However, the size of the area that is segmented is only limited to portions of the skulls that are well aligned following the registration step. This is demonstrated in Figure 3 where the same index value is generated between two different sized segmentations (panels B and C). In panel C, the segmentation was expanded more laterally compared to the segmentation in panel A to highlight that if the skulls are a good size match and consequently well registered, the same deformity index will automatically be calculated despite the segment size. However, a downside of using age and sex-matched skulls is that it is challenging to align all areas of the two skulls, hence why the segmentations are limited to areas that are well registered. Potential areas that may not be well aligned when using age and sex-matched controls are commonly the orbits and the skull vertex. Therefore, these regions are consistently omitted in the segmentation. Including these components may result in calculating an index value away from the area of interest (frontal bones), as demonstrated in Figure 3 (panel E). The location where the index value is derived is confirmed in the last step.

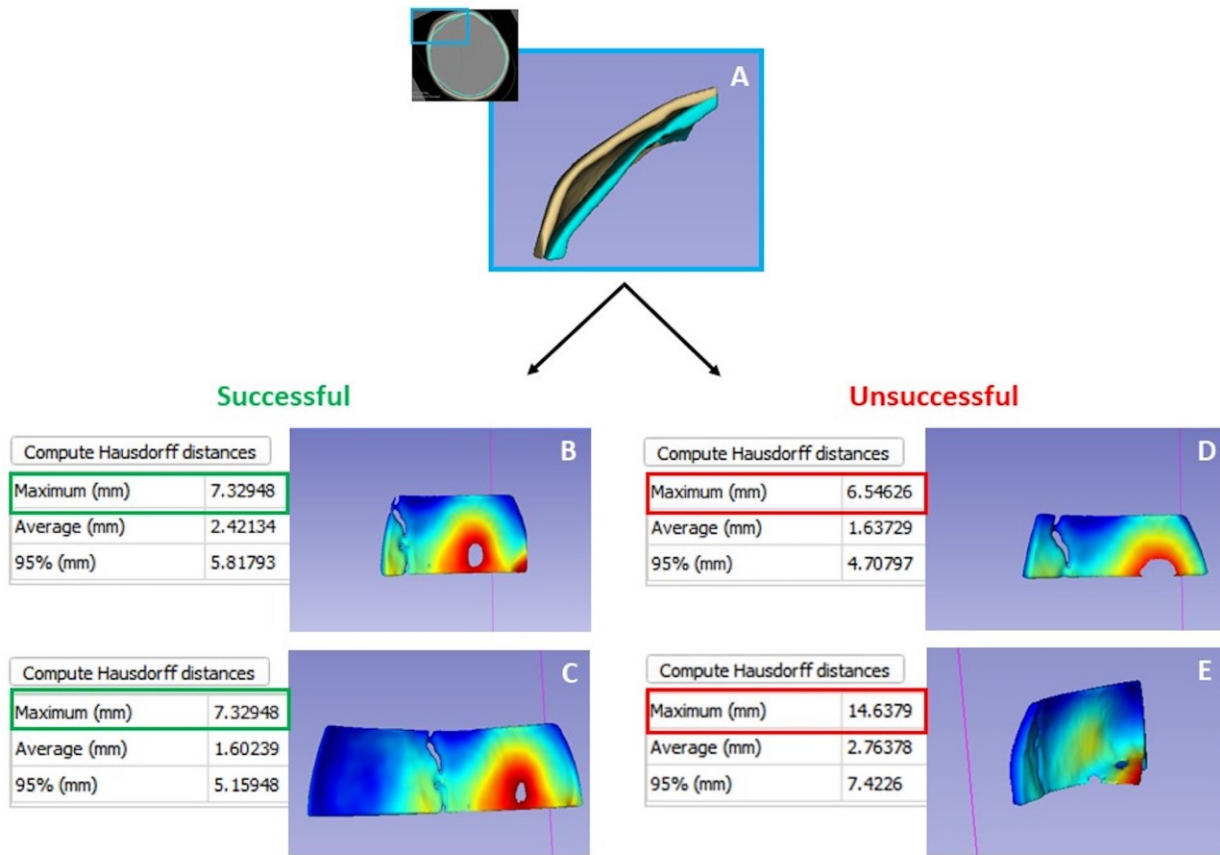


**Figure 2.3** The goals and potential pitfalls of the segmentation step are outlined in this figure, as well as the use of color maps to verify the location where the deformity index is calculated. Panel A shows the worm’s eye view of the segment of frontal bone isolated from the CT scan (top left). Panel B is a color map of the segment of frontal bone taken from the synostotic side in the UCS patient (blue skull), with information regarding the surface distances to the corresponding segment of the normal frontal bone (beige). Warm hues denote a distance further away from the UCS skull, which correspond to areas on the UCS frontal bone that are flattened when compared to the normal skull. Cool hues denote areas between the two skull segments that are close together, corresponding to areas of less deformity. In panel B, it is clear that the deformity index value of 7.329 mm is calculated from within the frontal bone segment, confirming that the value is calculated in the region of interest. In panel C, the same value is derived from a larger segment of the frontal bone. This emphasizes that the deformity index value will be identical between segments that are limited to the constraints outlined in the workflow. In panel D, the segmentation did not include sufficient frontal bone inferiorly, resulting in a smaller deformity index that is not representative of the true deformity. This is confirmed by the color map, which has warm hues at the inferior edge of the segmentation, and disappears from the same edge when the maximum threshold for the color map is reduced. This confirms that the deformity index was calculated from the edge of the segmentation, is not representative of the region of interest, and the segmentation step would require revision. Finally, panel E demonstrates what may happen if the first constraint is violated and the segment includes areas outside of the region of interest. In this case, the superior orbit of the UCS skull was included in the segmentation, again resulting in an erroneous deformity index that is not representative of the deformity at the frontal bones. In the confirmation step, it is clear that the maximum surface distance of 14.638 mm is derived from the region of the orbit as the warm hues are restricted to the portion of the superior orbit.

#### 2.4.3.4 Surface Distance Calculation

In the SlicerRT Extension, the Segment Comparison module is used to automatically calculate the maximum Hausdorff surface distances between the two frontal bone segments (Pinter et al., 2012) (Figure 3). This automatically calculated distance represents the largest deviation on the UCS skull from a normal reference skull. A larger distance corresponds to more frontal bone flattening on the synostotic side of the UCS skull, and can be used to represent a more severe deformity. The deformity index is the maximum Hausdorff distance value calculated in this step between the segmentations created in the previous step.

Maximum Hausdorff surface distances were used to calculate the deformity index. This technique is commonly used when comparing one shape to another and determining how much they differ from each other (Huttenlocher et al., 1993). When comparing the forehead region of two different skulls, this distance represents a linear measurement from a distinct point measured on the UCS skull to a corresponding point on the normal skull. A linear distance is calculated along every point along the UCS forehead to a corresponding point on the normal forehead. For example, for each set of linear distances calculated from point A, on the UCS skull, to point B on the normal skull, the shortest distance from the UCS to the normal skull is determined. These calculations are made for every point on the UCS skull, and the maximum Hausdorff distance is the largest of these minimum values. Therefore, the deformity index value is the longest possible distance travelled from a point on the UCS skull to closest point on the normal skull. This distinction is important when using the Hausdorff distance to quantify deformity as it avoids calculating an erroneously large number, which would represent a large degree of deformity, from a linear distance calculated at an oblique angle from one point on the UCS skull to a point on the normal skull, for example. While a single value is generated using this method, it is a representation of a global shape since it is calculated after an analysis of every point along the entire surface of the model in question, which is the UCS skull in this application. Therefore, it overcomes the pitfall of measurement techniques such as the AUC of being reliant on the accurate alignment of anatomic landmarks. The AUC is measured from a single axial CT scan slice (Khechoyan et al., 2014). Therefore, in order to make meaningful comparisons to other skulls, the landmarks that dictate where the slice is chosen have to be clearly identified and consistently used. A drawback of reporting a maximum Hausdorff distance is that it does not give information regarding the area of the abnormal skull that is involved. For example, a skull

that has a forehead that is not positioned significantly posterior when compared to a normal skull but where the deformity occurs over a large area would still be assigned a small deformity index value. This has the potential to erroneously categorize a UCS skull with significant deformity as having a mild deformity.

#### **2.4.3.5 Confirmation**

Finally, a color map model is generated using the Model-to-Model Distance module (Figure 3). On the ‘Models’ screen, the maximum surface distance threshold on the color map is decreased to confirm that the measurements are taken from within the segmentation, and not from a margin of the segment. If decreasing the upper limit of the threshold makes the model disappear from a margin, the previous steps are repeated. Disappearance from the center of the segmentation confirms that the measurement is taken from within the segment, and the point of maximum surface distance between the two skulls is captured. If, in the confirmation step, it appears that the maximum distance was calculated from a margin of the segmentation, it cannot be confirmed that the deformity index calculated is from the maximum point of deviation at the frontal bones.

#### **2.4.4 Reliability**

The reliability of the index was assessed using test-retest reliability. Fifteen pairs of UCS and age/sex-matched control CT scans were collected (Table 1). One study pair (#11) was not sex-matched due to unavailability of a suitable control. However, the size difference between the skulls was minimal, and registration was still possible. The sample size was chosen based on the predicted availability of UCS CT scans based on incidence values and recent birth rate data in Alberta (*Alberta Health, Analytics and Performance Reporting Branch*, 2018), as well as to sufficiently power a correlation analysis. Each skull pair was input into the workflow developed in part one and assigned an index value of deformity. Maximum Hausdorff surface distances were collected for each UCS skull. The reliability of the measurement index was assessed using an intra-class coefficient. The same assessor ran each skull pair through the workflow twice, with each trial separated by at least four weeks to minimize observer bias (Delgado-Rodriguez, 2004). The intra-class correlation was calculated in R Studio (Version 3.6.1) as the test-retest coefficient between the two data sets. A p-value of less than 0.05 and a correlation coefficient of  $\geq 0.7$  was considered evidence of high test-retest reliability (Hinkle et al., 2003). Lastly, a single

case of UCS was used as an illustrative example to demonstrate a potential application of the measurement index workflow. The workflow was used to quantify deformity for one UCS patient's pre and postoperative skull after a CVR procedure. The two values were compared to quantify the degree of advancement achieved and to determine if the measurement index can be used as an indication of reconstruction success. As it is not standard practice at the study institution to image patients postoperatively, a single case design was chosen due to the paucity of postoperative CT scan data.

**Table 2.1** Age and sex matched participants for the study pairs

Pair #	Experimental Skull		Control Skull	
	Age (mos)	Sex	Age (mos)	Sex
1	7	F	7	F
2	3	M	3	M
3	4	F	4	F
4	5	F	5	F
5	3	M	3	M
6	4	F	4	F
7	5	F	5	F
8	3	F	3	F
9	5	F	5	F
10	15	F	14	F
11	6	M	7	F
12	5	F	5	F
13	3	F	3	F
14	5	F	5	F
15	9	F	8	F

## 2.5 Results

The workflow met the outlined design criteria. Also, there is a conceptual alignment between the generated values and the visual salience of the targeted UCS feature (frontal bone asymmetry). The index value is generated from the frontal bone on the fused side of a UCS skull, which is flattened and retruded when compared to a normal skull. Figure 4 depicts two different UCS skulls that demonstrate varying degrees of forehead asymmetry. The top picture shows the forehead region of a UCS skull with a subtle deformity, whereas the bottom picture highlights

the same area of interest but from a UCS skull that has apparent asymmetry. The values generated for these skulls (A = 1.99 mm, B = 10.36 mm) seem to reflect the varying degree of deformity. This suggests that there is congruence with the amount of frontal bone flattening and the index value.

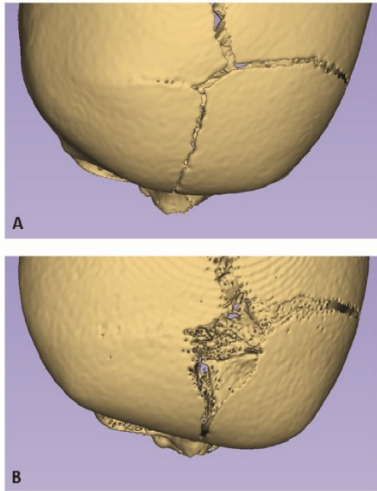


**Figure 2.4** Panel A) depicts the bird's eye view of the skull assigned the smallest surface distance value (1.99 mm), and panel B) depicts the same view of the skull assigned the largest surface distance value (10.36 mm). Skull A has a more symmetrical appearing forehead than skull B, and therefore the assigned index value corresponds with a subjective assessment of frontal bone deformity, at least at the extremes of surface distances.

The deformity index values for the 15 UCS cases ranged from 1.99 – 10.36 mm (Table 2). The intra-class coefficient for the test-retest reliability analysis was high (ICC = 0.93,  $p = <0.001$ , CI: 0.82, 0.98) for the maximum Hausdorff surface distance (Figure 5).

**Table 2.2** Results for test-retest reliability assessment.

Pair #	Maximum Hausdorff Surface Distance (mm)	
	Trial #1	Trial #2
1	5.95	5.95
2	6.92	7.26
3	6.62	4.61
4	4.97	3.82
5	7.80	7.81
6	5.85	6.11
7	8.53	8.73

8	5.28	4.85
9	1.99	2.43
10	4.60	4.42
11	4.28	4.75
12	5.34	4.73
13	10.36	10.22
14	2.81	4.12
15	5.32	5.83

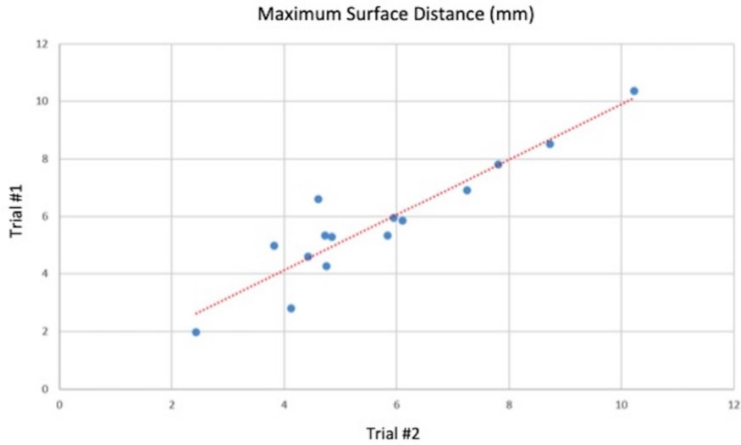


**Figure 2.5** Correlation between the maximum surface distances between the workflow trial one and trial two was 0.93 demonstrating high reliability and a measure that is reproducible.

This indicates that this measure is highly reproducible. For the illustrative example, a deformity index of 7.43 mm was calculated between the preoperative and the postoperative reference skull. This value represents the maximum frontal bone advancement achieved with the operation. This degree of advancement of the affected frontal bone is apparent on an axial view of both CT scans post-registration and segmentation (Figure 6).

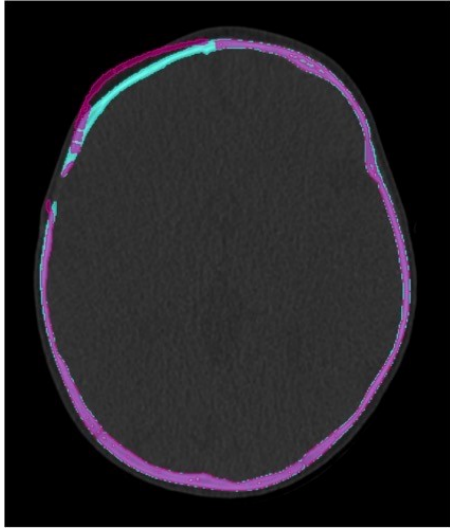


**Figure 2.6** An axial slice of the preoperative (blue) and postoperative (purple) CT scan of the same patient in figure 7 are registered. Areas where the preoperative and postoperative skull register and align well are displayed in a purple-blue color. The discrepancy between the frontal bones on the synostotic side (patient's right side, top left in the figure) is apparent. In this application, the measurement index corresponds to the largest distance between the blue and purple skulls on the synostotic side.

## 2.6 Discussion

A single, open-source software program was used to develop an objective deformity index workflow for the UCS population that was used for two purposes: 1) to quantify the degree of deformity at the frontal bones, and 2) to quantify the impact of surgical intervention. The workflow's combination of manual and automated components, as well as qualitative and quantitative assessment, allow for a clinician-friendly workflow that does not sacrifice reliability. The high intra-class coefficient demonstrates that the workflow is highly reproducible, despite having manual and qualitative components. Automation allows for a time-efficient process, a feature that may be attractive to busy surgical teams. 3D Slicer is a valuable and widely accessible tool for craniomaxillofacial surgical teams.

The use of age and sex-matched CT scans as the control group also adheres to the user-friendliness and accessibility criteria outlined for the proposed workflow. More surgeons are likely to have access to a database containing normative skulls as opposed to more sophisticated tools like statistical shape models, for example. The reliance on specific multi-atlas' is a recognized limitation of advanced quantification methods (Mendoza et al., 2014). Processes that can be carried out without the need for outsourcing or consultation are advantageous from a time and cost perspective. In addition, a user-friendly and inexpensive method to assess reconstruction

outcomes may increase clinician productivity in this field. Methods of morphometric quantification that require expert consultation or proprietary software may be a barrier to their regular use. In addition, the cost of using advanced technology is a recognized deterrent (Barbero-García et al., 2017; Fisher et al., 2016; LoPresti et al., 2017; Martelli et al., 2016; Seruya et al., 2013). As methods like statistical shape modeling become more commonplace in the clinical environment, this could replace the use of age and sex-matched CT scans for a more precise workflow.

The deformity index can be used to compare surgical outcomes in UCS correction surgery. The benefit of this application is that registering a patient's preoperative CT scan to his or her own postoperative scan does not require the use of a matched normal comparison. As a result, the values that are generated are more likely to be a very accurate representation of the surgical changes in skull morphology. When postoperative CT scans are available, this method could be used to help surgical teams assess the effectiveness of different surgical techniques available for craniosynostosis corrective surgery.

Having a method to quantify morphology in craniosynostosis is important not only to compare different surgical procedures but also to assess the benefits of using advanced technology in the peri-operative environment. This is relevant as virtual surgical planning (VSP) is being increasingly utilized for CVR (Fisher et al., 2016; Khechoyan et al., 2014; Mazzaferro et al., 2017; Queiros et al., 2017; Soleman et al., 2015; Xu et al., 2017). Advanced surgical planning technologies are especially useful when treating unilateral deformities, such as UCS that are asymmetric and additionally complex (Alford et al., 2018). A reliable and user-friendly method to describe deformity in UCS is required to assess the potential advantages of using advanced technology for VSP, as well as evaluating different surgical techniques. In addition, the deformity index could be used in the preoperative planning environment as a method to compare preoperative imaging to virtual reconstructions. The MeshStats module in 3D Slicer can be used to calculate maximum surface distances between models derived from CT scans and virtually reconstructed models.

The proposed workflow derives an objective value of deformity at the affected frontal bone in UCS skulls. UCS was chosen as the target population due to available data and the added treatment complexity for this craniosynostosis subtype. However, the workflow does not require

the delineation of specific bony or soft tissue landmarks and is therefore flexible enough that it could be applied to different types of craniosynostosis. Changing the region of interest by segmenting and isolating different areas of the skull could make the workflow suitable to other subtypes. For example, a deformity index could be calculated bilaterally in metopic synostosis by segmenting out right and left frontal bones individually. In lambdoid synostosis, the workflow could be modified to segment out the posterior vault as opposed to the frontal bones to derive a deformity index.

Lastly, visual aids, such as three-dimensional (3D) printed skull models, have demonstrated a benefit for parents of patients undergoing CVR (van Nunen et al., 2014). Displaying images depicting the change in skull shape (Figure 7) with corresponding numerical values for the amount of operative advancement may be a cost-effective and valuable tool in consultation and follow-up evaluations with patients and their families.

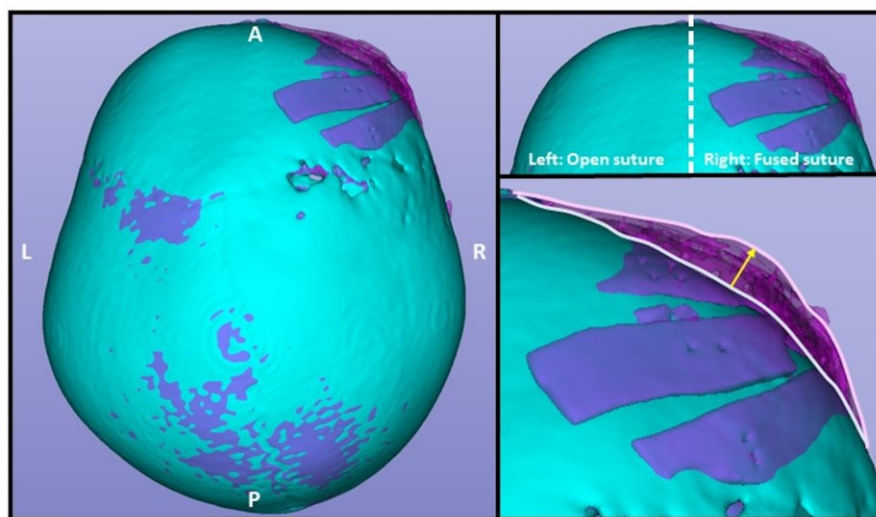


**Figure 2.7** The preoperative (blue) and postoperative (transparent purple) CT scans in a patient with UCS treated with a unilateral FOA are registered in order to appreciate the degree of frontal bone advancement. The postoperative skull is transparent in order to visualize the forehead contour of the preoperative skull. In the left panel, the improved forehead symmetry of the postoperative skull is noticeable on the bird's eye view. In the top right panel, the non-synostotic (left) and synostotic (right) sides of the forehead are outlined. This patient was treated with a unilateral advancement, meaning only the right-sided frontal bones were advanced. In the bottom right panel, the light purple curve outlines the new contour of the forehead in the postoperative skull, compared to the light blue curve, which outlines the preoperative contour. The yellow arrow highlights the degree of advancement visible from this view.

### **2.6.1 Limitations**

One of the limitations of this study is the use of age and sex-matched skulls. This method has been used previously to describe and measure deformity in a craniosynostosis skull (Chim et al., 2014; Dangi et al., 2017; Soleman et al., 2015). However, using a composite skull or a statistical shape model would increase the skull registration accuracy (Mendoza et al., 2014; Saber et al., 2012). Downsides of the latter techniques are that they require large volumes of CT scan data, which were unavailable at the study institution. In addition, age and sex-matched skull data is readily available to most clinicians. In contrast, more precise tools such as statistical shape models are more likely to require expert consultation and the presence of a large database of images in order to create a suitable tool. Although less precise, the use of age and sex-matched skulls as control data supports the workflow criteria of usability and accessibility and allowed for a highly reproducible index.

Another limitation of the presented workflow is the use of CT scan data. While using CT scans allows for the accurate registration of high-resolution images, subjecting infants to ionizing radiation is a concern. This has prompted the creation of head shape and volume quantification workflows based on 3D photogrammetry (Barbero-García et al., 2017; de Jong et al., 2017; McKay et al., 2010; Porrás et al., 2019; Tu et al., 2019; Wilbrand et al., 2012). These are excellent tools to quantify cranial vault morphology, especially for long-term follow-up in order to obviate the need for repeated exposure to radiation. However, virtual surgical planning for CVR is increasingly popular and is currently reliant on CT scan data. In addition, as Wood et al. (2016) highlight that there are pitfalls with relying on clinical exams to diagnose craniosynostosis. As a result, some surgeons may find that the benefit of a precisely planned operation on an accurate CT scan diagnosis outweighs the risk of radiation exposure. Therefore, the potential applications of the deformity index in the surgical planning and consultation environments would be feasible with one preoperative CT scan. Additionally, the described index does not rely on specific bony or soft tissue landmarks. Therefore, it is plausible that a similar stepwise approach could be applied to radiation-free imaging modalities such as 3D photogrammetry. In this study, the CT scans used to calculate measurements had been previously obtained for clinical indications, and no infants were prospectively scanned for data collection.

### **2.6.2 Future Direction**

Future work in this area would focus on implementing a similar stepwise approach using open-source software with 3D photogrammetry images.

### **2.7 Conclusion**

Quantifying cranial vault morphology in craniosynostosis is challenging, and outcome measures are inconsistently reported in the literature. A highly reproducible deformity index workflow for UCS that is user-friendly, objective, and accessible was developed. A stepwise process that allows clinicians to assess gross morphological differences or postoperative changes at the frontal bones in UCS may be beneficial in surgical planning and consultation.

## Chapter 3: Perception Study

### 3.1 Abstract

#### Background

Cranial vault remodeling aims at improving the aesthetic appearance of infants with unicoronal synostosis (UCS) by reshaping the forehead and reducing the potential for psychosocial discrimination. Peoples' perception of craniofacial deformity plays a role in the stigma of deformity. The purpose of this study is to examine the relationship between objective skull deformity in UCS patients and laypersons' perception of skull normality.

#### Methods

Forty layperson skull raters were recruited from the general public. Skull raters were asked to categorize 45 infant skull images as normal or abnormal. Twenty-one of the images were UCS skulls, and 24 were normal skulls. Skulls were displayed briefly on a computer to simulate a first impression scenario and generate a perceptual response. Chi-squared analysis and mixed-effects regression model were used to analyze the response data.

#### Results

Members of the general public were good at distinguishing between skull groups ( $\chi^2(1) = 281.97, p < 0.001$ ). In addition, skull raters' responses were predicted by the severity of deformity in the UCS skulls ( $b = -0.10, z = -2.6, p = 0.010, CI: -0.18, -0.02$ ). A skull with a deformity value of 2.8 mm ( $CI: 1.8, 4.1$ ) was equally likely to be rated normal or abnormal.

#### Conclusions

This is the first study investigating the relationship between objective skull deformity in UCS and public perception. Laypersons were good at distinguishing between normal and UCS skulls, and their perceptions of normality were predicted by the amount of skull deformity.

### **3.2 Background**

Unilateral coronal craniosynostosis (UCS) is a common subtype of craniosynostosis that affects the shape of an infant's skull resulting in anterior plagiocephaly, a phenotype characterized by an asymmetric forehead appearance (Campbell & Derderian, 2014). Facial attractiveness ratings of children with craniosynostosis by laypersons are lower than their age and sex-matched peers (Collett et al., 2013). As a result, children with untreated craniosynostosis may face psychosocial adjustment challenges (Snyder & Pope, 2010). Cranial vault remodeling (CVR) surgery aims at improving the aesthetic appearance of children with UCS by reshaping the bones that form the contour of the forehead (Alford et al., 2018). Specifically, fronto-orbital advancement (FOA) consists of reshaping the frontal bones and the superior orbital region and remains a first-line treatment for UCS (Tahiri et al., 2017).

Reported outcomes in the literature regarding surgical treatment for UCS focus attention on the restoration of a normal head shape and an improved aesthetic appearance. Photographic assessment is frequently used to demonstrate an aesthetic improvement, as well as reports on the presence of common morphologic features associated with UCS (Chim et al., 2014; Fisher et al., 2016; Hilling & Vaandrager, 2006; Mardini et al., 2014; Soleman et al., 2015; Taylor et al., 2015). Similarly, the popular Whitaker scale, a tool used to assess the severity of deformity in patients with craniosynostosis, is based on surgeons' subjective assessment of a patient's appearance (Whitaker et al., 1981). All of these methods rely on perceptions of experts in craniofacial reconstruction. However, previous studies on facial attractiveness have shown that patients' perceptions may not always correlate with experts' perceptions (Cochrane, 1999; Vargo et al., 2003).

A primary goal of CVR is to improve the appearance of an infant's head to prevent psychosocial discrimination later in life. In general, psychosocial discrimination is a consequence of perceptions of the general public as opposed to assessments of craniofacial experts. However, there are no outcome measurements that correlate surgical outcomes with laypersons' perception of skull normality.

### **3.3 Objectives**

The goal of this study was to determine if there is a relationship between an objective value of skull deformity and laypersons' perceptions of skull appearances. Additional objectives

were to determine if there were other factors influencing peoples' ratings of skull appearance, as well as to determine if there is a threshold value whereby members of the general public are unable to decipher the difference between a normal and a UCS skull. The primary interest in this study was to simulate and investigate a first impression scenario, thus mimicking a common situation where rapid judgments are made regarding peoples' appearances.

### **3.4 Materials and Methods**

#### **3.4.1 Participants**

After institutional ethics review board approval (Pro85714), layperson skull raters from the general public were recruited for this study. All raters were adults living in Edmonton with non-surgical backgrounds. After obtaining informed consent, 40 layperson skull raters were recruited. The average age of the raters was 33.6 years ( $SD = 12.4$ ), consisting of 21 females and 19 males. Most of the raters had a post-secondary level of education (92.5%).

CT scans from infants whose skull images were rated by the first group were also obtained. A waiver of consent was granted to access the infant skull data. The second group was subdivided into two cohorts; the control cohort consisted of skull images from infants with normal skull morphology, and the other cohort consisted of skull images from infants diagnosed radiographically with UCS. The control cohort consisted of computed tomography (CT) scan data retrospectively collected from infants less than two years of age, had CT head scans with  $\leq 1$  mm slices in coronal, axial, and sagittal planes, and had no skeletal craniofacial abnormalities, including skull bone fractures and congenital deformities (i.e., craniosynostosis). Two years was selected as the maximum age cut-off for the skull groups, as this corresponds with when most children with craniosynostosis would be diagnosed by in order to take advantage of optimum surgical timing (Tahiri et al., 2017). The UCS cohort consisted of infants with similar age and sex demographics to the control group, but who had single suture coronal synostosis in the absence of any additional skeletal abnormalities. Skull data were collected from 45 infants. There were 21 participants in the UCS cohort and 24 participants in the normal skull cohort. The majority of the skull participants were female with right-sided UCS. The two cohorts did not significantly differ statistically regarding age (Mann-Whitney  $U = 184$ ,  $p = 0.12$ ) and sex ( $\chi^2 = 0.164$ ,  $p = 0.69$ ) variables. Demographic data for the skull raters and the skull groups are summarized in Table 1 and Table 2.

**Table 3.1** Summary of demographic data for the layperson skull raters.

<b>Demographic Characteristic</b>	<b>Layperson Skull Raters</b>	
	<i>Number</i>	<i>Percent</i>
<b>Total</b>	40	100.0
<b>Sex</b>		
<i>Female</i>	21	52.5
<i>Male</i>	19	47.5
<b>Level of Education</b>		
<i>High school</i>	3	7.5
<i>Post Secondary</i>	37	92.5
	<b><i>Mean ± STD</i></b>	<b><i>Range</i></b>
<b>Age</b>	33.6 ± 12.4	22 - 73

**Table 3.2** Summary of demographic data for the skull cohorts.

<b>Demographic Characteristic</b>	<b>Normal Skulls</b>		<b>UCS Skulls</b>	
	<i>Number</i>	<i>Percent</i>	<i>Number</i>	<i>Percent</i>
<b>Total (/45 skulls)</b>	24	53.3	21	46.7
<b>Sex</b>				
<i>Female</i>	17	70.8	16	76.2
<i>Male</i>	7	29.2	5	23.8
<b>Affected suture</b>				

<i>Right</i>	--	--	17	81.0
<i>Left</i>	--	--	4	19.0
	<i>Mean ± STD</i>	<i>Range</i>	<i>Mean ± STD</i>	<i>Range</i>
<b>Age (months)</b>	7.0 ± 4.3	2 - 16	4.9 ± 3.0	1 - 15

Surface distance values were used to quantify deformity in the UCS cohort and ranged from 1.97 mm to 10.36 mm, with an average value of 6.06 mm and a standard deviation of 2.06 mm. Figure 1 displays the distribution of surface distance values.

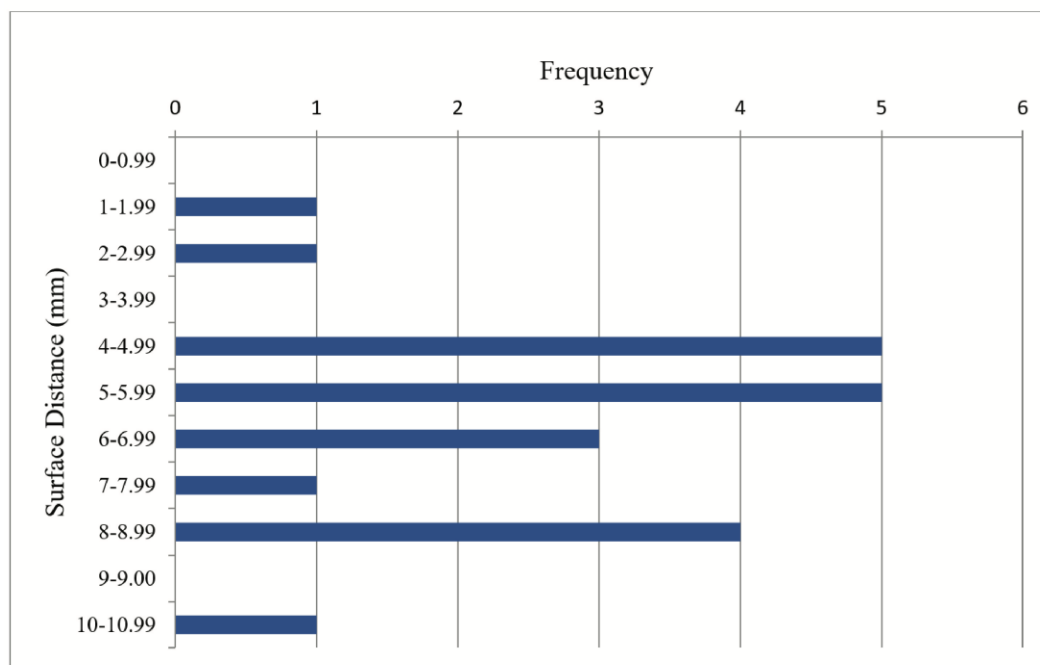


**Figure 3.1** Distribution of surface distance values among the UCS skull cohort.

### 3.4.2 Experimental Design

Three-dimensional (3D) skull models were generated for all 45 infant participants using an identical protocol. The digital imaging and communications in medicine (DICOM) data from CT head and/or CT facial bone scans were imported into the open-access software 3D Slicer (Version 11.0) (Fedorov et al., 2012). In 3D Slicer, the facial skeleton was segmented and

a stereolithography (STL) file was generated. Mandibles were removed from the image files to isolate the cranial vault as the region of interest. STL files were imported into KeyShot (Version 8.2.80), rendering software to standardize the display environment for all skull models, as demonstrated in Figure 2 (i.e., lighting, color, skull orientation, etc.).



**Figure 3.2** Examples of skull models as they appeared on the computer screen. The skull on the left is an example of a normal 3D skull model generated for this study. The skull on the right is an example of a UCS 3D skull model generated for this study.

A two-alternative forced-choice design was used for this study. Images were displayed to each skull rater on a Microsoft PowerPoint (Microsoft PowerPoint for Mac 2011, version 14.7.7) presentation on the same laptop computer (Figure 3). Each skull model was displayed on the screen for 300 milliseconds in randomized order, followed by five seconds to record a response. Raters were given a recording sheet with the skull number and the letter “N” or “A” to circle, corresponding to “Normal” and “Abnormal.” Following a brief training session on the features of normal infant skulls, participants began the study and were asked to record whether they thought each displayed skull was normal or abnormal. The experimental design was piloted five times to optimize the simulation of a first impression scenario and ensure a smooth flow of events. For the pilot sessions, stimulus duration and inter-stimulus duration was varied from 0.1 – 3 seconds and 3 – 5.3 seconds, respectively. Based on participant feedback regarding task difficulty, stimulus, and inter-stimulus duration were adjusted.

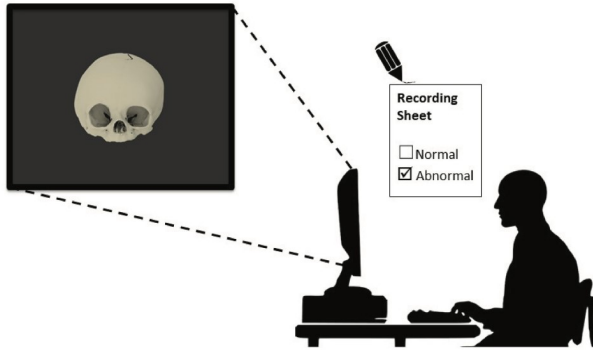


**Figure 3.3** Experimental setup. Skull raters viewed the skull images on a laptop computer screen and were asked to categorize each skull as ‘normal’ or ‘abnormal’. Responses were recorded on an answer sheet. Each skull was displayed for 0.3 seconds, and raters had 5 seconds to record a response.

### ***3.4.3 Surface Distance Measurement***

Frontal bone surface distances were calculated for the UCS cohort in order to assign a quantitative value for cranial vault deformity in each skull. The degree of the deformity was determined using the workflow outlined in Figure 4. In 3D Slicer, a CT scan from the UCS cohort was imported, along with an age and sex-matched normal CT scan (control skull). The control skull was the only manipulated image in the workflow in order to reduce the possibility of artificially exaggerating or muting the deformity in the UCS skull. The skulls were then manually aligned, followed by an automatic geometry-based rigid registration to obtain the best inter-skull comparison possible. Once registered, the skull bones were segmented from the CT scans, and then further segmented to isolate the frontal bones for each skull. Hausdorff surface distances are standard units in medical image software analysis and were used to quantify UCS deformity at the frontal bone region in this study. In 3D Slicer, distances were automatically calculated in millimeters between the UCS and normal CT frontal bones using the Segment Comparison module. Using this method, a larger surface distance corresponds to a forehead that is positioned more posteriorly on the synostotic side when compared to an age and sex-matched normal skull. Normal skulls are used as the control skulls, and are therefore assumed to have a deformity value of zero millimeters. The value generated using this method served as a surrogate marker for the severity of anterior plagiocephaly in a UCS skull. Frontal bones were selected as the target area to measure deformity since they constitute the forehead, and therefore represent an area of the facial skeleton that is noticeable to onlookers. In addition, the frontal bones are

manipulated in FOA procedures to correct anterior plagiocephaly and are therefore of particular interest.

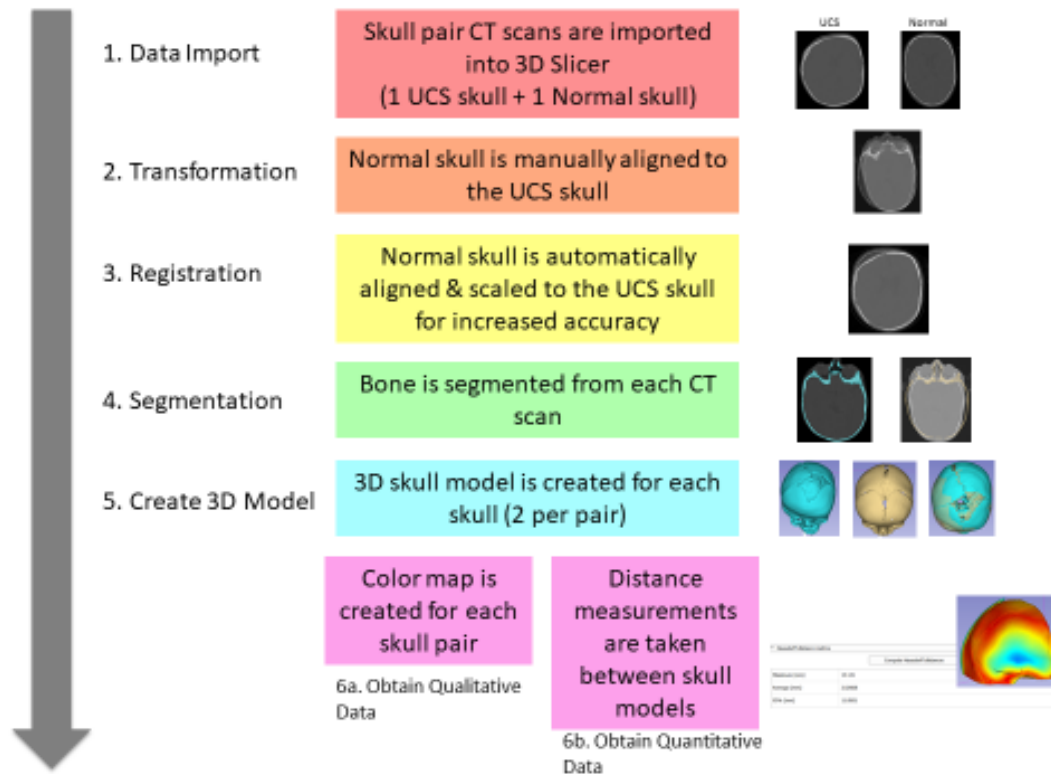


**Figure 3.4** Overview of the workflow used to determine surface distance values. This workflow is outlined in detail in Chapter 2.

### 3.4.4 Analysis

A chi-square analysis was used to determine if skull raters were able to distinguish between abnormal (UCS) and normal skulls. A mixed-effects logistic regression model was fitted to the response data for the UCS skulls to determine if the objective values of skull deformity impacted raters' responses. A similar model was used to solve for a threshold value of deformity and was fitted to all available data, including the normal skulls. The threshold value was defined as the point along the surface distance scale, where the statistically estimated psychometric response curve assumed a value of 50%. This number represents the objective value of deformity, whereby the responses from the skull raters were equally divided between normal and abnormal. Skull presentation order was analyzed to determine if this factor influenced rater responses.

### 3.5 Results

The skull raters were able to accurately distinguish between normal skulls and UCS skulls the majority of the time ( $\chi^2 [1, N=40] = 281.97, p < 0.001$ ). When shown a UCS skull, layperson raters correctly categorized the skull as ‘abnormal’ 71% of the time. Similarly, when shown a normal skull, the raters categorized the skull as ‘normal’ 69% of the time (Figure 5).

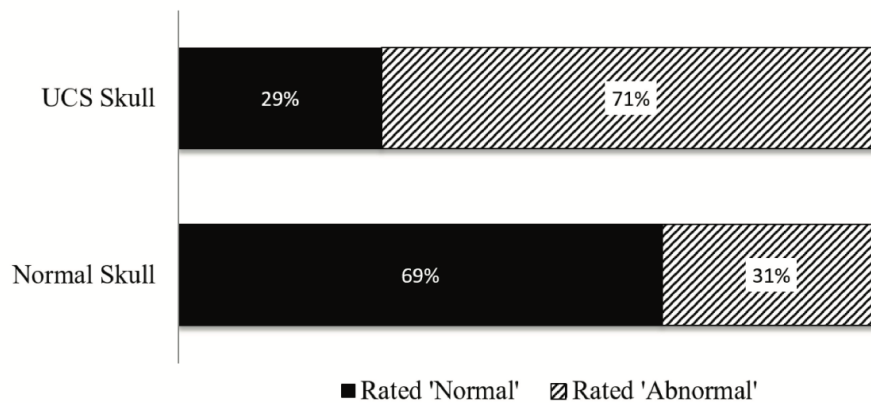


Figure 3.5 Results of the chi-squared analysis of skull rater responses.

A mixed-effects logistic regression model fitted to the response data for the UCS skulls revealed that objective values of skull deformity predicted raters’ categorization of the skulls. Larger surface distance values for the UCS skulls, corresponding to more a significant forehead deformity, resulted in layperson raters being more likely to rank a skull as abnormal versus normal ( $b = -0.10, z = -2.6, p = 0.010$  [CI: -0.18, -0.02]).

Based on a mixed-effects regression model that was fitted to all the available data including normal skulls, a threshold value of deformity of 2.8 mm [CI: 1.8, 4.1] was determined based on the degree to which the objective value of deformity impacted responses ( $b = -0.27, z = -15.6, p < 0.0001$  [CI: -0.30, -0.23]). The steeper slope in this model, compared to the model containing only UCS skulls, reflects the homogeneity of the values assigned to the normal skulls (i.e., all zeroes). The skull presentation influenced the rater responses, so that skull raters were 1.4% more likely to rank each subsequent skull as normal as they progressed, resulting in a relative increase of ‘normal’ responses towards the end of the experiment.

### 3.6 Discussion

In a simulated first impression scenario, members of the general public were able to differentiate between normal and abnormal skulls. This performance is impressive given the complex geometry of an infant craniofacial skeleton and the very rapid exposure time in this study. This highlights the sensitivity of human visual perception to changes in facial symmetry, particularly in the upper third of the face, which has been demonstrated previously (Hohman et al., 2014).

In addition, UCS skulls with more severe anterior plagiocephaly were visually more salient than the skulls with a more subtle deformity. The methods of quantifying deformity in this study strictly isolated the asymmetry in the frontal bones of the UCS skulls. These findings suggest that while there are a number of skeletal differences between normal infant and UCS skulls, the characteristic features of contralateral forehead bossing and ipsilateral flattening is a feature driving peoples' responses. This is in keeping with findings by Hohman et al. (2014) and Kim et al. (2013) that report humans are more perceptive to changes in upper versus lower facial symmetry.

Another factor that influenced raters' responses was the order of skull exposure. People were more likely to categorize a skull as normal if it appeared later in the presentation. Response fatigue in two-alternative forced-choice tasks may have contributed to the response pattern in this study.

The threshold value of 2.8 mm determined in this study suggests a degree of UCS deformity that would be difficult to detect by laypersons. This value is consistent with findings in the perception literature and is close to the range determined by previous studies (3-4 mm) looking at perceptions of facial asymmetry and detectable differences (Choi, 2015; Chu et al., 2011). Therefore, a 2.8 mm frontal bone discrepancy may serve as a reasonable goal to aim for when planning FOA procedures. Virtual surgical planning (VSP) for CVR is becoming more popular among craniofacial surgeons (Burge et al., 2011; Chim et al., 2014; Fisher et al., 2016; Jans et al., 1999; Khechoyan et al., 2014; LoPresti et al., 2017; Mardini et al., 2014; Mommaerts et al., 2001; Queiros et al., 2017; Safran et al., 2018; Seruya et al., 2013; Soleman et al., 2015; Zhao et al., 2012). VSP has been shown to reduce the subjectivity of surgical decision making, reduce operating time, and yield aesthetic reconstruction results (Chim et al., 2014; Khechoyan

et al., 2014; Seruya et al., 2013). With the development and implementation of cost-effective ways to consistently utilize VSP, it is likely to become an increasingly ubiquitous tool in the surgical planning environment. With that said, a quantitative endpoint that is easily measured using cost-free software may be a valuable component in the planning armamentarium for FOA procedures.

CVR procedures are lengthy and associated with several risks, such as significant bleeding (Lee et al., 2012). The threshold value in this study may be useful information for consultation appointments between surgeons and parents of infants with UCS when considering treatment options. While the mortality and morbidity of these surgeries have improved over the years, the process of considering one's infant for an invasive procedure involving removal and reshaping of the skull can be considered daunting.

### ***3.6.1 Limitations***

One of the limitations of this study is the lack of small surface distance values for the UCS skull cohort (Figure 1), preventing the ability to determine a threshold value based on UCS data alone. However, a craniosynostosis diagnosis requires clinical suspicion based on noticeable deformity, therefore making it unlikely to detect UCS in infants who may have very minimal frontal bone asymmetry. Therefore, UCS data may not, by definition, be available for small deformities.

Additional limitations of this study are the lack of naturalness in the stimuli and the use of CT scans as the imaging modality. Regarding the stimuli, layperson raters were shown 3D skull models as opposed to pictures of infants' faces. The absence of soft tissue in the study stimuli takes away from the applicability of the findings to everyday life. However, the amount of soft tissue present in infants less than two years of age is minimal, and the deformity present in the facial skeleton is likely to be well reflected in the soft tissue. In addition, while the data for this study were collected retrospectively, it is important to note that there are concerns with exposing infants to the degree of ionizing radiation associated with CT scans. Researchers conducting future perception studies should consider the use of 3D photogrammetry. Of note, CT imaging allows for precise mapping of the craniofacial skeleton and accurate outcome measurements, making it a popular modality for virtual surgical planning. Therefore, the use of CT images in this study is consistent with commonly employed virtual planning practices,

allowing the threshold information gathered to be related directly to the current planning environment.

### ***3.6.2 Future Direction***

Future direction with this research includes conducting a similar experiment using clinical photographs or 3D scanning images of infants with uncorrected UCS to increase the transferability of the findings to a real-life scenario. In addition, while social discrimination is generally viewed as a construct of general public perception, it can be more accurately described as a result of one's peers' perceptions. Futures studies will involve recruiting child peers as skull raters to perform a similar task, and determining if there are differences between adult and child raters when it comes to craniofacial morphology.

### **3.7 Conclusions**

This study investigated the relationship between objective skull deformity in UCS and public perception. Layperson raters were effective at correctly categorizing normal and abnormal infant skulls when displayed very briefly, simulating a first impression scenario. Laypersons' perceptions of abnormality were predicted by an objective value of skull deformity, which was determined by surface distance values measured at the forehead region. The perceptual threshold value of deformity identified in this study is in keeping with values determined in other studies investigating perceptual visual thresholds in facial differences. This information may be helpful when counseling parents and patients, and for preoperative surgical planning of CVR surgeries.

## Chapter 4: Computer Automation in Surgical Planning

### 4.1 Abstract

#### Background

Craniosynostosis is a common condition affecting 1 in 1000 infants. Uniconal craniosynostosis (UCS) is a common subtype and results in a misshapen forehead. Cranial vault remodeling (CVR) is the primary method of treating UCS, and involves removing the abnormal bones, reshaping them, and securing them in place. CVR for UCS is especially challenging due to the asymmetric nature of the deformity. Computer automated surgical planning has recently been shown to be a feasible option to reduce the subjectivity of surgical decision making for CVR and reduce planning time by allowing a computer algorithm to determine the optimal surgical steps. Computer automation has not been used in the setting of UCS. The objectives of this study are to develop a virtual surgical workflow for CVR in UCS using the resources at the study institution, as well as to introduce automated steps into the workflow to build a conceptual framework for a fully automated surgical planning algorithm.

#### Methods

The virtual surgical workflows were developed using Geomagic FreeformPlus software. A CT scan from a three-month-old female with right-sided UCS was used as the index case. The reconstruction models built using the workflow steps were analyzed using Hausdorff surface distances, comparing them to preoperative skull models as well as normal control models. Boolean operations and model registration were two techniques used to introduce automation into the virtual workflow. Fifteen iterations of introducing automation into the workflow were carried out.

#### Results

The root mean square error of the maximum Hausdorff surface distances for the reconstruction model (0.69 mm) was smaller than for the preoperative model (1.64 mm) using the virtual surgical workflow, indicating it was closer in shape to a normal skull. Boolean operations and registration were introduced into the workflow and demonstrated success in outlining surgical regions of interest and repositioning these areas. The amount of frontal bone

advancement ranged from 3.089 mm to 10.478 mm. The amount of supra-orbital bar advancement ranged from -1.752 mm to 7.779 mm. Iterations #12 and #7 were the most successful at achieving a frontal bone and supra-orbital bar that were closest in shape to a normal reference skull, respectively. The degree of human involvement in the surgical planning process was decreased for the partially automated workflows.

## **Conclusion**

A virtual surgical workflow was developed using in-house software that allowed for a successful virtual reconstruction of a UCS case. Introducing automated steps into the workflow allowed for reconstructions that were closer in shape to a normal skull than the preoperative skull, as well as a reduction in subjectivity of surgical decision-making. The degree of surgeon involvement varied between the iterations. Boolean operations and image registration were automated techniques that successfully outlined key regions of interest and suggested surgical steps. The information gathered from the iterative process will serve as the conceptual framework from which to develop a fully automatic surgical planning algorithm.

## 4.2 Background

Craniosynostosis is a relatively common birth defect affecting up to 1 in 1000 live births. Left untreated, craniosynostosis can affect normal brain growth and development, can cause visual impairment, and can have a significant psychosocial impact on the child (Tahiri et al., 2017). Unicoronal synostosis (UCS) is a common subtype of craniosynostosis that is especially difficult to treat due to the asymmetrical nature of the deformity. Cranial vault reconstruction (CVR) is a primary method to surgically correct UCS, where the goals of surgery are to expand the intracranial volume, reduce the risk of abnormal brain growth, and to normalize head shape and appearance (Alford et al., 2018).

The use of virtual surgical planning (VSP) has been increasing for craniosynostosis reconstruction. VSP has been shown to reduce intra-operative procedure length (Khechoyan et al., 2014; Msallem et al., 2017; Xia et al., 2006). Virtual technologies have demonstrated particular utility for complex craniofacial cases (Fisher et al., 2016; LoPresti et al., 2017). Time spent by the craniofacial surgeon deciding where to make osteotomies (cuts in the bone) and in what configuration to plate bone segments, is shifted from the operating room to the pre-planning virtual environment. VSP also reduces the subjectivity of craniosynostosis reconstruction. Conventionally, surgeons perform osteotomies and plate bone fragments to transform a dysmorphic skull into a ‘normal’ appearing skull based on experience, guesswork, and trial and error. CVR surgeries are lengthy procedures, and the potential complications are severe, with significant blood loss remaining the most common cause of intra-operative morbidity and mortality (Lee et al., 2012). This further highlights the importance of using methods that reduce intra-operative time for these procedures.

Recent efforts using VSP in CVR are focused on using normal skulls as a template to guide surgical osteotomies and plating (Burge et al., 2011; Delye et al., 2015; Marcus et al., 2009). While studies have produced aesthetic results using this technique, time spent in meetings with the surgical team and the biomedical engineering team is significant, as are the costs involved, limiting the use of this technology to only a few tertiary centers (LoPresti et al., 2017). One center published their preliminary experience with VSP, quoting planning times of up to six days, and costs up to 6000 American dollars (Soleman et al., 2015). Therefore, there is a

potential role for computer automation in VSP for CVR, particularly in cost reduction and time efficiency. Efforts to decrease costs have included the use of open-source software and low fidelity 3D printers (Gerstle et al., 2014), however, planning time remains a barrier.

Preliminary attempts at automating this process have demonstrated success (Porras et al., 2016, 2017, 2018). Porras et al. (2016) introduced a transformation model to automatically generate a surgical plan for fronto-orbital advancement in metopic craniosynostosis. They improved their method by integrating bone bending in their updated procedure, involving a novel surface registration framework allowing transformations of individual bone components. In addition, they individually segment the typical components of an FOA procedure: the supra-orbital bar (SOB) and frontal bones (Porras et al., 2018). Their results were automated surgical plans for metopic craniosynostosis remodeling with varying numbers of bone segments, resulting in overall significant improvements in head shape. Expert surgeons agreed on the usefulness of the proposed automatic surgical plans. The computation time to generate the surgical plans in this model was an estimated four hours. However, this was unsupervised time and did not require any human involvement (Porras et al., 2018). In addition, automatic surgical planning could reduce costs in centers that currently outsource their surgical plan. Downsides of this method are the reliance on experts in medical image analysis and computer science, which may be a barrier for centers without this degree of collaboration. A more user-friendly method that provides automated surgical plans would be beneficial to surgical teams.

Using computer algorithms to generate surgical plans has the potential to reduce the subjectivity of surgical decision-making, planning duration, and resources. While VSP has demonstrated a benefit in CVR by reducing procedure duration, decreasing the subjectivity of surgeon decision making, and producing aesthetic reconstruction results, the cost and time investment of using advanced technology is prohibitive to its widespread use. In addition, surgical plans developed in a virtual environment are still reliant on subjective decisions made by the surgical team. The guesswork is reduced to an extent with the ability to use normal skull models as a reference. However, the decisions on where to cut and reposition the bone are still inherently subjective and based on surgeon experience. Corrective surgery for UCS is primarily a complex geometric problem. Introducing computer algorithms into the surgical planning process to solve a geometric problem may reduce the guesswork, cost, and time associated with VSP.

Recent data on automatic surgical plans for craniosynostosis in metopic craniosynostosis are promising. Published methods are mathematically advanced, and have not been applied to asymmetric craniosynostosis. Ultimately, computer automation in CVR planning may increase the availability of VSP, allowing more patients to benefit from precise preoperative planning.

Time and pressure constraints on surgeons, as well as costs involved with advanced technology, are important criteria to consider in the design process for virtual workflows (Burton et al., 2018). Objectivity and accessibility are key design criteria in the development of a CVR workflow. Minimizing surgeon involvement in the surgical decision making process was a design criteria for the workflow developed in this study in order to reduce the degree of guesswork. As the sophistication of automated surgical planning increases, the role of the surgeon in the design process could be directed towards ensuring the fidelity of the finished product as opposed to making multiple subjective decisions in a time-consuming and unpredictable process. The goal of this study was to achieve this by using in-house software to replace virtual planning steps that are currently dependent on surgeon involvement with automatic steps, thereby increasing the objectivity of the surgical planning process. A method for automatic CVR planning that meets these design elements may increase the availability of advanced technologies in the surgical planning environment, and decrease the guesswork associated with CVR.

### **4.3 Objectives**

The objective of this study was to develop a virtual surgical workflow for CVR in UCS at the study institution. Secondary objectives were to automate certain components of the workflow to reduce surgeon involvement in the planning process. The goal of this component was to create a workflow that had a combination of surgeon involvement and automated steps that could serve as a conceptual basis for the future development of an automated surgical planning computer algorithm.

### **4.4 Materials and Methods**

An iterative design process was used to develop virtual workflows in this study. The first step was creating a framework for a virtual fronto-orbital advancement (FOA) using the software available at the study institution. In-house workflow development adhered to the accessibility and cost-effective design criteria as the costs of outsourcing development were avoided. This

initial framework is referred to as the ‘manual workflow design’ in this chapter. This reflects the need for direct surgeon involvement for all steps of the workflow. The workflow is dependent on a surgeon making repeated subjective decisions on how to improve skull shape and guide the planning process. In subsequent iterations, categorized in this chapter under ‘partially automated workflow design,’ certain steps in the workflow were automated by introducing techniques such as Boolean operations and registration. These automated steps reduce the direct involvement of the surgeon and therefore reduce the amount of guesswork involved for surgical planning. All of the fifteen automated workflow iterations vary in the degree of surgeon involvement required. There are iterations that follow a rigid algorithm design requiring zero subjective input from the surgeon, and others that follow a semi-rigid paradigm and require a degree of surgeon guidance in the planning process. Reconstruction success was determined by comparing reconstruction models to preoperative skull models as well as normal control skull models. In general, a skull that is reconstructed to be closer in shape to a normal skull, and further in shape to the preoperative dysmorphic state, represents a successful reconstruction.

#### ***4.4.1 Participants***

A single case feasibility design was used to pilot the manual and automated workflow development. Both workflows were designed using Geomagics FreeformPlus software (Version 2017). The pilot case was a three-month-old female with right-sided UCS, and an age and sex-matched normal skull was used for the comparison in the automated workflow. CT scans were identified using a local radiology database. The same steps previously described to generate 3D skull models were used in this study (Robertson et al., 2020). The skull models were exported as stereolithography (STL) files and imported into Geomagics Freeform.

#### ***4.4.2 Manual Workflow Design***

##### **4.4.2.1 Step 1: Importing Skull Models**

A registered normal and UCS skull is imported into FreeformPlus (Version 2017). In Figure 1, the calvariae of the UCS and the normal skull models are shown from an anterior view and a bird’s eye view. The flattened frontal bone on the synostotic side of the UCS skull is especially apparent in the bird’s eye view.

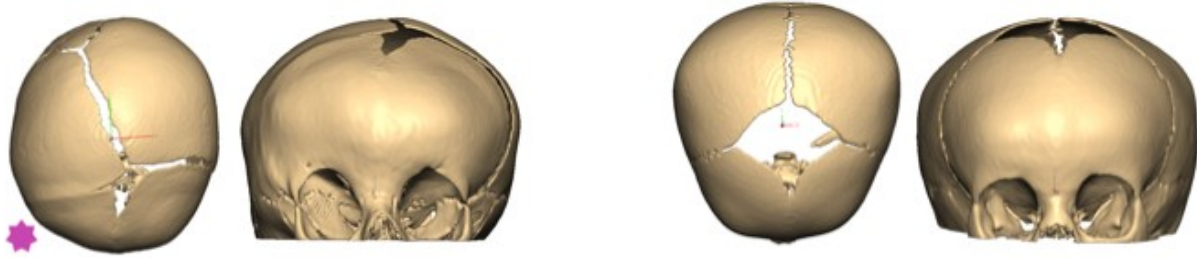


**Figure 4.1** The UCS skull (left) is shown in the bird's eye view and frontal view. The normal control skull (right) is shown in the same views. The frontal bone on the side with the fused suture in the UCS skull (pink star) is flattened when compared to the contralateral side and the normal control.

#### 4.4.2.2 Step 2: Isolating the SOB

Next, the Select Clay tool is used to highlight the SOB, as shown in Figure 2. The lasso and square select tool are used. The Square tool easily allows for a horizontal plane at the superior margin of the SOB, and the Lasso select tool allows for precise adjustments to be made. For example, the osteotomies made at the superior orbital roof can be detailed with the Lasso select tool. The ruler is used to ensure the distance between the superior margin of the SOB and the superior margin of the orbit is approximately one centimeter.

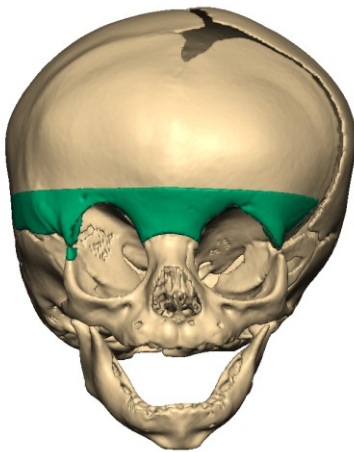


**Figure 4.2** The SOB (green) is virtually selected using the Lasso and Square Select Clay tools.

#### 4.4.2.3 Step 3: Isolating the Frontal Bones

The same tools in step two are used to isolate the frontal bones. The right and left frontal bones may be virtually osteotomized as one piece, or as separate pieces. The same is true for the SOB.

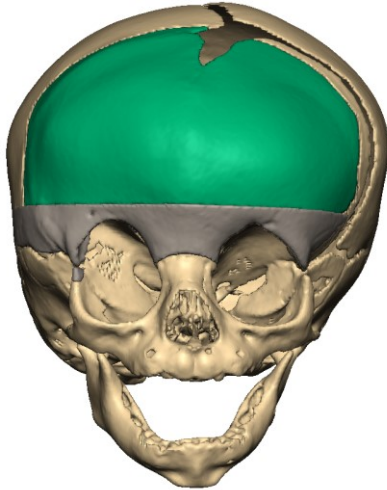


**Figure 4.3** The right and left frontal bones (green) are selected using the lasso and square select clay tools.

#### 4.4.2.4 Step 4: Virtual Osteotomies

Once the SOB and the frontal bones are isolated, they are virtually osteotomized by deleting them from the original skull model and copy/pasting them as new pieces. These pieces can be advanced, rotated, translated, switched from right to left, and bent as needed to approximate a normal head shape. The normal skull model can be made transparent to use as a guide. Figure 4 shows the SOB, and the frontal bones removed from the skull as a single piece, or separated into right and left pieces, and the resulting skull model.

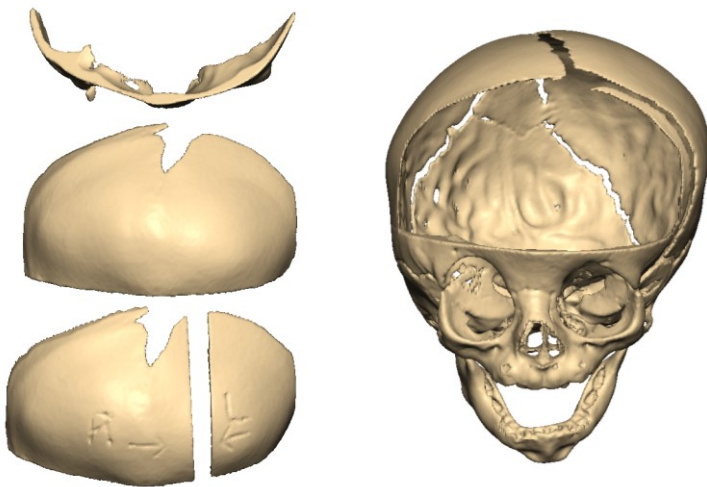


**Figure 4.4** Bone pieces osteotomized in a FOA surgery are removed from the skull model. The resulting skull model is shown on the right. This model is used to build the final reconstruction model. Note - only the frontal bones are removed in the skull pictured on the right. In a FOA procedure, both the SOB and the FBs would be removed, reshaped, and fixated.

#### 4.4.2.5 Step 5: Bone Manipulation

In this step, the pieces that are osteotomized in step four are manipulated to approximate the shape of the normal control skull. The Bend Clay tool can be used to bend the bony pieces, and the Reposition Clay tool can be used to translate, rotate, and exchange pieces from the right side to the left side. In Figure 5, the bend tool is shown reshaping the SOB.

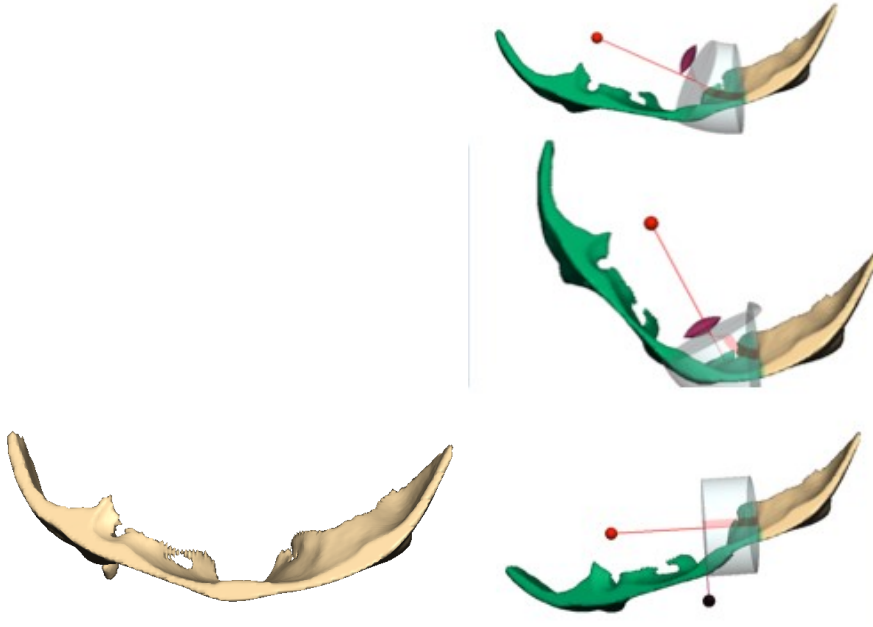


**Figure 4.5** The original SOB from the UCS skull is shown on the left. On the right, the Bend Clay tool is shown altering the shape of the SOB. The area in green is being manipulated virtually.

An example of a possible reconstruction is shown in Figure 6. In this example, the SOB is bent and advanced anteriorly. The right and left frontal bones are osteotomized separately, and rotated each 180 degrees. In addition, they are exchanged from the right side to the left side and vice versa.

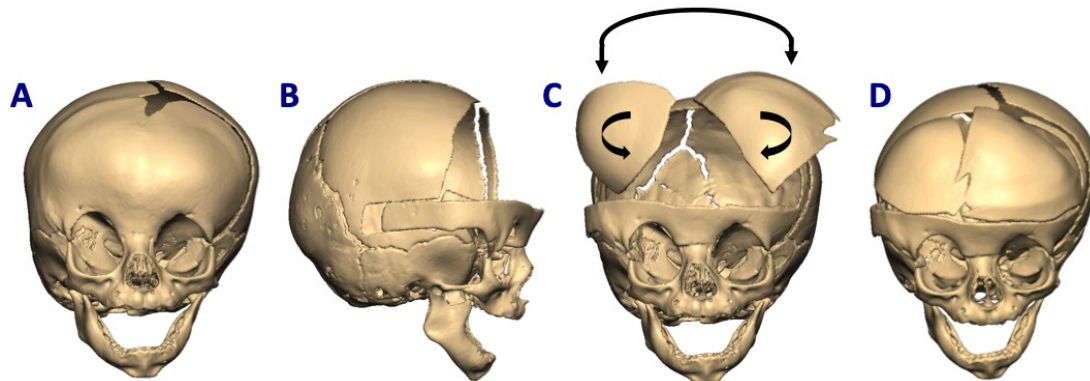


**Figure 4.6** An example of a FOA procedure for UCS is shown. Panel A is the preoperative skull model, and Panel D is the reconstruction model. In Panel B, the SOB is shown being translated anteriorly. In Panel C, the right and left frontal bones are being rotated, and exchanged from right to left.

A summary of the manual virtual workflow for an example of a FOA procedure is shown in Figure 7.

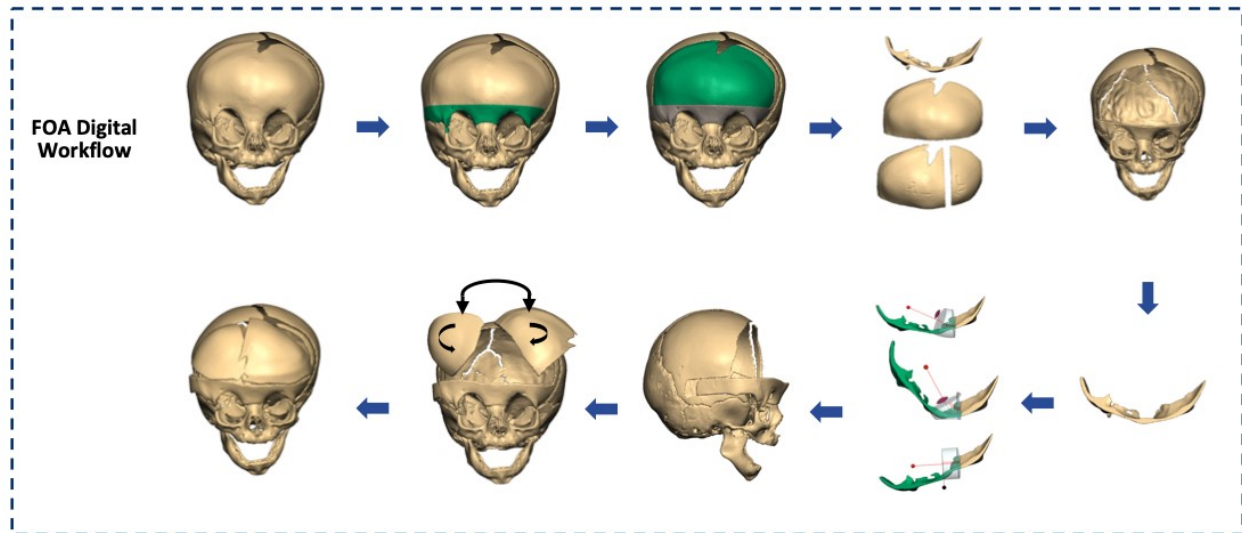


**Figure 4.7** The virtual workflow for a FOA procedure in a patient with UCS is shown. This is one example of how the bone components can be manipulated in order to approximate a normal head shape.

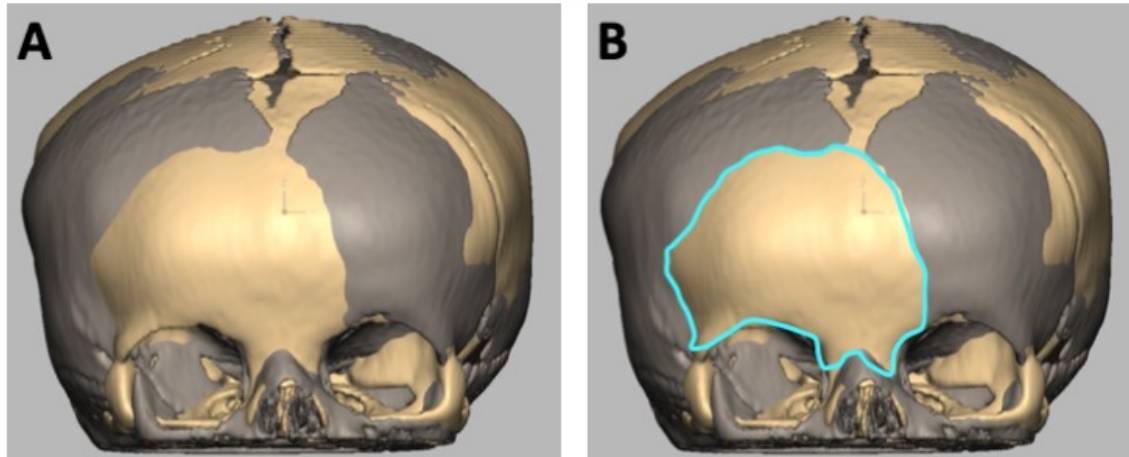
#### 4.4.3 Partially Automated Workflow Design

The key concept behind introducing automation into the virtual workflow for FOA is the use of Boolean functions and registration of key regions of interest (ROIs) to reshape a UCS skull. The ROIs for an FOA are the SOB and the frontal bones (FBs). These pieces are mobilized using the manual workflow previously described. The ROIs are registered to the control skull in an effort to achieve a UCS reconstruction model that more closely approximates a normal head shape compared to the preoperative model. The registration function in FreeformPlus (Version 2017) automatically positions an ROI in relation to the reference skull by minimizing the surface distances between each model. This eliminates the need for a surgeon to manually outline and advance the FB and SOB.

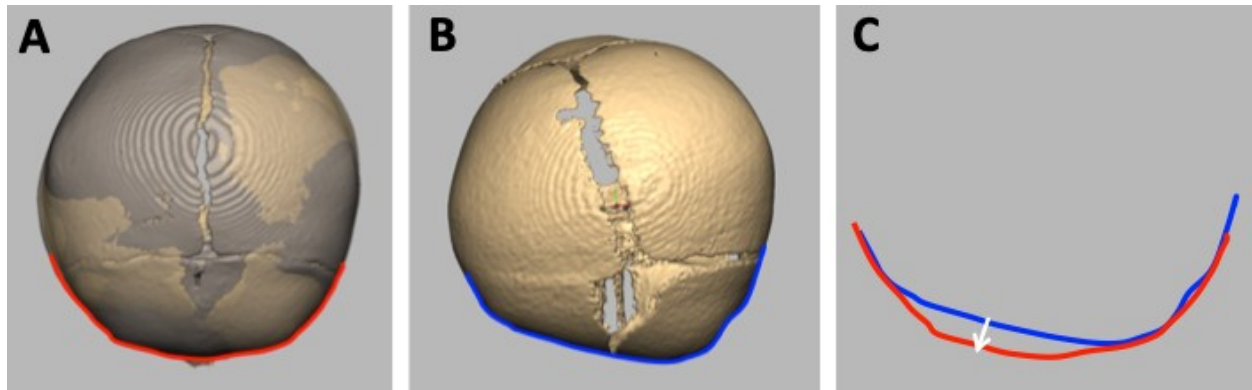
Fifteen iterations of the automated workflow design were executed. Key components of the iterations involve Boolean functions to delineate the FB ROI, SOB ROI, and registration of the ROIs.

#### 4.4.3.1 Frontal Bone Region of Interest

When the UCS and the control skulls are registered, the region of the UCS skull that is more retruded compared to the control skull is apparent (Figure 8). On a bird's eye view, this area of retrusion is also visible (Figure 9).

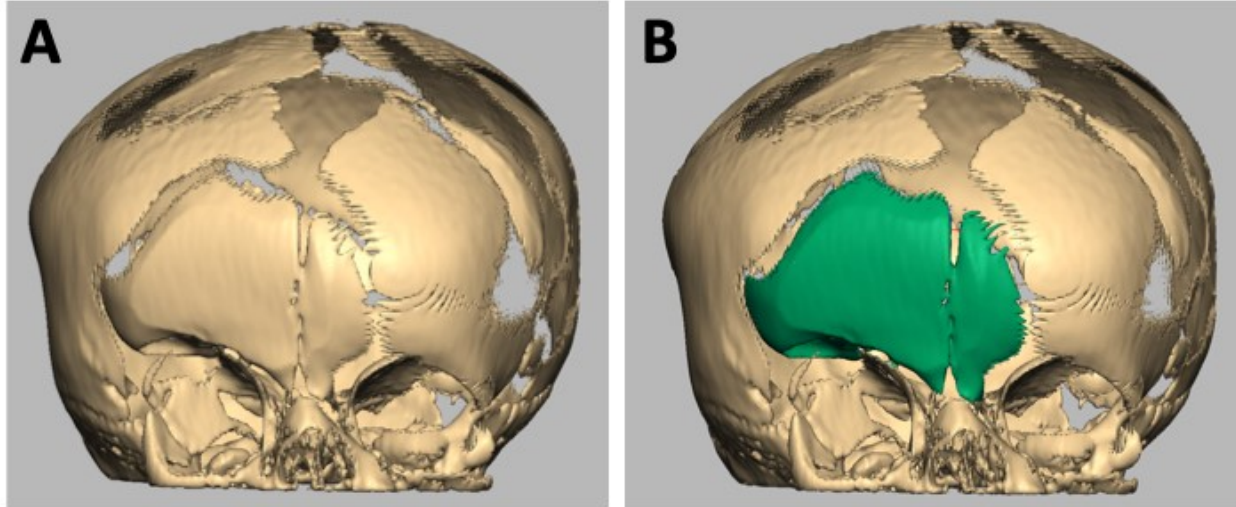


**Figure 4.8** In Panel A, the UCS skull model (grey) and the control skull model (beige) are shown registered to each other. The area at the frontal bones where the grey skull is posteriorly positioned compared to the beige skull is apparent. This region is outlined in blue in Panel B.



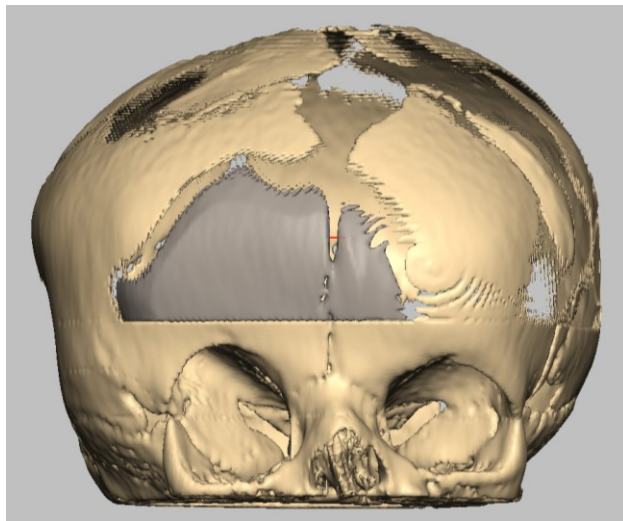
**Figure 4.9** In Panel A, a bird's eye view of the UCS skull and the control skull registered to each other is shown. The red line outlines the contour of the normal skull forehead. In Panel B, a bird's eye view of the UCS skull is shown. In Panel C, the area where the UCS forehead is retruded compared to the control skull is apparent. The white arrow highlights the anterior translation of the frontal bones that a surgeon aims to achieve in UCS with an FOA procedure.

The Boolean Subtraction function is used in Freeform to remove the control skull from the UCS skull. This removes bone from the UCS skull where it was intersecting or overlapping with the control skull, highlighting the FB ROI, as shown in Figure 10.



**Figure 4.10** In Panel A, the UCS skull is shown after the control skull is subtracted from it using the Freeform Boolean function. The gaps in the skull model are areas where the normal skull intersected or overlapped with the UCS skull. The FB ROI is highlighted in green in Panel B.

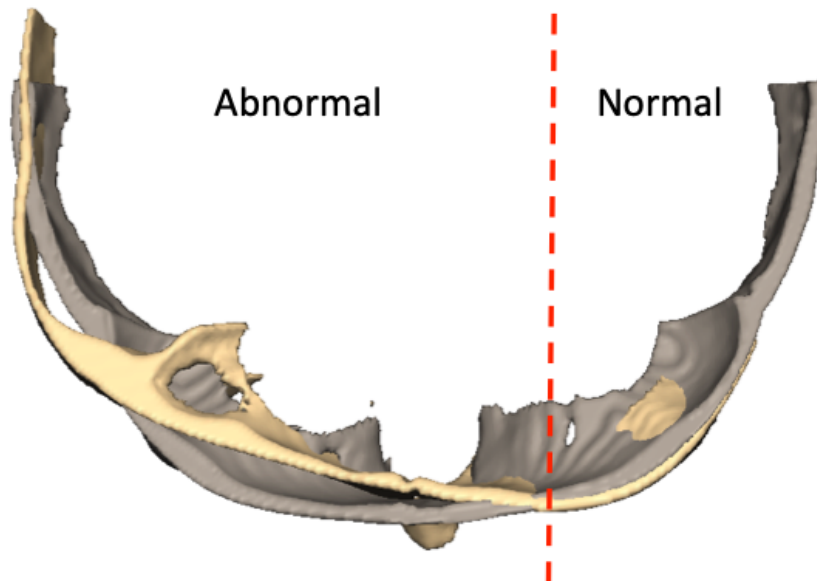
In the later iterations of the partially automated workflow, the SOB and FB ROIs were distinguished from each other. With that distinction, the automatically derived FB ROI is refined so that it does not cross the superior margin of the SOB (Figure 11). This margin is placed about one centimeter superior from the superior orbital rim on the affected side. In the case example, this is the right side.



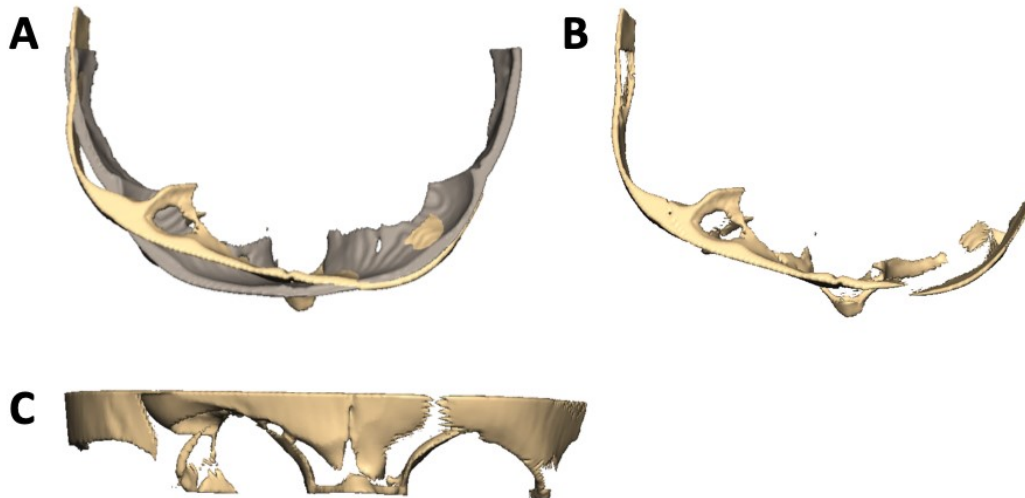
**Figure 4.11** With the SOB ROI defined, the FB ROI (grey) is refined with an inferior margin that does not cross the superior margin of the SOB.

#### 4.4.3.2 Supra-Orbital Bar Region of Interest

The SOB ROI is outlined using the same method as described above in the manual workflow. The SOB ROI was separated into two components: the abnormal side, corresponding to the retruded portion of the SOB when compared to the normal SOB, and the normal side, corresponding to the well-registered portion of the SOB when compared to the normal SOB (Figure 12). This was done in an attempt to improve the registration of the SOB to the normal SOB. Because the normal component of the SOB was well registered to the normal SOB reference, there was limited movement of the SOB when attempting to automate the advancement. However, due to the increased irregularity of the SOB shape and differences in registration to the normal skull, this resulted in a SOB with various areas of missing bone, which does not simulate a realistic surgical scenario (Figure 13).

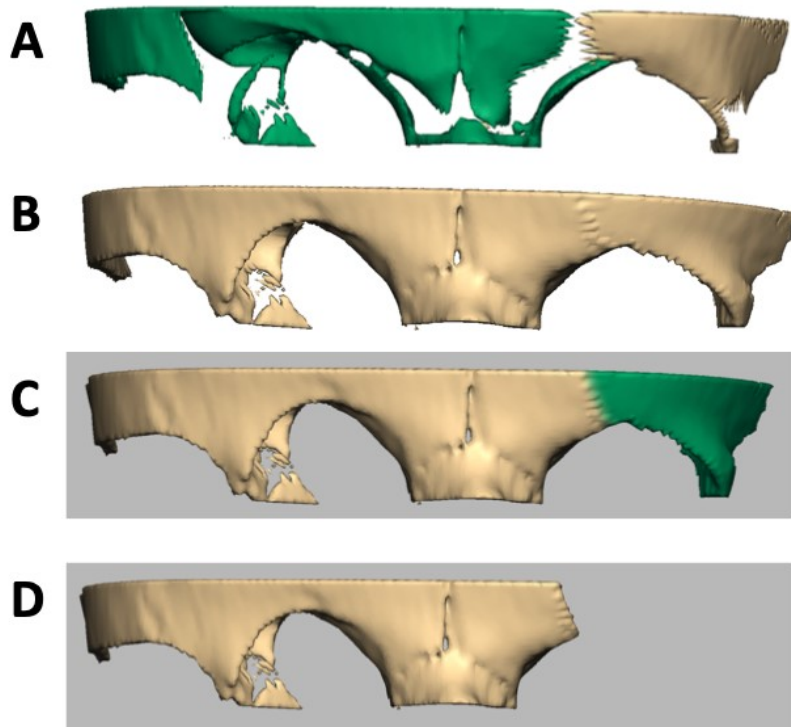


**Figure 4.12** The UCS SOB (beige) is registered to the control SOB (grey). On the patient's left side, which corresponds to the non-synostotic side of the skull, the UCS SOB is registered well to the control SOB. Areas that are well registered have good bony overlap between the grey and the beige skulls. On the patient's right side, corresponding to the synostotic side, the UCS SOB is clearly retruded compared to the control SOB and is not well registered. The distinction between the abnormal and normal components of the UCS SOB (red line) is the point where the UCS SOB transitions from being well registered to the control SOB, to where it is not well registered to the control SOB.



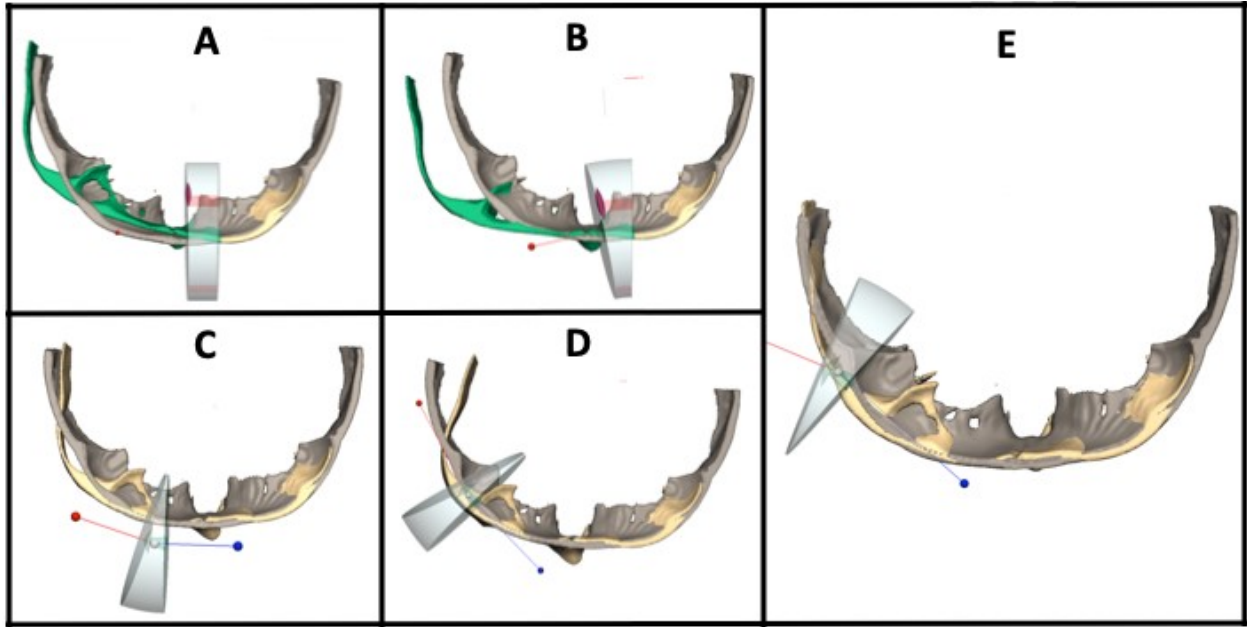
**Figure 4.13** In A, the UCS SOB (beige) and the control SOB (grey) are registered and shown from a bird's eye view. In B, the control SOB is subtracted from the UCS SOB via a Boolean function. Panel C demonstrates the problematic resulting UCS SOB with the various areas of missing bone.

To overcome this problem, a manual step is introduced. Boolean subtracting the normal component from the entire SOB automatically delineates the abnormal components of the UCS SOB. This resulted in a depression in the UCS SOB that identified the transition between the normal and abnormal SOB (Figure 14). This depression is used as the boundary when manually selecting and then deleting the normal component of the SOB to form a refined SOB ROI. In later iterations, the normal component was not removed from the UCS SOB, and this boundary was used to determine where to make the initial bend in the SOB. In this context, normal and abnormal components are referring to the UCS SOB. Therefore, the SOB is still from an abnormal UCS skull. Normal and abnormal refer to components of the SOB that are well registered and non-well registered to a control reference SOB, respectively. How well a ROI is registered is determined based on a three-dimensional, qualitative, visual assessment by the software user.



**Figure 4.14** Panel A – the UCS SOB after the control SOB is subtracted from it results in excessive bone loss. The green portion is the abnormal component of the SOB, and the area of interest when recreating a normal SOB. Panel B – subtracting the normal component of the SOB from the abnormal component results in a depression. Panel C – the distinction between the normal and abnormal SOB components is identified and used as the boundary to select the normal component. Panel D – the abnormal SOB ROI remains and is used in multiple iterations to approximate a normal SOB.

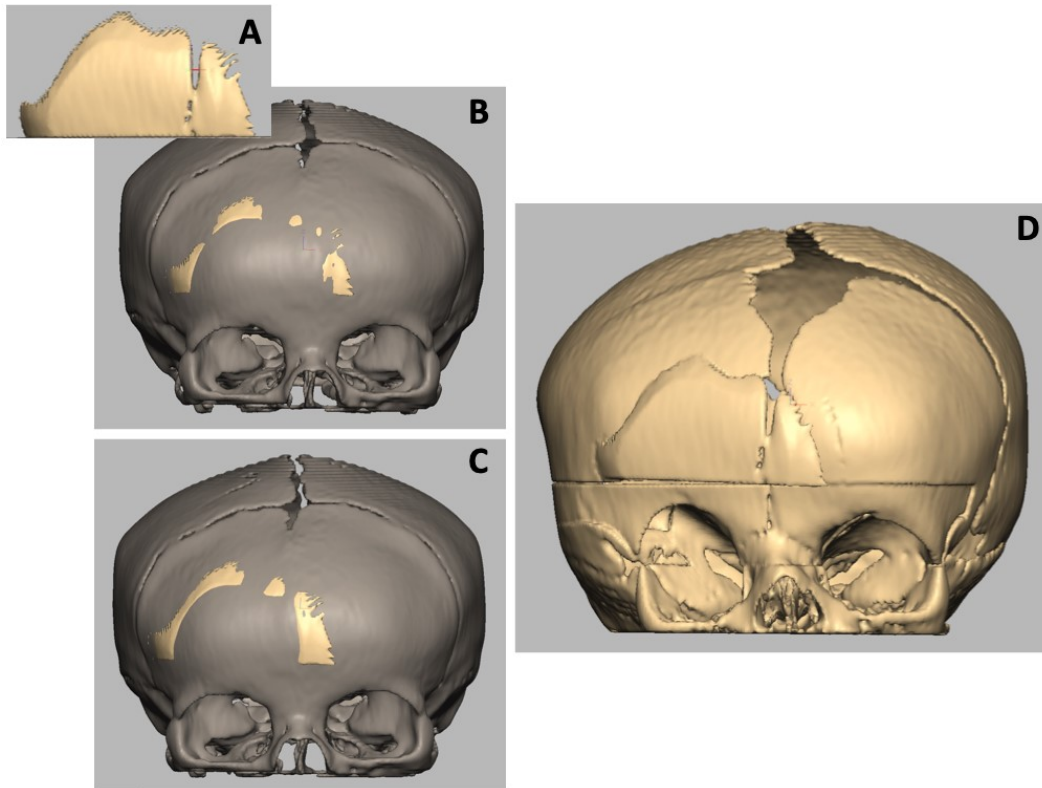
In some iterations, a bend was introduced into the workflow to reshape the SOB. The method in Figure 14 to define the transition point between the normal and abnormal SOB components is used to identify where to make the first bend in the SOB (Figure 15).



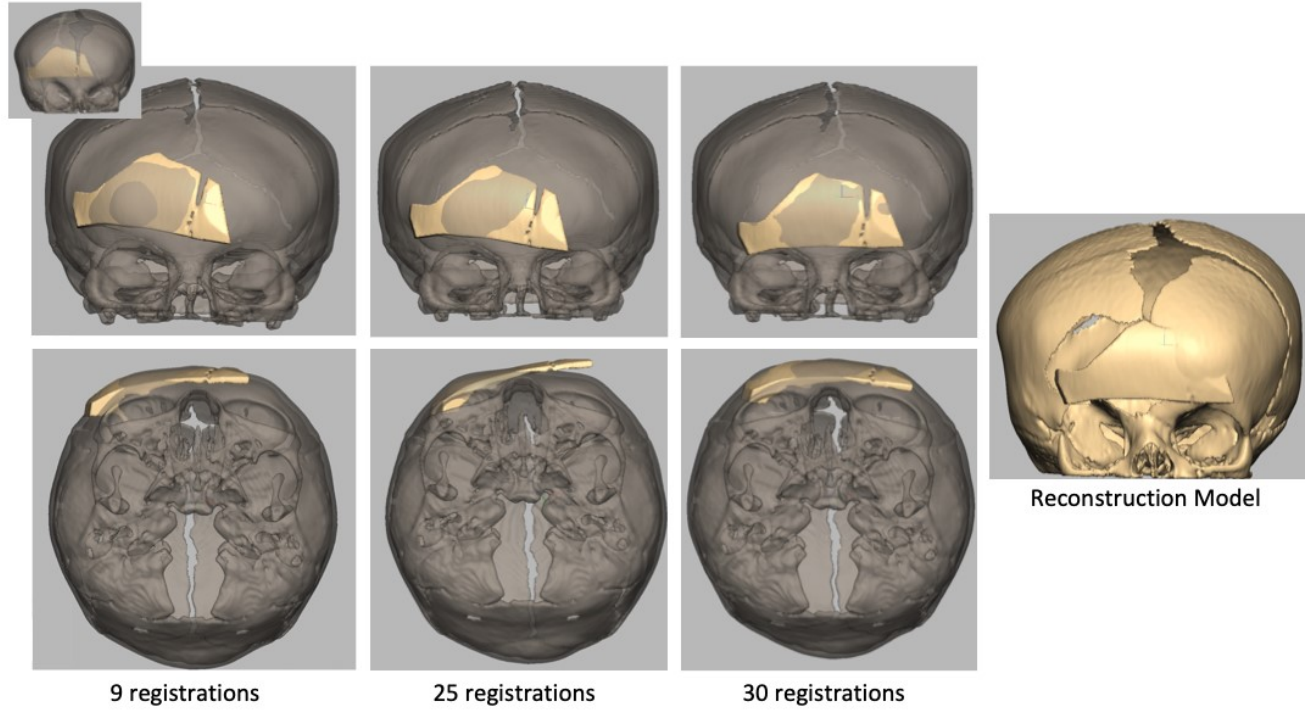
**Figure 4.15** Panel A – the intersection between the normal and abnormal SOB is used to define where to initially bend the SOB. Panel B – The SOB after the first bend. Panel C – the SOB after the second bend. Panel D – the SOB after the third bend. Panel E – the final reconstructed SOB after the fourth bend.

#### 4.4.3.3 Registration of Regions of Interest

Once the FB and SOB ROIs are determined, the registration function in Freeform is used to optimize their position in relation to the control skull. The goal is to have the UCS FB and SOB automatically move to a position that most closely resembles a normal forehead contour. The stop criterion for the registration is when the ROI has stopped moving after two consecutive registration attempts. Movement is determined as a visually apparent change as determined by the workflow operator. The visually noticeable assessment was chosen because if the ROI does not move a degree that is clearly visualized, it is not likely to have made a clinically meaningful change in position. Figure 16 demonstrates the registration of the FB ROI in workflow iteration #3. In this example, the FB makes a very minimally noticeable advancement after registration. Conversely, in iteration #2, the FB ROI was a slightly different shape, and the degree of advancement after 30 registrations is very noticeable (Figure 17). As a result, the contour of the forehead in the reconstruction model for iteration #2 is similar to the contour of the control forehead. A summary of the 15 automated workflow iterations key features, pros, cons, and reconstruction models are outlined in Table 1. Reconstruction models were built using the union Boolean operation, combining the FBs, SOB, and remaining skull model.

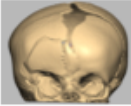
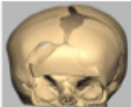
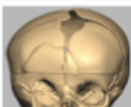
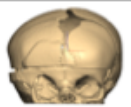
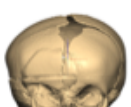
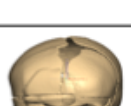
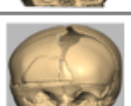


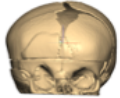
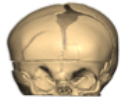
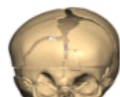
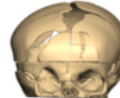
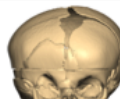
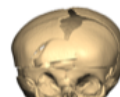
**Figure 4.16** In iteration #3 of the automated workflow, the FB ROI does not make a large visibly noticeable advancement. Panel A depicts the RB ROI. Panel B demonstrates the FB ROI (beige) after the first registration to the control skull (grey). Prior to registration, no part of the beige ROI was visible in front of the control skull. Panel C shows the FB ROI after the tenth and final registration. It is noticeable that the surface area of the beige FB ROI that is in front of the grey control skull has increased when compared to Panel B. This indicates that the FB ROI advanced further between registrations one and ten. Panel D shows the final reconstruction model.



**Figure 4.17** In iteration #2 of the automated workflow, the FB ROI (beige) makes a visibly noticeable advancement, translation, and rotation to approximate the shape of the control skull (grey) forehead. The improved contour of the forehead is noticeable on the worm's eye view of the skull models. In the top left image, the UCS FB ROI (beige) is seen completely posterior to the control skull forehead, which is transparent in these images in order to visualize the FB ROI throughout the registrations. There were no changes made to the SOB in this reconstruction model.

**Table 4.1** Summary of the 15 iterations of the partially automated workflow.

Work-flow Iteration #	Key Points	Pros	Cons	Reconstruction Model
1	<ul style="list-style-type: none"> <li>• FB ROI is automatically highlighted by Boolean function</li> <li>• Identified ROI is registered to the control skull</li> </ul>	<ul style="list-style-type: none"> <li>• Fully automated</li> </ul>	<ul style="list-style-type: none"> <li>• Minimal FB advancement achieved</li> <li>• SOB &amp; FB not separated</li> </ul>	
2	<ul style="list-style-type: none"> <li>• FB ROI is automatically highlighted by Boolean</li> <li>• Polygon Select Clay tool used to trace out highlighted area</li> </ul>	<ul style="list-style-type: none"> <li>• Obeyed typical surgical boundaries (i.e. 1 cm above supra-orbital rim)</li> <li>• FB piece advanced further than iteration #1</li> </ul>	<ul style="list-style-type: none"> <li>• Not fully automated</li> <li>• FB ROI manually traced out based on area suggested by Boolean function</li> </ul>	
3	<ul style="list-style-type: none"> <li>• FB ROI and SOB ROI are separated and registered to the control skull individually</li> </ul>	<ul style="list-style-type: none"> <li>• Better simulation of real-life surgical scenario</li> </ul>	<ul style="list-style-type: none"> <li>• Minimal FB and SOB advancement</li> <li>• FB does not abut SOB</li> </ul>	
4	<ul style="list-style-type: none"> <li>• FB ROI and SOB ROI are registered to a control FB and a control SOB, versus the whole control skull</li> </ul>	<ul style="list-style-type: none"> <li>• Reasonable degree of advancement</li> </ul>	<ul style="list-style-type: none"> <li>• UCS SOB rotated out of the horizontal plane</li> <li>• FB does not abut SOB</li> </ul>	
5	<ul style="list-style-type: none"> <li>• Control SOB was refined using the same parameters for the UCS SOB</li> </ul>	<ul style="list-style-type: none"> <li>• More realistic reference</li> </ul>	<ul style="list-style-type: none"> <li>• No difference appreciated</li> </ul>	
6	<ul style="list-style-type: none"> <li>• SOB ROI was separated into 2 components: abnormal and normal</li> <li>• Boolean function used to determine abnormal and normal components</li> </ul>	<ul style="list-style-type: none"> <li>• SOB advanced further</li> </ul>	<ul style="list-style-type: none"> <li>• Boolean function creates large gaps in the SOB</li> <li>• Abnormal SOB component rotates out of plane</li> </ul>	
7	<ul style="list-style-type: none"> <li>• Attempt to improve automatic separation of abnormal and normal SOB components</li> </ul>	<ul style="list-style-type: none"> <li>• Fewer gaps in the SOB ROI</li> <li>• Fully automated</li> </ul>	<ul style="list-style-type: none"> <li>• FB does not abut SOB</li> <li>• FB and SOB pieces are not clean</li> </ul>	
8	<ul style="list-style-type: none"> <li>• Attempt to improve automatic separation of abnormal and normal SOB components into cleaner pieces</li> </ul>	<ul style="list-style-type: none"> <li>• SOB advanced further</li> <li>• Cleaner SOB components</li> </ul>	<ul style="list-style-type: none"> <li>• Had to separate components manually based on Boolean overlap</li> </ul>	

9	<ul style="list-style-type: none"> <li>Added Bend Clay function to SOB</li> </ul>	<ul style="list-style-type: none"> <li>SOB shape is much more similar to normal control</li> </ul>	<ul style="list-style-type: none"> <li>Bend component not automated</li> <li>Separating SOB components not automated</li> </ul>	
10	<ul style="list-style-type: none"> <li>Smooth edges of FB ROI</li> <li>Make FB ROI larger than automatically defined piece</li> </ul>	<ul style="list-style-type: none"> <li>Do not lose bone from Boolean subtraction</li> </ul>	<ul style="list-style-type: none"> <li>Not fully automated</li> <li>Negligible advancement of FB</li> </ul>	
11	<ul style="list-style-type: none"> <li>Remove small spicule of SOB in FB ROI from iteration #10</li> </ul>	<ul style="list-style-type: none"> <li>More realistic anatomical boundaries</li> </ul>	<ul style="list-style-type: none"> <li>No difference appreciated</li> </ul>	
12	<ul style="list-style-type: none"> <li>Register FB ROI to whole control skull versus FB ROI of control</li> <li>FB ROI manually delineated</li> </ul>	<ul style="list-style-type: none"> <li>A lot of movement in FB including rotation</li> </ul>	<ul style="list-style-type: none"> <li>Multiple iterations (66 registrations)</li> <li>Not fully automated</li> </ul>	
13	<ul style="list-style-type: none"> <li>Register FB ROI to whole control skull</li> <li>FB ROI automatically delineated</li> </ul>	<ul style="list-style-type: none"> <li>May simulate real-life scenario better than #12 as bone is lost with osteotomies</li> </ul>	<ul style="list-style-type: none"> <li>Less advancement than with larger piece</li> </ul>	
14	<ul style="list-style-type: none"> <li>Manually advanced FB ~1 cm</li> </ul>	<ul style="list-style-type: none"> <li>FB ROI registers well to the control FB</li> </ul>	<ul style="list-style-type: none"> <li>Not fully automated – adding more manual components</li> <li>Multiple iterations (40)</li> </ul>	
15	<ul style="list-style-type: none"> <li>Entire FB osteotomized, including ROI highlighted with Boolean function</li> <li>Bone graft used to fill gaps</li> </ul>	<ul style="list-style-type: none"> <li>Most similar to real-life scenario</li> <li>A lot of FB movement</li> <li>Acceptable result</li> </ul>	<ul style="list-style-type: none"> <li>Least automated of all iterations</li> </ul>	

#### 4.4.4 Analysis

The manual VSP workflow was analysed using Geomagic Control (Version 2015.3.1.0). Maximum Hausdorff surface distances were calculated at four points along the forehead in the reconstruction skull model compared to the control skull model. These points (Figure 18) are approximate points that represent four quadrants of the bony forehead. Points A and B are measured at the right and left SOB, and points C and D are measured at the right and left frontal bones, respectively. The root mean squared error (RMSE) of the maximum surface distances at each point was calculated using the equation below.

$$X_{\text{rmse}} = \sqrt{[(x_A^2 + x_B^2 + x_C^2 + x_D^2)/4]}$$

A smaller RMSE represents a model whose forehead quadrants are closer in shape to a normal reference skull than the preoperative UCS skull. Therefore, a smaller RMSE value represented a successful reconstruction and a surgical workflow that leads to a successful virtual operation. In addition, color maps were generated in Geomagic Control to qualitatively assess the improvement in skull morphology at the frontal bones and superior orbital bar. Lastly, input from

an expert surgeon was obtained to assess the fidelity of the virtual surgical workflow. Each workflow step was carefully reviewed to ensure they simulated real-life operative procedures as closely as possible.

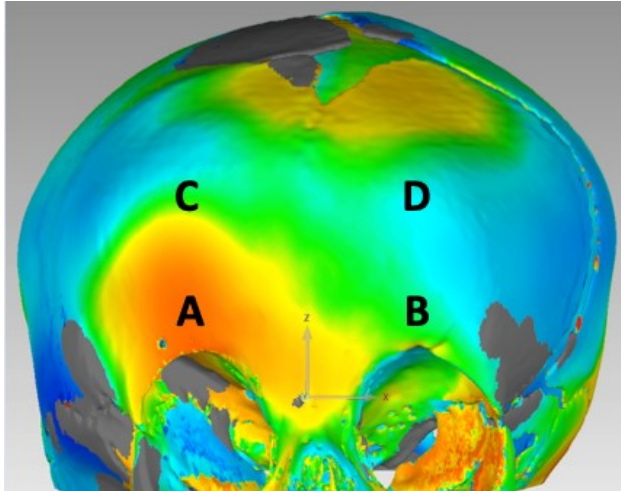


**Figure 4.18** Points A and B represent the right and left SOB of the skull model, and points C and D represent the right and left frontal bones, respectively. These represent the four points where maximum Hausdorff surface distance measurements were taken to analyse the shape of the virtually reconstructed skull.

Results for the automated workflow were analysed in 3D Slicer (Version 10.2). The Model To Model Distance and Mesh Stats modules were used to calculate the maximum Hausdorff surface distances between the reconstruction models and the preoperative UCS skull at the SOB and the frontal bones. This was done to assess the degree of advancement of the bony components. The same method was used to calculate distances between the reconstruction models and the normal control skull, to assess the similarity between the reconstruction model and normal skull morphology. Skulls that had a large surface distance value in comparison to the preoperative skull, and small surface distance values in comparison to the normal skull were considered successful reconstructions. In addition, color maps for all skull reconstruction models were generated using the Shape Population Viewer module to qualitatively assess the skull morphology.

## 4.5 Results

### 4.5.1 Manual Workflow Design

The RMSE of the maximum surface distance values for the preoperative UCS skull was 3.28 mm, and the value for the model reconstructed using the manual virtual workflow was smaller at 1.38 mm (Table 2). The overall improvement in the forehead contour in the reconstruction model is appreciated by the color map comparison of the two models (Figure 19). In the surface distance comparison of the UCS skull and the control skull, there is a clear asymmetry in the distribution of color, with an orange/yellow area above the right orbit that is not present above the left orbit. Conversely, in the surface distance comparison of the reconstruction skull to the control skull, the distribution of warm and cool colors is more symmetrical, with warmer tones being central and cooler tones presenting laterally (Figure 19). The improvement in the RMSE values and the symmetry of the reconstruction model indicate that the manual virtual workflow produced a skull model that is closer in shape to a normal skull compared to the preoperative shape. The workflow steps were reviewed with a surgeon specializing in pediatric craniomaxillofacial reconstruction and were deemed to be a reasonable representation of real-life surgical steps.

**Table 4.2** Summary of maximum Hausdorff surface distances between the preoperative UCS skull model and a control skull, and the postoperative reconstruction UCS model and a control skull. The reconstruction skull was created using a manual VSP.

Skull Points	Surface Distances (mm)				RMSE (mm)
	A	B	C	D	
Pre-Op	-6.32	-0.54	-1.20	-1.24	3.28
Post-Op	2.64	0.62	-0.05	-0.55	1.38

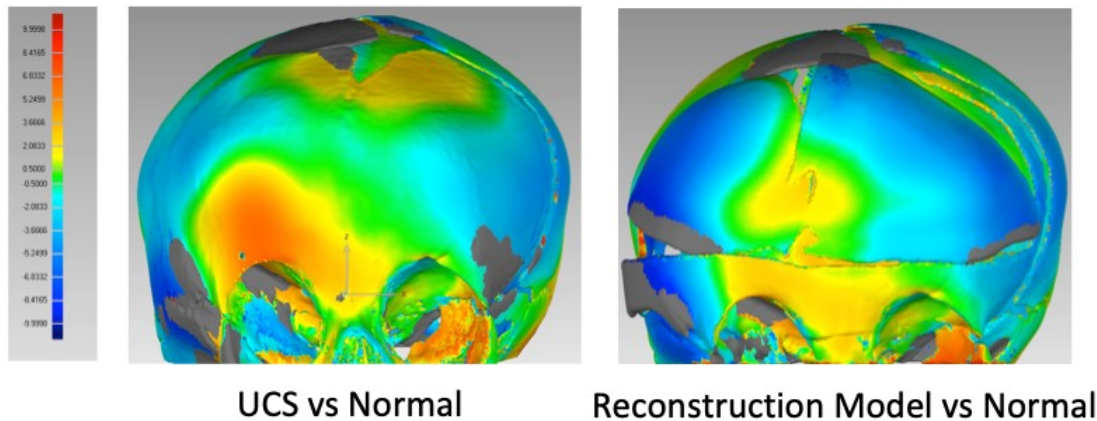


**Figure 4.19** Color maps displaying surface distances values between the preoperative UCS skull model and the control skull (left), and the reconstruction UCS skull model and the control skull (right). Warmer tones represent larger distances between the skull model and a normal skull, representing areas that are less similar to a normal skull than cooler tones.

#### ***4.5.2 Automated Workflow Design***

The results for the 15 reconstruction models compared to the preoperative UCS skull model are listed in Table 3. The model with the largest surface distance compared to the preoperative model at the FB was #14, with advancement of 10.478 mm. Models #15 and #12 had the second and third largest values for the FB advancement at 10.407 mm and 8.427 mm, respectively. The model with the largest surface distance compared to the preoperative model at the SOB was #11, with a maximum advancement of 7.889 mm. Models #9 and #10 had the second largest value at the SOB with an advancement of 7.887 mm.

The models that achieved the smallest degree of advancement for the FB and SOB were #11 (3.089 mm) and #3 (-1.752 mm), respectively. The SOB in model #3 had a maximum surface distance value that was negative, indicating the SOB in the reconstruction model was even more retruded than in the preoperative scenario. The color maps displaying the maximum surface distance values are helpful in visualizing the virtual surgical changes (Figure 20).

**Table 3.** Maximum surface distance values between the FB and SOB of the reconstruction UCS model compared to the preoperative UCS model.

Recon Model #	Max Surface Distance Values (mm)	
	SOB	FB
1	N/A	4.611
2	N/A	7.768
3	-1.752	3.836
4	4.575	3.775
5	4.670	3.770
6	4.730	3.830
7	4.388	3.788
8	6.763	3.763
9	7.887	3.787
10	7.887	4.187
11	7.889	3.089
12	7.727	8.427
13	7.825	3.625
14	7.678	10.478
15	7.807	10.407

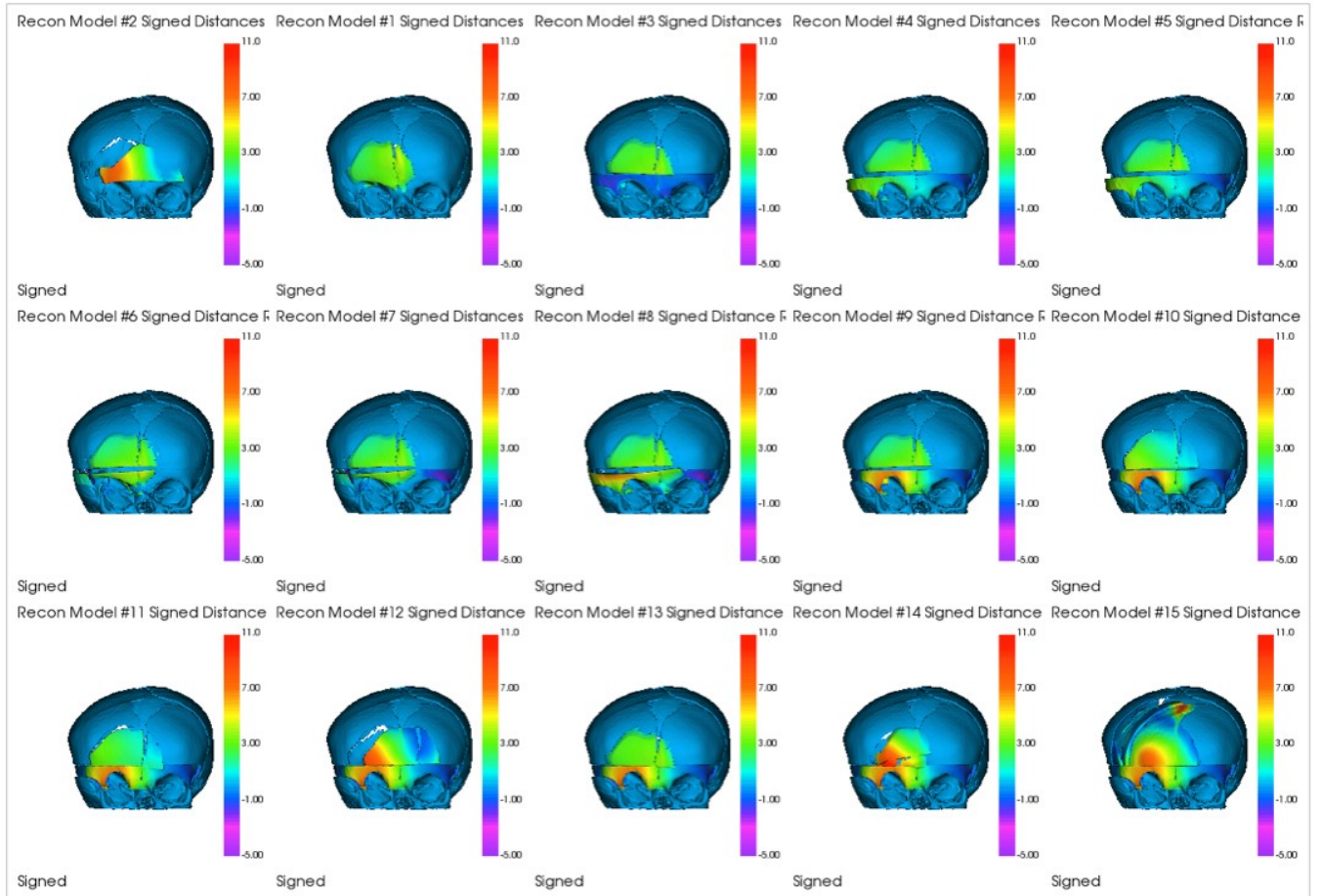


**Figure 4.20** Color maps depicting the maximum surface distances calculated between the preoperative UCS skulls and the reconstruction models demonstrate the virtual surgical changes.

The results for the 15 reconstruction models compared to the control skull model are listed in Table 4. Color maps were created for the frontal bone ROI (Figure 21) and the SOB ROI (Figure 22) compared to the corresponding control skull ROIs using the same scale as the comparison in Figure 20. The color maps for the comparison to the normal skulls were limited to the specific ROIs because the skulls do not register perfectly in multiple areas of using the whole skull since they are from different people. This is in contrast to the preoperative and postoperative comparison where all areas of the skull that are not manipulated line up well since both skull models are from the same patient. For the normal skull comparison, the average surface distance values are also of interest. For the previous comparison, the maximum amount of surgical advancement is of interest, and therefore, the maximum surface distance values are reported. In contrast, when comparing the reconstruction model to the control skull, how close the overall shape approximates a normal skull is of interest. In addition, the maximum value may

represent a small area of local deformity or artifact at the edge of a model or bone piece. For these reasons, the location where the maximum values were obtained was confirmed using the same method in Chapter 2. Therefore, the maximum and mean surface distance values are reported for the SOB and FOB of each reconstruction model.

**Table 4.4** Maximum and mean surface distance values between the FB and SOB of the reconstruction UCS model compared to the control skull model.

Recon Model #	Surface Distance Value (mm)			
	FB		SOB	
	Mean	Max	Mean	Max
1	0.346	5.431	N/A	N/A
2	0.103	1.257	N/A	N/A
3	0.476	5.299	0.999	7.619
4	0.523	5.344	1.778	10.838
5	0.551	5.344	2.031	10.880
6	0.530	5.344	0.638	8.08
7	0.534	5.344	0.421	7.401
8	0.287	4.197	1.027	9.574
9	0.516	5.344	0.456	5.400
10	0.712	4.928	0.502	6.186
11	0.852	5.493	0.618	6.280
12	0.015	1.186	0.475	6.113
13	0.491	5.238	0.516	6.395
14	-0.089	0.997	0.535	5.991
15	0.330	0.846	0.488	6.116

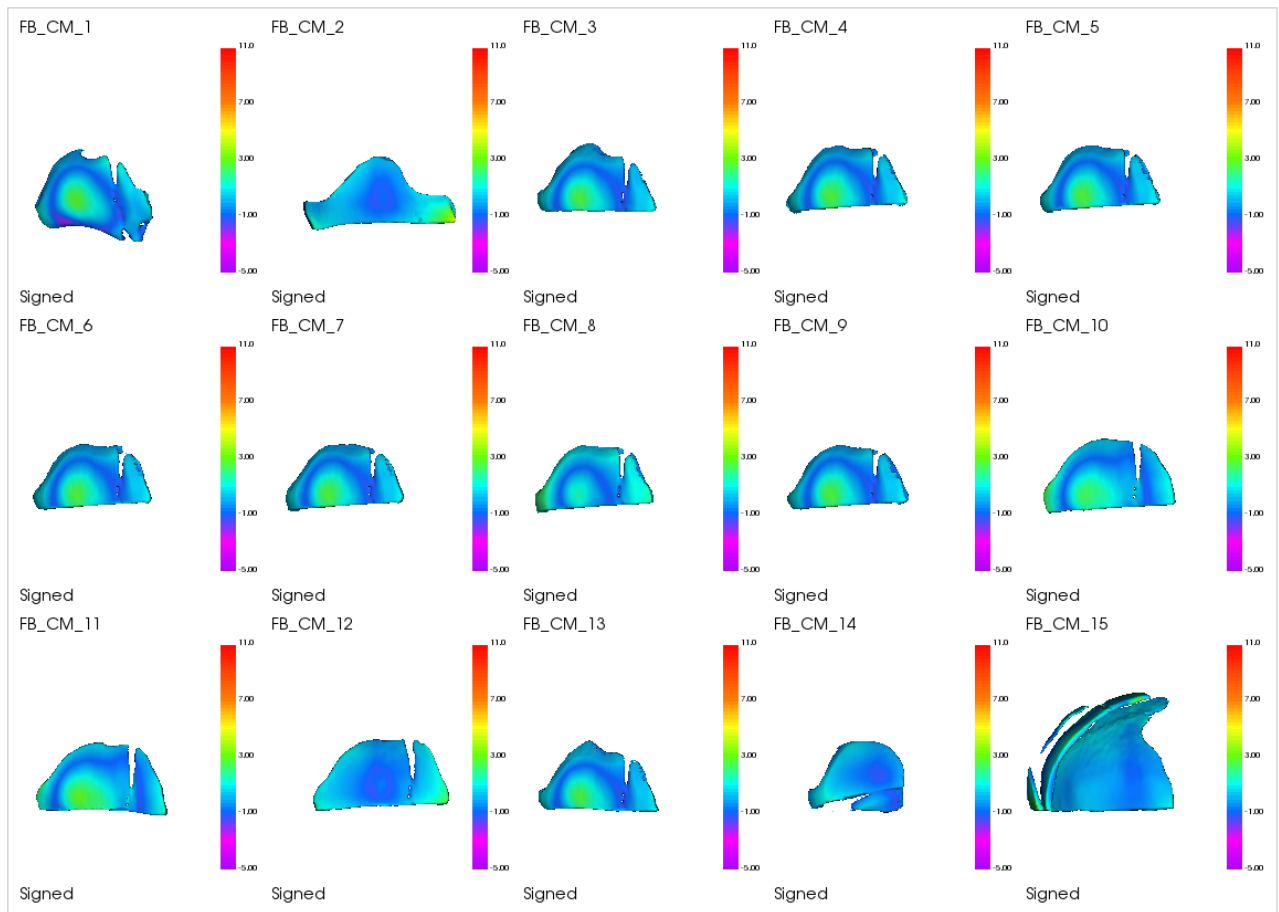


**Figure 4.21** Color maps for the FB ROI for the 15 reconstruction models are shown. Cooler tones indicate a small distance between skulls, and warmer tones indicate a larger distance. Frontal bones in this figure that are bluer are more similar to a normal reference skull, and frontal bones that have areas of green are less similar to a normal reference.

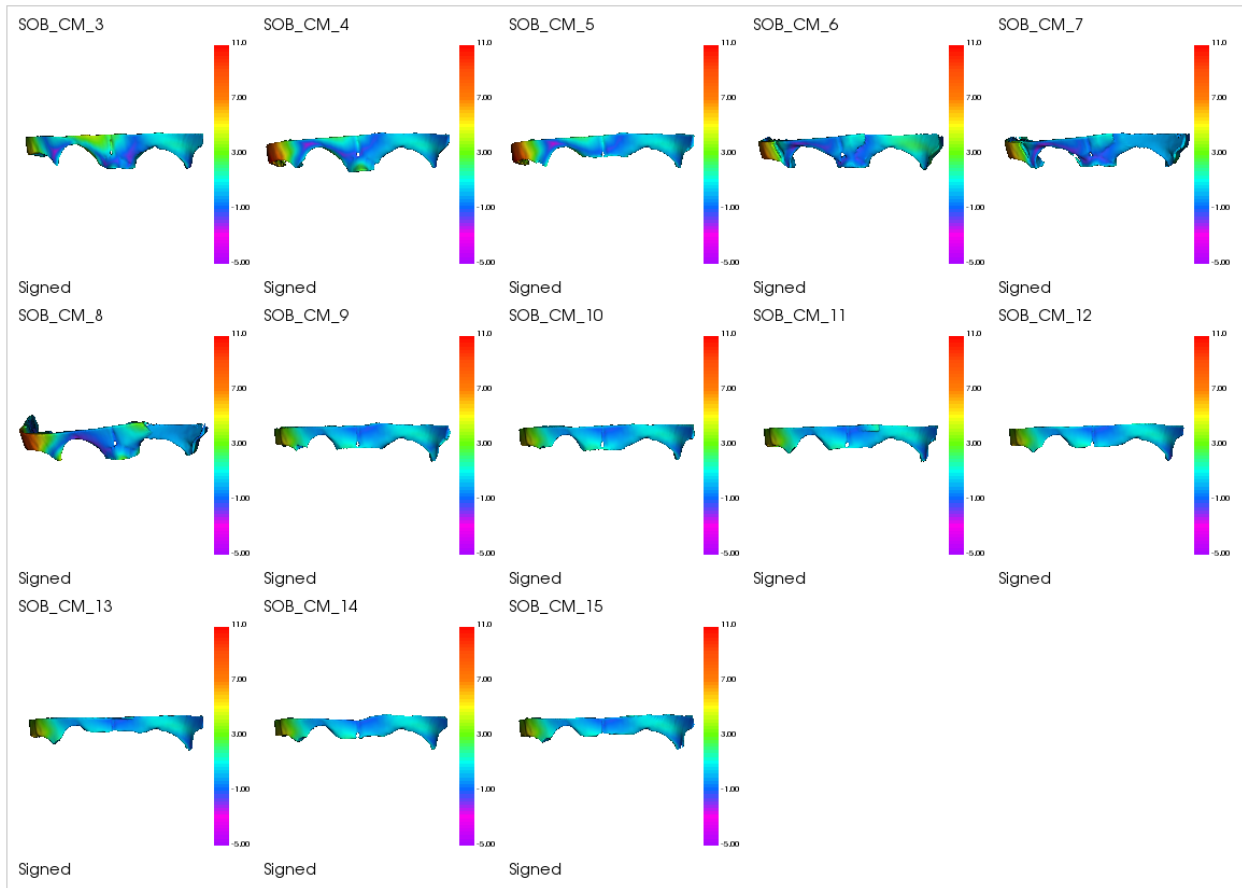


**Figure 4.22** Color maps for the SOB ROI for the 13 reconstruction models that isolated the SOB are shown. Cooler tones indicate a small distance between skulls, and warmer tones indicate a larger distance. Cooler tones indicate similarity to a normal reference skull, and warm tones indicate areas where the SOB was not close in shape to the normal reference.

The reconstruction models with the smallest mean surface distances compared to a control skull at the FB were #12 (0.015 mm), #14 (-0.089 mm), and #2 (0.103 mm). The reconstruction models with the smallest mean surface distances compared to a control skull at the SOB were #7 (0.421 mm), #9 (0.456 mm), and #12 (0.475 mm). These models achieved the closest FB and SOB shape to a control skull. On the other hand, reconstruction models that had the largest mean surface distances compared to a control skull and did not approximate a normal head shape very well were models #11 (0.852 mm), #10 (0.712 mm), and #5 (0.551 mm) for the FB, and models #5 (2.031 mm), #4 (1.778 mm) and #8 (1.027 mm) for the SOB.

Model #12 was the highest overall performer, and models #5 and #8 were the lowest overall performers. Model #12 was the only model that achieved advancement and normality in

both ROIs, whereas models #5 and #8 achieved poor advancement and poor normality in both ROIs (Table 5). All other models' successes were limited to either the frontal bone or the supra-orbital bar.

**Table 4.5** The highest and the lowest performing models are presented. Overall high performance was determined by highest degree of advancement and/or high degree of normalcy in both ROIs. Overall low performance was determined by lowest degree of advancement and/or low degree of normalcy in both ROIs.

	Recon Model Compared to Pre-Op Model		Recon Model Compared to Normal Model		
	FB	SOB	FB	SOB	
<b>Most Advancement</b>	14 15 12	11 9 10	12 14 2	7 9 12	<b>Most Normal</b>
<b>Least Advancement</b>	11 13 8	3 7 4	11 10 5	5 4 8	<b>Least Normal</b>

#### 4.6 Discussion

An in-house manual VSP workflow was developed using Geomagics FreeformPlus (Version 2017) software. The workflow was used to simulate a FOA in a three-month-old female with UCS. The skull model reconstructed using the workflow had a forehead that was closer in shape to a normal skull and was more symmetrical based on a qualitative assessment. The benefit of the manual workflow is that a surgical team can simulate an operation multiple times virtually without any consequence to the patient. The downsides are that all of the steps are still dictated by subjective decisions made by a surgeon. This guesswork has been attributed to unreliable results and a large variation between surgeons regarding reconstruction outcomes in CVR (Soleman et al., 2015). To reduce this subjectivity, Boolean operations on polygons and 3D model registration were introduced to create a partially automated workflow for a FOA procedure that had a reduced need for surgeon involvement to guide the planning process.

Boolean operations on polygons are very popular methods for designing solid objects. Typically primitive shapes are introduced, and new objects and 3D models can be created by using the three types of Boolean functions: union, difference, and intersection (Masuda, 1993). Boolean operations have been used previously in VSP, particularly for a surgical guide and splint design (Charton et al., 2017; Chen et al., 2016; Lin et al., 2006; Zhan & Chen, 2016). Similar to this study, Wang et al. (2014) used Boolean subtraction to outline the surgical region of interest to create an aesthetically pleasing toe-to-thumb transfer. This is the first study that uses Boolean operations to outline surgical ROIs in virtual cranial vault remodeling. Subtraction, or difference, was used in this study by taking advantage of the fact that a UCS skull and a normal skull that are registered to each other will overlap in areas of less deformity. Intuitively, areas of the UCS skull that are less dysmorphic, and therefore, more normal will line up well with a normal skull reference. On the other hand, in areas like the flattened frontal bone on the UCS skull, the skulls will only overlap in areas surrounding the dysmorphic bone, forming a perimeter around the area of flattening. This perimeter is used to highlight the area that requires surgical advancement automatically. Using this method to automatically derive the FB ROI and register it to the normal skull model resulted in minimal advancement and residual deformity, as seen in low performing models #5 and #8 (Figure 21). However, for iteration #12, the ROI formed by the Boolean operation was manually smoothed and then registered, resulting in far more advancement of the FB and improved skull morphology (Figure 22). This suggests that the workflow would benefit from a smoothing function to avoid the need for human intervention to uphold the goal of automation.

Another advantage of using this method to automatically outline a FB ROI is that information is provided regarding the surface area over which the deformity spans in a UCS skull. One of the pitfalls of using maximum Hausdorff surface distance measurements to quantify deformity is that it does not provide information on the size of the affected area on the abnormal forehead. Combining the deformity index in chapter two with the automatically derived ROIs provides more information regarding skull morphology.

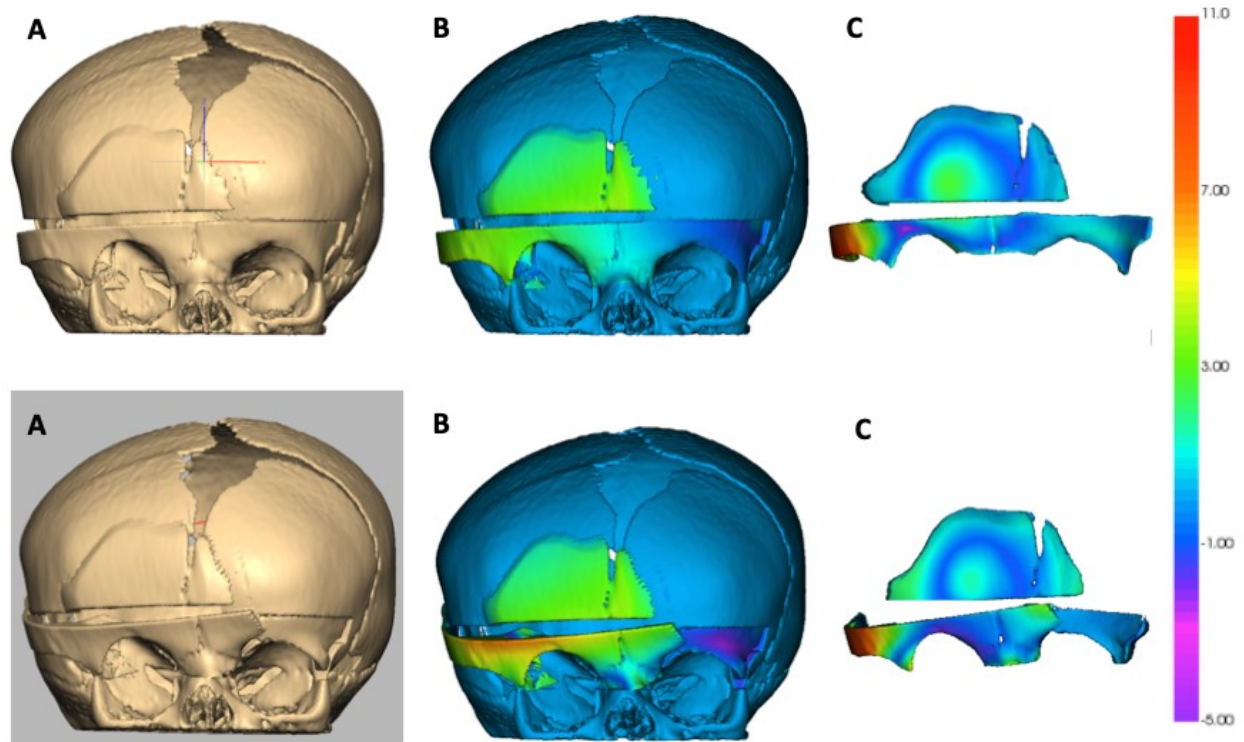


**Figure 4.23** Reconstruction models #5 (top row), and #8 (bottom row) were poor performers among the fifteen automated workflow iterations. The A panels show the reconstruction models, B panels show the comparison to the preoperative skull, and C panels show the comparison to the normal skulls. The FB ROIs when derived and registered fully automatically do not result in a much-improved forehead contour.

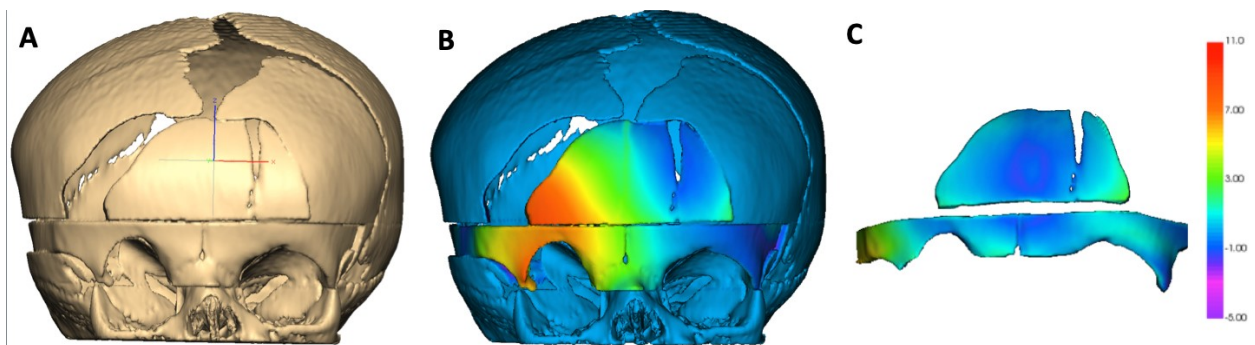


**Figure 4.24** Reconstruction model #12 is displayed (Panel A), along with the comparison between the preoperative skull (Panel B), and the normal skull (Panel C). The edges of the FB region in model #12 are manually smoothed based off the ROI defined by automation. The resultant skull was closer in shape to a normal skull, suggesting the edge smoothing is an important feature to consider in a final algorithm.

The same Boolean subtraction approach was applied to the SOB, but results were less consistent and of limited utility. For example, skull models that had large maximum surface distance values when compared to preoperative models did not necessarily result in a SOB that was close to a normal shape. An example of this would be reconstruction model #8 that had a larger surface distance value compared to model #7 but resulted in a less normal SOB shape

(Figure 23). Conversely, model #7 had one of the smallest advancements but resembled more closely a normal SOB. The superior and inferior rotation was not controlled in the automated workflow when registering the SOB to a normal reference and likely contributed to this inconsistency. As a result, a large distance could refer to a large downward rotation, limited anterior translation, and, therefore not correlate to a clinically improved SOB. Limiting planes of motion for specific surgical maneuvers such as SOB advancement for an FOA would be an important component of an automated workflow. Unlike the FBs, the desired configuration and anticipated advancement for the SOB is more standard. Therefore, using Boolean operations to suggest surgical steps for the SOB may be too simplistic and may not provide the same value of information as for the FB ROI.

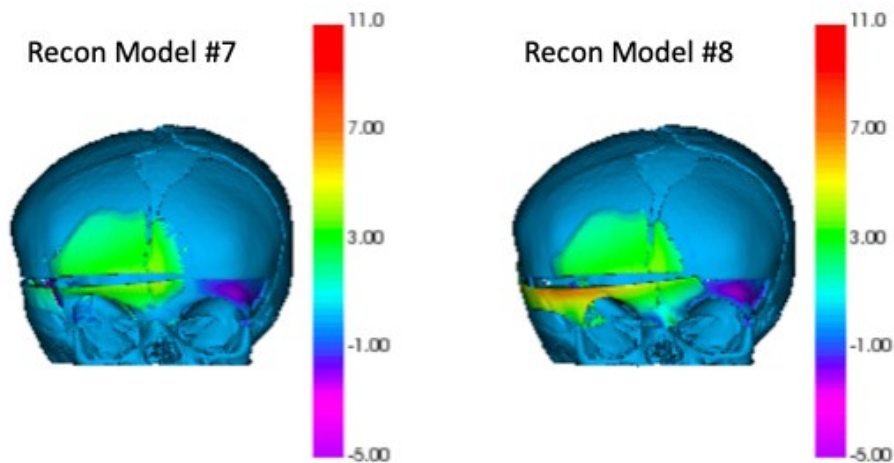


**Figure 4.25** Reconstruction model #7 on the left achieved 4.388 mm of advancement in the virtual FOA compared to reconstruction model #8 on the right (6.763 mm). However, model #7 was closer in shape to a normal model. The degree of downward rotation of the right SOB in model #8 might account for this discrepancy.

A CVR workflow for an FOA where the SOB and FB were outlined and repositioned using automatic functions, such as Boolean operations and registration, was achieved in some of the workflow iterations. However, several workflow iterations that resulted in successfully advanced ROIs and improved forehead shape had a combination of manual and automated steps. In iteration #15, for example, the FB ROI was automatically outlined using a Boolean operation. Then, the FB osteotomy was manually designed to incorporate this area but adhered to a triangular configuration that mimics how frontal bones are currently mobilized at the study institution. The result was a reconstruction model that had good advancement of the frontal

bones and had a mean surface distance value that was reasonably close to a normal skull (0.330 mm) (Figure 24). The pieces of bone graft near the apex of reconstruction model #15 likely contributed to a higher than expected average surface distance value. This is in contrast to model #12, for example, where the reconstruction model is close in shape to a normal skull, but suggests a less conventional osteotomy pattern for the frontal bone. Critics may point out that having more osteotomies at the forehead and not hidden at the apex like in iteration #15 may have a higher risk of contour abnormality and bone resorption in an aesthetically critical area. The benefits of a procedure like the one described for iteration #15 are that the surgeon has additional control over the design of the osteotomy but still has automated suggestions on where to position the FB piece, including where to harvest the bone graft. This highlights the important concept that automated surgical planning can successfully reduce the subjectivity of surgical decision-making. However, clinician input is still crucial to refine a plan and ensure its feasibility. In that sense, computer automation can be viewed as a helpful adjunct to traditional surgeon based planning. Using automation to reduce the guesswork in surgical planning in conjunction with human input may increase the uptake of new technology, especially in initial phases. Even in highly sophisticated computation models, there are steps that require surgeon involvement (Porras et al., 2018).

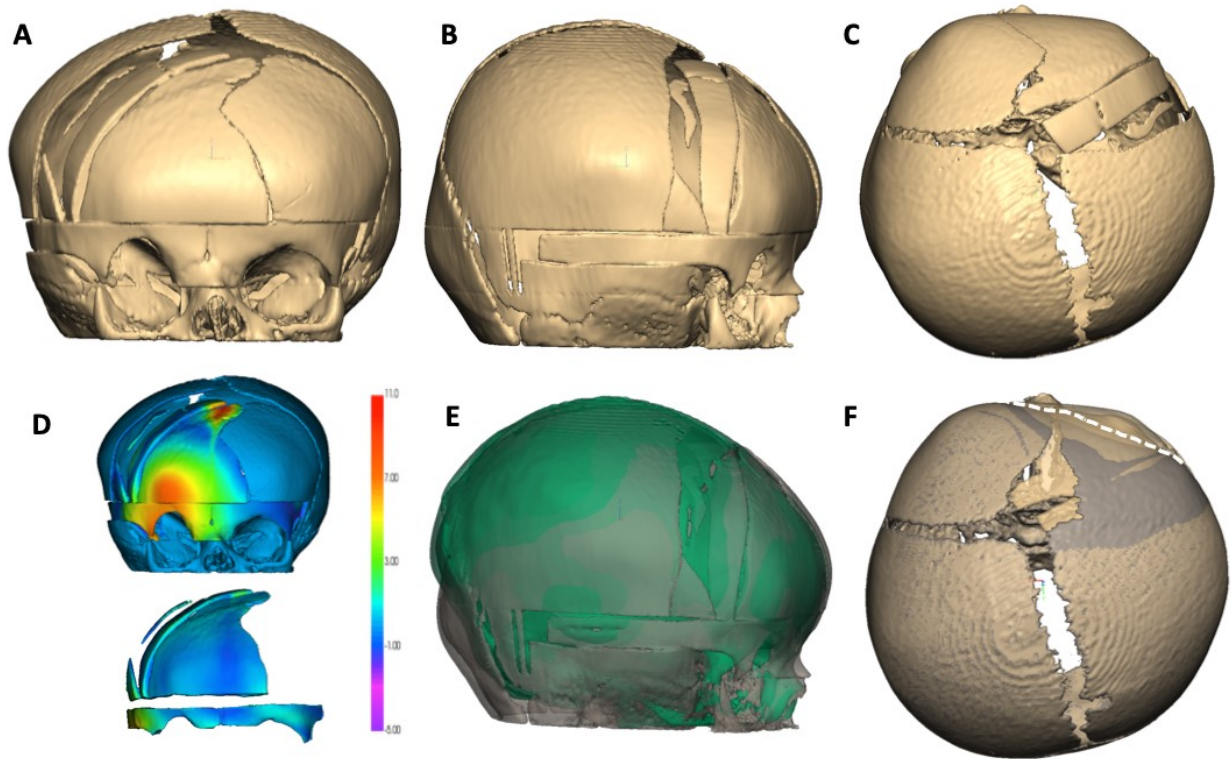


**Figure 4.26** Panel A – A view reconstruction model for iteration #15. Panel B – right lateral view of reconstruction model #15. Panel C – Bird’s eye view of reconstruction model #15. Panel D – Comparison of reconstruction model to preoperative UCS model (top), and the reconstruction model ROIs to the normal skull ROIs (bottom). Panel E – comparison of reconstruction model (grey translucent) to normal skull (green). Panel F – comparison of reconstruction model (beige) to preoperative model (grey). The contour of the preoperative UCS forehead is outlined with the dotted white line.

The presented workflows can be carried out using fundamental computing functions that are widely available in many software programs. In addition, these functions are easily automated, and the demonstration of their potential in surgical planning is optimistic for the development of a fully automated planning algorithm. Although there are downsides to a simplified approach to automating surgical planning, the information provided may still be valuable for surgical planning. Automatically outlining ROIs has the potential to reduce the guesswork associated with CVR. In addition, the advantage of 3D visual aids for preoperative planning has been long recognized (Vannier, 1983). Van Nunen et al. (2014) found a benefit from printing stereolithographic models when planning an FOA. While this simple aid did not reduce surgical times or decrease the blood transfusion rate, surgical trainees, and patients’ families benefitted from the models. Using the proposed workflow, surgeons could run through multiple operative options virtually, quickly, and in a cost-effective manner using in-house

resources. In addition, visual aids have been shown to benefit patient families when considering surgery (Care et al., 2018). Virtual surgical plans could augment the consultation experience with patients' families regarding CVR operations, at a low cost and time expense to surgical teams.

#### **4.6.1 Limitations**

There are limitations of the presented workflows. Firstly, proprietary software was used and may be a deterrent to their widespread use. However, Boolean operations are common and available in open-source software programs, such as 3D Slicer (Version 4.10.2). It is possible that the concept can be applied in programs that are more accessible.

In addition, there is no biomechanical information regarding the properties of infant bone in either the manual or automated workflow. The challenge of introducing bone bending in automated CVR algorithms has only recently been introduced (Porras et al., 2018). While a simplified approach to automated surgical planning may be more accessible to clinicians, the downside could be a less realistic approach. In the proposed workflow, the degree to which bones can bend before fracturing is based on visual judgment and surgeon experience.

In addition, the automated workflow relies on a degree of bony overlap between the UCS and the reference skull model. It is possible to achieve this if a large and varied library of normal skulls is available at an institution, and the method of using an age and sex-matched skull for this comparison has been employed with success (Chim et al., 2014; Dangi et al., 2017; Soleman et al., 2015). However, some institutions may not have such a repository of CT information available, or some cases may be difficult to match for other reasons. In these circumstances, the presented workflow may be of limited use. One method to improve the registration accuracy in these scenarios would be to use statistical shape modeling as opposed to matched skulls (Mendoza et al., 2014; Saber et al., 2012).

#### **4.6.2 Future Work**

This study presents a conceptual basis and pilot data for an alternative method to develop automated surgical workflow algorithms for CVR applied to UCS. Future work with this data would include developing an algorithm using the described Boolean and registration functions, as well as adding in features such as bone bending and edge smoothing.

In addition, algorithm derived surgical plans have not been compared to expert surgeon plans. The goal of future studies would be to compare a UCS reconstruction model as planned by an experienced pediatric craniofacial surgeon using a manual workflow to a computer-derived reconstruction model. Variables such as planning duration and reconstruction success, as measured in this study, would be measured.

#### **4.7 Conclusion**

An in-house manual and partially automated workflow for FOA procedures was developed and piloted using a case of UCS. This is the first study to use Boolean operations on polygons and registration to suggest surgical steps for CVR. The automated workflow was successful in reducing the subjectivity of surgical decision making by highlighting key regions of interest in an infant skull and suggesting possible reconstruction models. A simple approach to automated surgical planning has limitations but may result in more clinician uptake than more sophisticated methods. Automation allows for the amount of trial and error in VSP to be decreased, which would likely result in a reduction in surgical planning time. These virtual tools may benefit surgical teams in the pre-planning environment.

## Chapter 5: Conclusion

The three studies presented in this thesis document are unified by their application toward the field of surgical design and simulation, and their contribution toward virtual surgical planning, and their dedication toward a complex craniofacial condition. The general themes of “usability” and “accessibility” are maintained throughout. In a time when technological improvements in surgical design and technique are ample and exciting, it is important to maintain a sense of the advantages and disadvantages of using advanced technologies in the surgical setting. Developing techniques that are accessible to surgeons and people naïve to computer sciences may help these advantages and disadvantages remain the focus of further innovation and development.

The first study was generated out of a need to objectively measure cranial vault morphology, both as it compares to normal morphology, and as it compares to a preoperative shape. Previous studies tackling the same problem were difficult to replicate without a background in computing sciences, without a multi-disciplinary team, and without specialized software. In addition, previous studies were using methods such as manual measurements that are almost too primitive, and therefore time-consuming to be routinely applied. The deformity index was developed out of the desire for a practical measurement workflow that provided information about global head shape. The purpose of this was to have a method to compare surgeon-derived virtual surgical planning to partially automatic surgical planning in the last study.

From there, the desire to maintain clinical relevance as the focus of innovation in surgical design and simulation lead to the second study regarding perceptions of deformity in unicoronal synostosis. The ability to create a perfect reconstruction virtually may not always translate into the clinical setting when soft tissue, patient growth, and other surgical factors are involved. Therefore, determining an objective goal for surgical correction that corresponds to what is noticeable to the public may help set realistic parameters and expectations.

The motivating concept behind this thesis work is the desire for an automated computer algorithm that could take a UCS skull, compare it to a normal reference skull, and from those two inputs, generate an optimal surgical plan with steps for a successful reconstruction. While VSP takes the trial and error approach to CVR out of the operating room and into a safe virtual

environment, the degree of guesswork in surgical decision-making is largely maintained. An automated computer algorithm that can suggest osteotomy and fixation patterns based on objectively defined parameters may reduce this subjectivity. The third study presented a novel approach to laying the groundwork for such an algorithm. This groundwork was using Boolean operations and registration functions to replace components of surgeon input in the planning process, and to create a workflow that had the potential to be automated. This study presents promising results from one case where these steps were used to generate a surgical plan that resulted in numerous iterations with varying reconstruction outcomes. This again demonstrates a simplified approach that is accessible and user-friendly, taking advantage of simple geometric principles.

Future work will involve refining parameters of the partially automated workflow and including features such as bone bending so that reconstruction models are optimal and more realistic. The workflow will be applied to more cases so that all potential pitfalls are recognized and factored into the development of an algorithm. Once all parameters are in place, collaboration with computer scientists will continue toward the development of an automatic computer algorithm that suggests optimal surgical steps for cranial vault remodeling. Results from the algorithm can be compared to results using traditional techniques to illicit the advantages and disadvantages of this technology. In addition, gathering feedback from surgeons regarding the feasibility of automatically derived reconstruction models will help outline the optimal balance of surgeon and computer input in the surgical planning process.

In summary, all three studies share the common goal of improving surgical planning for cranial vault remodeling, specifically in patients with unicoronal synostosis. They present the groundwork for continued studies in this field and for the development of computing science tools that may be advantageous in surgical planning.

## Thesis References

- Alberta Health, Analytics and Performance Reporting Branch.* (2018). [Interactive Health Data Application: Age Specific Fertility Rates]. Government of Alberta.  
[http://www.ahw.gov.ab.ca/IHDA\\_Retrieval/selectSubCategoryParameters.do#](http://www.ahw.gov.ab.ca/IHDA_Retrieval/selectSubCategoryParameters.do#)
- Alford, J., Derderian, C. A., & Smartt, J. M. (2018). Surgical Treatment of Nonsyndromic Unicoronal Craniosynostosis: *Journal of Craniofacial Surgery*, 29(5), 1199–1207.  
<https://doi.org/10.1097/SCS.00000000000004509>
- Barbero-García, I., Lerma, J. L., Marqués-Mateu, Á., & Miranda, P. (2017). Low-Cost Smartphone-Based Photogrammetry for the Analysis of Cranial Deformation in Infants. *World Neurosurgery*, 102, 545–554. <https://doi.org/10.1016/j.wneu.2017.03.015>
- Beckett, J. S., Persing, J. A., & Steinbacher, D. M. (2013). Bilateral Orbital Dysmorphology in Unicoronal Synostosis: *Plastic and Reconstructive Surgery*, 131(1), 125–130.  
<https://doi.org/10.1097/PRS.0b013e3182729ed7>
- Burge, J., Saber, N. R., Looi, T., French, B., Usmani, Z., Anooshiravani, N., Kim, P., Forrest, C., & Phillips, J. (2011). Application of CAD/CAM Prefabricated Age-Matched Templates in Cranio-Orbital Remodeling in Craniosynostosis: *Journal of Craniofacial Surgery*, 22(5), 1810–1813. <https://doi.org/10.1097/SCS.0b013e31822e8045>
- Burton, H. E., Peel, S., & Eggbeer, D. (2018). Reporting fidelity in the literature for computer aided design and additive manufacture of implants and guides. *Additive Manufacturing*, 23, 362–373. <https://doi.org/10.1016/j.addma.2018.08.027>
- Campbell, C., & Derderian, C. (2014). Craniosynostosis. In *Essentials of Plastic Surgery* (2nd edition, p. 237). Taylor & Francis Group.

- Care, H., Dalton, L., & Johnson, D. (2018). The Value of a Photobook in Informing Families About the Cosmetic Results of Surgery in Craniosynostosis: *Journal of Craniofacial Surgery*, 29(1), 88–91. <https://doi.org/10.1097/SCS.00000000000004194>
- Charton, J., Laurentjoye, M., & Kim, Y. (2017). 3D Boolean operations in virtual surgical planning. *International Journal of Computer Assisted Radiology and Surgery*, 12(10), 1697–1709. <https://doi.org/10.1007/s11548-017-1637-y>
- Chen, X., Li, X., Xu, L., Sun, Y., Politis, C., & Egger, J. (2016). Development of a computer-aided design software for dental splint in orthognathic surgery. *Scientific Reports*, 6(1). <https://doi.org/10.1038/srep38867>
- Chim, H., Wetjen, N., & Mardini, S. (2014). Virtual Surgical Planning in Craniofacial Surgery. *Seminars in Plastic Surgery*, 28(03), 150–158. <https://doi.org/10.1055/s-0034-1384811>
- Choi, K. Y. (2015). Analysis of Facial Asymmetry. *Archives of Craniofacial Surgery*, 16(1), 1–10. <https://doi.org/10.7181/acfs.2015.16.1.1>
- Chu, E. A., Farrag, T. Y., Ishii, L. E., & Byrne, P. J. (2011). Threshold of Visual Perception of Facial Asymmetry in a Facial Paralysis Model. *Archives of Facial Plastic Surgery*, 13(1), 14–19. <https://doi.org/10.1001/archfacial.2010.101>
- Cochrane, S. (1999). A comparison of the perception of facial profile by the general public and 3 groups of clinicians. *The International Journal of Adult Orthodontics and Orthognathic Surgery*, 14(4), 291–295.
- Collett, B. R., Gray, K. E., Kapp-Simon, K. A., Birgfeld, C., Cunningham, M., Rudo-Stern, J., Ung, D., Buono, L., & Speltz, M. L. (2013). Laypersons' Ratings of Appearance in Children With and Without Single-Suture Craniosynostosis: *Journal of Craniofacial Surgery*, 24(4), 1331–1335. <https://doi.org/10.1097/SCS.0b013e3182997885>

- Dangi, S., Shah, H., Porras, A. R., Paniagua, B., Linte, C. A., Linguraru, M., & Enquobahrie, A. (2017). Robust head CT image registration pipeline for craniosynostosis skull correction surgery. *Healthcare Technology Letters*, 4(5), 174–178.  
<https://doi.org/10.1049/htl.2017.0067>
- de Jong, G., Tolhuisen, M., Meulstee, J., van der Heijden, F., van Lindert, E., Borstlap, W., Maal, T., & Delye, H. (2017). Radiation-free 3D head shape and volume evaluation after endoscopically assisted strip craniectomy followed by helmet therapy for trigonocephaly. *Journal of Cranio-Maxillofacial Surgery*, 45(5), 661–671.  
<https://doi.org/10.1016/j.jcms.2017.02.007>
- Delgado-Rodriguez, M. (2004). Bias. *Journal of Epidemiology & Community Health*, 58(8), 635–641. <https://doi.org/10.1136/jech.2003.008466>
- Delye, H., Clijmans, T., Mommaerts, M. Y., Sloten, J. V., & Goffin, J. (2015). Creating a normative database of age-specific 3D geometrical data, bone density, and bone thickness of the developing skull: A pilot study. *Journal of Neurosurgery: Pediatrics*, 687–702.  
<https://doi.org/10.3171/2015.4.PEDS1493>
- Fearon, J. (2014). Evidence-Based Medicine: Craniosynostosis. *Plastic and Reconstructive Surgery*, 133(5), 1261–1275.
- Fedorov, A., Beichel, R., Kalpathy-Cramer, J., Finet, J., Fillion-Robin, J.-C., Pujol, S., Bauer, C., Jennings, D., Fennessy, F., Sonka, M., Buatti, J., Aylward, S., Miller, J. V., Pieper, S., & Kikinis, R. (2012). 3D Slicer as an image computing platform for the Quantitative Imaging Network. *Magnetic Resonance Imaging*, 30(9), 1323–1341.  
<https://doi.org/10.1016/j.mri.2012.05.001>

- Fisher, M., Medina, M., Bojovic, B., Ahn, E., & Dorafshar, A. (2016). Indications for Computer-Aided Design and Manufacturing in Congenital Craniofacial Reconstruction. *Craniofacial Trauma and Reconstruction*, *09*(03), 235–241. <https://doi.org/10.1055/s-0036-1584391>
- Gerstle, T. L., Ibrahim, A. M. S., Kim, P. S., Lee, B. T., & Lin, S. J. (2014). A Plastic Surgery Application in Evolution: Three-Dimensional Printing. *Plastic and Reconstructive Surgery*, *133*(2), 446–451. <https://doi.org/10.1097/01.prs.0000436844.92623.d3>
- Hilling, D. E., & Vaandrager, J. M. (2006). Long-term aesthetic results of frontoorbital correction for frontal plagiocephaly. *J. Neurosurg*, *105*, 21–25.
- Hinkle, D. E., Wiersma, W., & Jurs, S. G. (2003). *Applied Statistics for the Behavioral Sciences* (5th ed.). Houghton Mifflin.
- Hohman, M. H., Kim, S. W., Heller, E. S., Frigerio, A., Heaton, J. T., & Hadlock, T. A. (2014). Determining the threshold for asymmetry detection in facial expressions: Detection of Facial Asymmetry. *The Laryngoscope*, *124*(4), 860–865. <https://doi.org/10.1002/lary.24331>
- Huttenlocher, D., Klandermann, G., & Rucklidge, W. (1993). Comparing Images using the Hausdorff Distance. *IEEE Transactions on Patterns and Machine Intelligence*, *15*(9), 850–863.
- Jans, G., Sloten, J. V., Gobin, R., Van der Perre, G., Audekercke, R. V., & Mommaeits, M. (1999). Computer-Aided Craniofacial Surgical Planning Implemented in CAD Software. *Computer Aided Surgery*, *4*(3), 117–128. <https://doi.org/10.3109/10929089909148167>
- Khechoyan, D. Y., Saber, N. R., Burge, J., Fattah, A., Drake, J., Forrest, C. R., & Phillips, J. H. (2014). Surgical outcomes in craniosynostosis reconstruction: The use of prefabricated

- templates in cranial vault remodelling. *Journal of Plastic, Reconstructive & Aesthetic Surgery*, 67(1), 9–16. <https://doi.org/10.1016/j.bjps.2013.09.009>
- Kim, S. W., Heller, E. S., Hohman, M. H., Hadlock, T. A., & Heaton, J. T. (2013). Detection and Perceptual Impact of Side-to-Side Facial Movement Asymmetry. *JAMA Facial Plastic Surgery*, 15(6), 411–416. <https://doi.org/10.1001/jamafacial.2013.1227>
- Lee, H. Q., Hutson, J. M., Wray, A. C., Lo, P. A., Chong, D. K., Holmes, A. D., & Greensmith, A. L. (2012). Analysis of Morbidity and Mortality in Surgical Management of Craniosynostosis: *Journal of Craniofacial Surgery*, 23(5), 1256–1261. <https://doi.org/10.1097/SCS.0b013e31824e26d6>
- Lin, Y., Zhang, S., Chen, X., & Wang, C. (2006). A novel method in the design and fabrication of dental splints based on 3D simulation and rapid prototyping technology. *The International Journal of Advanced Manufacturing Technology*, 28(9–10), 919–922. <https://doi.org/10.1007/s00170-004-2197-1>
- Liu, M. T., Khechoyan, D. Y., Susarla, S. M., Skladman, R., Birgfeld, C. B., Gruss, J. S., Lee, A., Ellenbogen, R. G., Pet, M. A., & Hopper, R. A. (2019). Evolution of Bandeau Shape, Orbital Morphology, and Craniofacial Twist after Fronto-Orbital Advancement for Isolated Unilateral Coronal Synostosis: A Case-Control Study of 2-Year Outcomes. *Plastic and Reconstructive Surgery*, 143(6), 1703–1711. <https://doi.org/10.1097/PRS.0000000000005639>
- LoPresti, M., Daniels, B., Buchanan, E. P., Monson, L., & Lam, S. (2017). Virtual surgical planning and 3D printing in repeat calvarial vault reconstruction for craniosynostosis: Technical note. *Journal of Neurosurgery: Pediatrics*, 490–494. <https://doi.org/10.3171/2016.10.PEDS16301>

- Marcus, J. R., Domeshek, L. F., Loyd, A. M., Schoenleber, J. M., Das, R. R., Nightingale, R. W., & Mukundan, S. (2009). Use of a Three-Dimensional, Normative Database of Pediatric Craniofacial Morphology for Modern Anthropometric Analysis: *Plastic and Reconstructive Surgery*, *124*(6), 2076–2084.  
<https://doi.org/10.1097/PRS.0b013e3181bf7e1b>
- Mardini, S., Alsubaie, S., Cayci, C., Chim, H., & Wetjen, N. (2014). Three-dimensional preoperative virtual planning and template use for surgical correction of craniosynostosis. *Journal of Plastic, Reconstructive & Aesthetic Surgery*, *67*(3), 336–343.  
<https://doi.org/10.1016/j.bjps.2013.11.004>
- Martelli, N., Serrano, C., van den Brink, H., Pineau, J., Prognon, P., Borget, I., & El Batti, S. (2016). Advantages and disadvantages of 3-dimensional printing in surgery: A systematic review. *Surgery*, *159*(6), 1485–1500. <https://doi.org/10.1016/j.surg.2015.12.017>
- Masserano, B., Woo, A. S., Skolnick, G. B., Naidoo, S. D., Proctor, M. R., Smyth, M. D., & Patel, K. B. (2018). The Temporal Region in Unilateral Coronal Craniosynostosis: Fronto-orbital Advancement Versus Endoscopy-Assisted Strip Craniectomy. *The Cleft Palate-Craniofacial Journal*, *55*(3), 423–429.  
<https://doi.org/10.1177/1055665617739000>
- Masuda, H. (1993). Topological operators and Boolean operations for complex-based nonmanifold geometric models. *Computer-Aided Design*, *25*(2), 119–129.  
[https://doi.org/10.1016/0010-4485\(93\)90097-8](https://doi.org/10.1016/0010-4485(93)90097-8)
- Mazzaferro, D. M., Wes, A. M., Naran, S., Bartlett, S. P., & Taylor, J. A. (2017). A Volumetric and Craniometric Analysis of Cranial Base Differences in Unicoronal Craniosynostosis:

- Journal of Craniofacial Surgery*, 28(7), 1725–1729.  
<https://doi.org/10.1097/SCS.0000000000003865>
- McKay, D. R., Davidge, K. M., Williams, S. K., Ellis, L. A., Chong, D. K., Teixeira, R. P., Greensmith, A. L., & Holmes, A. D. (2010). Measuring Cranial Vault Volume With Three-Dimensional Photography: A Method of Measurement Comparable to the Gold Standard. *Journal of Craniofacial Surgery*, 21(5), 1419–1422.  
<https://doi.org/10.1097/SCS.0b013e3181e3181e>
- Mendoza, C. S., Safdar, N., Okada, K., Myers, E., Rogers, G. F., & Linguraru, M. G. (2014). Personalized assessment of craniosynostosis via statistical shape modeling. *Medical Image Analysis*, 18(4), 635–646. <https://doi.org/10.1016/j.media.2014.02.008>
- Mommaerts, M. Y., Jans, G., Sloten, J. V., Staels, P. F. J., Van der Perre, G., & Gobin, R. (2001). On the Assets of CAD Planning for Craniosynostosis Surgery: *Journal of Craniofacial Surgery*, 12(6), 547–554. <https://doi.org/10.1097/00001665-200111000-00008>
- Msallem, B., Beiglboeck, F., Honigmann, P., Jaquiéry, C., & Thieringer, F. (2017). Craniofacial Reconstruction by a Cost-Efficient Template-Based Process Using 3D Printing: *Plastic and Reconstructive Surgery - Global Open*, 5(11), e1582.  
<https://doi.org/10.1097/GOX.0000000000001582>
- Pinter, C., Lasso, A., Wang, A., Jaffray, D., & Fichtinger, G. (2012). SlicerRT: Radiation therapy research toolkit for 3D Slicer: SlicerRT: Radiation therapy research toolkit for 3D Slicer. *Medical Physics*, 39(10), 6332–6338. <https://doi.org/10.1118/1.4754659>
- Porras, A. R., Paniagua, B., Enquobahrie, A., Ensel, S., Shah, H., Keating, R., Rogers, G. F., & Linguraru, M. G. (2017). Locally Affine Diffeomorphic Surface Registration for Planning of Metopic Craniosynostosis Surgery. In M. Descoteaux, L. Maier-Hein, A.

- Franz, P. Jannin, D. L. Collins, & S. Duchesne (Eds.), *Medical Image Computing and Computer-Assisted Intervention – MICCAI 2017* (Vol. 10434, pp. 479–487). Springer International Publishing. [https://doi.org/10.1007/978-3-319-66185-8\\_54](https://doi.org/10.1007/978-3-319-66185-8_54)
- Porras, A. R., Paniagua, B., Ensel, S., Keating, R., Rogers, G. F., Enquobahrie, A., & Linguraru, M. G. (2018). Locally Affine Diffeomorphic Surface Registration and Its Application to Surgical Planning of Fronto-Orbital Advancement. *IEEE Transactions on Medical Imaging*, 37(7), 1690–1700. <https://doi.org/10.1109/TMI.2018.2816402>
- Porras, A. R., Tu, L., Tsering, D., Mantilla, E., Oh, A., Enquobahrie, A., Keating, R., Rogers, G. F., & Linguraru, M. G. (2019a). Quantification of Head Shape from Three-Dimensional Photography for Presurgical and Postsurgical Evaluation of Craniosynostosis: *Plastic and Reconstructive Surgery*, 144(6), 1051e–1060e. <https://doi.org/10.1097/PRS.00000000000006260>
- Porras, A. R., Tu, L., Tsering, D., Mantilla, E., Oh, A., Enquobahrie, A., Keating, R., Rogers, G. F., & Linguraru, M. G. (2019b). Quantification of Head Shape from Three-Dimensional Photography for Presurgical and Postsurgical Evaluation of Craniosynostosis: *Plastic and Reconstructive Surgery*, 144(6), 1051e–1060e. <https://doi.org/10.1097/PRS.00000000000006260>
- Porras, A. R., Zukic, D., Equobahrie, A., Rogers, G. F., & Linguraru, M. G. (2016a). Personalized Optimal Planning for the Surgical Correction of Metopic Craniosynostosis. In R. Shekhar, S. Wesarg, M. Á. González Ballester, K. Drechsler, Y. Sato, M. Erdt, M. G. Linguraru, & C. Oyarzun Laura (Eds.), *Clinical Image-Based Procedures. Translational Research in Medical Imaging* (Vol. 9958, pp. 60–67). Springer International Publishing. [https://doi.org/10.1007/978-3-319-46472-5\\_8](https://doi.org/10.1007/978-3-319-46472-5_8)

- Porras, A. R., Zukic, D., Equobahrie, A., Rogers, G. F., & Linguraru, M. G. (2016b). Personalized Optimal Planning for the Surgical Correction of Metopic Craniosynostosis. In R. Shekhar, S. Wesarg, M. Á. González Ballester, K. Drechsler, Y. Sato, M. Erdt, M. G. Linguraru, & C. Oyarzun Laura (Eds.), *Clinical Image-Based Procedures. Translational Research in Medical Imaging* (Vol. 9958, pp. 60–67). Springer International Publishing. [https://doi.org/10.1007/978-3-319-46472-5\\_8](https://doi.org/10.1007/978-3-319-46472-5_8)
- Queiros, C., Joly, A., Paré, A., Listrat, A., Travers, N., Goga, D., & Laure, B. (2017). Use of cutting guides during craniosynostosis sequelae surgery: A comparative study between computer-assisted planning and post-operative results. *Journal of Cranio-Maxillofacial Surgery*, 45(7), 1062–1068. <https://doi.org/10.1016/j.jcms.2017.03.011>
- Robertson, E., Louie, G., Kwan, P., Boulanger, P., & Aalto, D. (2020). Skeletal deformity in patients with unilateral coronal craniosynostosis—Perceptions of the general public. *Journal of Craniomaxillofacial Trauma and Reconstruction*.
- Saber, N. R., Phillips, J., Looi, T., Usmani, Z., Burge, J., Drake, J., & Kim, P. C. W. (2012). Generation of normative pediatric skull models for use in cranial vault remodeling procedures. *Child's Nervous System*, 28(3), 405–410. <https://doi.org/10.1007/s00381-011-1630-7>
- Safran, T., Viesel-Mathieu, A., Beland, B., Azzi, A. J., Galli, R., & Gilardino, M. (2018). The State of Technology in Craniosynostosis: *Journal of Craniofacial Surgery*, 29(4), 904–907. <https://doi.org/10.1097/SCS.0000000000004399>
- Salazar-Gamarra, R., Seelaus, R., da Silva, J. V. L., da Silva, A. M., & Dib, L. L. (2016). Monoscopic photogrammetry to obtain 3D models by a mobile device: A method for

- making facial prostheses. *Journal of Otolaryngology - Head & Neck Surgery*, 45(1).  
<https://doi.org/10.1186/s40463-016-0145-3>
- Selber, J. C., Brooks, C., Kurichi, J. E., Temmen, T., Sonnad, S. S., & Whitaker, L. A. (2008). Long-Term Results following Fronto-Orbital Reconstruction in Nonsyndromic Uniconoral Synostosis: *Plastic and Reconstructive Surgery*, 121(5), 251e–260e.  
<https://doi.org/10.1097/PRS.0b013e31816a9f88>
- Seruya, M., Borsuk, D. E., Khalifian, S., Carson, B. S., Dalesio, N. M., & Dorafshar, A. H. (2013). Computer-Aided Design and Manufacturing in Craniosynostosis Surgery: *Journal of Craniofacial Surgery*, 24(4), 1100–1105.  
<https://doi.org/10.1097/SCS.0b013e31828b7021>
- Snyder, H., & Pope, A. W. (2010). Psychosocial Adjustment in Children and Adolescents with a Craniofacial Anomaly: Diagnosis-Specific Patterns. *The Cleft Palate-Craniofacial Journal*, 47(3), 264–272. <https://doi.org/10.1597/08-227.1>
- Soleman, J., Thieringer, F., Beinemann, J., Kunz, C., & Guzman, R. (2015). Computer-assisted virtual planning and surgical template fabrication for frontoorbital advancement. *Neurosurgical Focus*, 38, 1–5. <https://doi.org/10.3171/2015.3.FOCUS14852>
- Tahiri, Y., Bartlett, S. P., & Gilardino, M. S. (2017). Evidence-Based Medicine: Nonsyndromic Craniosynostosis. *Plastic and Reconstructive Surgery*, 140(1), 177e–191e.  
<https://doi.org/10.1097/PRS.0000000000003473>
- Taylor, J. A., Paliga, J. T., Wes, A. M., Tahiri, Y., Goldstein, J. A., Whitaker, L. A., & Bartlett, S. P. (2015). A Critical Evaluation of Long-Term Aesthetic Outcomes of Fronto-Orbital Advancement and Cranial Vault Remodeling in Nonsyndromic Uniconoral

Craniosynostosis: *Plastic and Reconstructive Surgery*, 135(1), 220–231.

<https://doi.org/10.1097/PRS.0000000000000829>

Tu, L., Rogers, G. F., Linguraru, M. G., Porras, A. R., Oh, A., Lepore, N., Buck, G. C., Tsering, D., Enquobahrie, A., & Keating, R. (2019). Quantitative evaluation of local head malformations from 3 dimensional photography: Application to craniosynostosis. In H. K. Hahn & K. Mori (Eds.), *Medical Imaging 2019: Computer-Aided Diagnosis* (p. 113). SPIE. <https://doi.org/10.1117/12.2512272>

van Nunen, D. P. F., Janssen, L. E., Stubenitsky, B. M., Han, K. S., & Muradin, M. S. M. (2014). Stereolithographic skull models in the surgical planning of fronto-supraorbital bar advancement for non-syndromic trigonocephaly. *Journal of Cranio-Maxillofacial Surgery*, 42(6), 959–965. <https://doi.org/10.1016/j.jcms.2014.01.017>

Vannier, M. W. (1983). THREE DIMENSIONAL COMPUTER GRAPHICS FOR CRANIOFACIAL SURGICAL PLANNING AND EVALUATION. *Computer Graphics*, 17(3), 11.

Vargo, JK, Gladwin, M, & Ngan, P. (2003). Association between ratings of facial attractiveness and patients' motivation for orthognathic surgery. *Orthod Craniofacial Res*, 6, 63–71.

Wang, L., Tian, G., Wang, M., & Yang, G. (2014). Analysis of the Morphologic Differences of the Second Toe and Digits of the Hand, and Evaluation of Potential Surgical Intervention to Minimize the Differences Using Computer-Aided Design Technology: *Plastic and Reconstructive Surgery*, 134(6), 902e–912e.

<https://doi.org/10.1097/PRS.0000000000000761>

Wes, A. M., Mazzaferro, D., Naran, S., Bartlett, S. P., & Taylor, J. A. (2017). Nasal Root Deviation in Unicoronal Craniosynostosis: A Craniometric Analysis of Early and Late

- Postoperative Outcomes. *Journal of Craniofacial Surgery*, 28(5), 1220–1223.  
<https://doi.org/10.1097/SCS.0000000000003665>
- Wes, A. M., Naran, S., Sun, J., Mazzaferro, D., Xu, W., Nguyen, P., Whitaker, L. A., Bartlett, S. P., & Taylor, J. A. (2017). The Whitaker Classification of Craniosynostosis Outcomes: An Assessment of Interrater Reliability. *Plastic and Reconstructive Surgery*, 140(4), 579e–586e. <https://doi.org/10.1097/PRS.0000000000003688>
- Whitaker, L., Pashayan, H., & Reichman, J. (1981). A proposed new classification of craniofacial anomalies. *Cleft Palate Journal*, 18, 161–176.
- Wilbrand, J.-F., Szczukowski, A., Blecher, J.-C., Pons-Kuehnemann, J., Christophis, P., Howaldt, H.-P., & Schaaf, H. (2012). Objectification of cranial vault correction for craniosynostosis by three-dimensional photography. *Journal of Cranio-Maxillofacial Surgery*, 40(8), 726–730. <https://doi.org/10.1016/j.jcms.2012.01.007>
- Wood, B. C., Mendoza, C. S., Oh, A. K., Myers, E., Safdar, N., Linguraru, M. G., & Rogers, G. F. (2016). What’s in a Name? Accurately Diagnosing Metopic Craniosynostosis Using a Computational Approach: *Plastic and Reconstructive Surgery*, 137(1), 205–213.  
<https://doi.org/10.1097/PRS.0000000000001938>
- Xia, J. J., Phillips, C. V., Gateno, J., Teichgraber, J. F., Christensen, A. M., Gliddon, M. J., Lemoine, J. J., & Liebschner, M. A. K. (2006). Cost-Effectiveness Analysis for Computer-Aided Surgical Simulation in Complex Cranio-Maxillofacial Surgery. *Journal of Oral and Maxillofacial Surgery*, 64(12), 1780–1784.  
<https://doi.org/10.1016/j.joms.2005.12.072>
- Xu, W., Gerety, P. A., Li, J., Bartlett, S. P., & Taylor, J. A. (2017). Frontal Sinus Volume and Frontal Bar Position Are Associated in Unicoronal Craniosynostosis: *Plastic and*

*Reconstructive Surgery*, 139(4), 965e–974e.

<https://doi.org/10.1097/PRS.0000000000003180>

Yang, B., Ni, J., & Li, B. (2018). 3D morphological change of skull base and fronto-temporal soft-tissue in the patients with unicoronal craniosynostosis after fronto-orbital advancement. *Child's Nervous System*, 34(5), 947–955. <https://doi.org/10.1007/s00381-018-3721-1>

Yu, J. W., Xu, W., Wink, J. D., Wes, A. M., Bartlett, S. P., & Taylor, J. A. (2020). Strabismus in Unicoronal Craniosynostosis: Effect of Orbital Dymorphology and Fronto-Orbital Advancement and Remodeling. *Plastic and Reconstructive Surgery*, 145(2), 382e–390e. <https://doi.org/10.1097/PRS.00000000000006479>

Zhan, Q., & Chen, X. (2016). Boolean Combinations of Implicit Functions for Model Clipping in Computer-Assisted Surgical Planning. *PLOS ONE*, 11(1), e0145987. <https://doi.org/10.1371/journal.pone.0145987>

Zhao, L., Patel, P. K., & Cohen, M. (2012). Application of Virtual Surgical Planning with Computer Assisted Design and Manufacturing Technology to Cranio-Maxillofacial Surgery. *Archives of Plastic Surgery*, 39(4), 309. <https://doi.org/10.5999/aps.2012.39.4.309>

## List of Tables

### Chapter 1

**Table 1.1** Outline of studies presented in the thesis document.

Chapter 2 – Study #1	<ul style="list-style-type: none"><li>• Development of deformity index workflow</li><li>• Using the novel workflow to quantify deformity in a series of UCS patients</li><li>• Test-retest reliability testing</li><li>• Case example: using workflow to quantify reconstruction success in pre and postoperative patient</li></ul>
Chapter 3 – Study #2	<ul style="list-style-type: none"><li>• Assessing general public’s perceptions of skull deformity</li></ul>
Chapter 4 – Study #3	<ul style="list-style-type: none"><li>• Manual and partially automated virtual workflow development for CVR surgery for UCS</li></ul>

## Chapter 2

**Table 2.1** Age and sex matched participants for the study pairs.

Pair #	Experimental		Control Skull	
	Age	Sex	Age	Sex
1	7	F	7	F
2	3	M	3	M
3	4	F	4	F
4	5	F	5	F
5	3	M	3	M
6	4	F	4	F
7	5	F	5	F
8	3	F	3	F
9	5	F	5	F
10	15	F	14	F
11	6	M	7	F
12	5	F	5	F
13	3	F	3	F
14	5	F	5	F
15	9	F	8	F

**Table 2.2** Results for test-retest reliability assessment.

Pair #	Maximum Hausdorff Surface Distance (mm)	
	Trial #1	Trial #2
1	5.95	5.95
2	6.92	7.26
3	6.62	4.61
4	4.97	3.82
5	7.80	7.81
6	5.85	6.11
7	8.53	8.73
8	5.28	4.85
9	1.99	2.43
10	4.60	4.42
11	4.28	4.75
12	5.34	4.73
13	10.36	10.22
14	2.81	4.12
15	5.32	5.83

### Chapter 3

**Table 3.1** Summary of demographic data for the layperson skull raters.

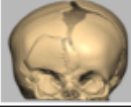
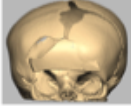
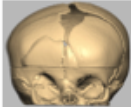
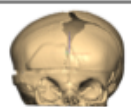
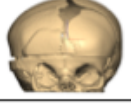
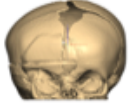
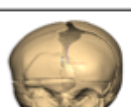
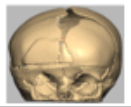
Demographic Characteristic	Layperson Skull Raters	
	<i>Number</i>	<i>Percent</i>
<b>Total</b>	40	100.0
<b>Sex</b>		
<i>Female</i>	21	52.5
<i>Male</i>	19	47.5
<b>Level of Education</b>		
<i>High school</i>	3	7.5
<i>Post Secondary</i>	37	92.5
	<i>Mean ± STD</i>	<i>Range</i>
<b>Age</b>	33.6 ± 12.4	22 - 73

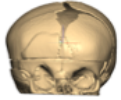
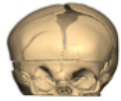
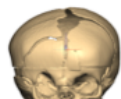
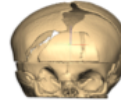
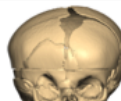
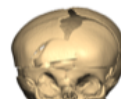
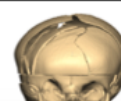
**Table 3.2** Summary of demographic data for the skull cohorts.

<b>Demographic Characteristic</b>	<b>Normal Skulls</b>		<b>UCS Skulls</b>	
	<i>Number</i>	<i>Percent</i>	<i>Number</i>	<i>Percent</i>
<b>Total (/45 skulls)</b>	24	53.3	21	46.7
<b>Sex</b>				
<i>Female</i>	17	70.8	16	76.2
<i>Male</i>	7	29.2	5	23.8
<b>Affected suture</b>				
<i>Right</i>	--	--	17	81.0
<i>Left</i>	--	--	4	19.0
	<i>Mean ± STD</i>	<i>Range</i>	<i>Mean ± STD</i>	<i>Range</i>
<b>Age (months)</b>	7.0 ± 4.3	2 - 16	4.9 ± 3.0	1 - 15

## Chapter 4

**Table 4.1** Summary of the 15 iterations of the partially automated workflow.

Work-flow Iteration #	Key Points	Pros	Cons	Reconstruction Model
1	<ul style="list-style-type: none"> <li>• FB ROI is automatically highlighted by Boolean function</li> <li>• Identified ROI is registered to the control skull</li> </ul>	<ul style="list-style-type: none"> <li>• Fully automated</li> </ul>	<ul style="list-style-type: none"> <li>• Minimal FB advancement achieved</li> <li>• SOB &amp; FB not separated</li> </ul>	
2	<ul style="list-style-type: none"> <li>• FB ROI is automatically highlighted by Boolean</li> <li>• Polygon Select Clay tool used to trace out highlighted area</li> </ul>	<ul style="list-style-type: none"> <li>• Obeyed typical surgical boundaries (i.e. 1 cm above supra-orbital rim)</li> <li>• FB piece advanced further than iteration #1</li> </ul>	<ul style="list-style-type: none"> <li>• Not fully automated</li> <li>• FB ROI manually traced out based on area suggested by Boolean function</li> </ul>	
3	<ul style="list-style-type: none"> <li>• FB ROI and SOB ROI are separated and registered to the control skull individually</li> </ul>	<ul style="list-style-type: none"> <li>• Better simulation of real-life surgical scenario</li> </ul>	<ul style="list-style-type: none"> <li>• Minimal FB and SOB advancement</li> <li>• FB does not abut SOB</li> </ul>	
4	<ul style="list-style-type: none"> <li>• FB ROI and SOB ROI are registered to a control FB and a control SOB, versus the whole control skull</li> </ul>	<ul style="list-style-type: none"> <li>• Reasonable degree of advancement</li> </ul>	<ul style="list-style-type: none"> <li>• UCS SOB rotated out of the horizontal plane</li> <li>• FB does not abut SOB</li> </ul>	
5	<ul style="list-style-type: none"> <li>• Control SOB was refined using the same parameters for the UCS SOB</li> </ul>	<ul style="list-style-type: none"> <li>• More realistic reference</li> </ul>	<ul style="list-style-type: none"> <li>• No difference appreciated</li> </ul>	
6	<ul style="list-style-type: none"> <li>• SOB ROI was separated into 2 components: abnormal and normal</li> <li>• Boolean function used to determine abnormal and normal components</li> </ul>	<ul style="list-style-type: none"> <li>• SOB advanced further</li> </ul>	<ul style="list-style-type: none"> <li>• Boolean function creates large gaps in the SOB</li> <li>• Abnormal SOB component rotates out of plane</li> </ul>	
7	<ul style="list-style-type: none"> <li>• Attempt to improve automatic separation of abnormal and normal SOB components</li> </ul>	<ul style="list-style-type: none"> <li>• Fewer gaps in the SOB ROI</li> <li>• Fully automated</li> </ul>	<ul style="list-style-type: none"> <li>• FB does not abut SOB</li> <li>• FB and SOB pieces are not clean</li> </ul>	
8	<ul style="list-style-type: none"> <li>• Attempt to improve automatic separation of abnormal and normal SOB components into cleaner pieces</li> </ul>	<ul style="list-style-type: none"> <li>• SOB advanced further</li> <li>• Cleaner SOB components</li> </ul>	<ul style="list-style-type: none"> <li>• Had to separate components manually based on Boolean overlap</li> </ul>	

9	<ul style="list-style-type: none"> <li>Added Bend Clay function to SOB</li> </ul>	<ul style="list-style-type: none"> <li>SOB shape is much more similar to normal control</li> </ul>	<ul style="list-style-type: none"> <li>Bend component not automated</li> <li>Separating SOB components not automated</li> </ul>	
10	<ul style="list-style-type: none"> <li>Smooth edges of FB ROI</li> <li>Make FB ROI larger than automatically defined piece</li> </ul>	<ul style="list-style-type: none"> <li>Do not lose bone from Boolean subtraction</li> </ul>	<ul style="list-style-type: none"> <li>Not fully automated</li> <li>Negligible advancement of FB</li> </ul>	
11	<ul style="list-style-type: none"> <li>Remove small spicule of SOB in FB ROI from iteration #10</li> </ul>	<ul style="list-style-type: none"> <li>More realistic anatomical boundaries</li> </ul>	<ul style="list-style-type: none"> <li>No difference appreciated</li> </ul>	
12	<ul style="list-style-type: none"> <li>Register FB ROI to whole control skull versus FB ROI of control</li> <li>FB ROI manually delineated</li> </ul>	<ul style="list-style-type: none"> <li>A lot of movement in FB including rotation</li> </ul>	<ul style="list-style-type: none"> <li>Multiple iterations (66 registrations)</li> <li>Not fully automated</li> </ul>	
13	<ul style="list-style-type: none"> <li>Register FB ROI to whole control skull</li> <li>FB ROI automatically delineated</li> </ul>	<ul style="list-style-type: none"> <li>May simulate real-life scenario better than #12 as bone is lost with osteotomies</li> </ul>	<ul style="list-style-type: none"> <li>Less advancement than with larger piece</li> </ul>	
14	<ul style="list-style-type: none"> <li>Manually advanced FB ~1 cm</li> </ul>	<ul style="list-style-type: none"> <li>FB ROI registers well to the control FB</li> </ul>	<ul style="list-style-type: none"> <li>Not fully automated – adding more manual components</li> <li>Multiple iterations (40)</li> </ul>	
15	<ul style="list-style-type: none"> <li>Entire FB osteotomized, including ROI highlighted with Boolean function</li> <li>Bone graft used to fill gaps</li> </ul>	<ul style="list-style-type: none"> <li>Most similar to real-life scenario</li> <li>A lot of FB movement</li> <li>Acceptable result</li> </ul>	<ul style="list-style-type: none"> <li>Least automated of all iterations</li> </ul>	

**Table 4.2** Summary of maximum Hausdorff surface distances between the preoperative UCS skull model and a control skull, and the postoperative reconstruction UCS model and a control skull.

Skull Points	Surface Distances (mm)				RMSE (mm)
	A	B	C	D	
Pre-Op	-6.32	-0.54	-1.20	-1.24	3.28
Post-Op	2.64	0.62	-0.05	-0.55	1.38

**Table 4.3** Maximum surface distance values between the FB and SOB of the reconstruction UCS model compared to the preoperative UCS model.

Recon Model #	Max Surface Distance Values (mm)	
	SOB	FB
1	N/A	4.611
2	N/A	7.768
3	-1.752	3.836
4	4.575	3.775
5	4.670	3.770
6	4.730	3.830
7	4.388	3.788
8	6.763	3.763
9	7.887	3.787
10	7.887	4.187
11	7.889	3.089
12	7.727	8.427
13	7.825	3.625
14	7.678	10.478
15	7.807	10.407

**Table 4.4** Maximum and mean surface distance values between the FB and SOB of the reconstruction UCS model compared to the control skull model.

Recon Model #	Surface Distance Value (mm)			
	FB		SOB	
	Mean	Max	Mean	Max
1	0.346	5.431	N/A	N/A
2	0.103	1.257	N/A	N/A
3	0.476	5.299	0.999	7.619
4	0.523	5.344	1.778	10.838
5	0.551	5.344	2.031	10.880
6	0.530	5.344	0.638	8.08
7	0.534	5.344	0.421	7.401
8	0.287	4.197	1.027	9.574
9	0.516	5.344	0.456	5.400
10	0.712	4.928	0.502	6.186
11	0.852	5.493	0.618	6.280
12	0.015	1.186	0.475	6.113
13	0.491	5.238	0.516	6.395
14	-0.089	0.997	0.535	5.991
15	0.330	0.846	0.488	6.116

**Table 4.5** The highest and the lowest performing models are presented. Overall high performance was determined by highest degree of advancement and/or high degree of normalcy in both ROIs. Overall low performance was determined by lowest degree of advancement and/or low degree of normalcy in both ROIs.

		Recon Model Compared to <u>Pre-Op Model</u>		Recon Model Compared to <u>Normal Model</u>			
		FB	SOB	FB	SOB		
<b>Most Advancement</b>		14	11	12	7	<b>Most Normal</b>	
		15	9	14	9		
		12	10	2	12		
<b>Least Advancement</b>		11	3	11	5	<b>Least Normal</b>	
		13	7	10	4		
		8	4	5	8		

## List of Figures

### Chapter 1

**Figure 1.1** The coronal suture is shown in red. Fusion of the suture on either the left or the right side of the skull leads to anterior plagiocephaly.

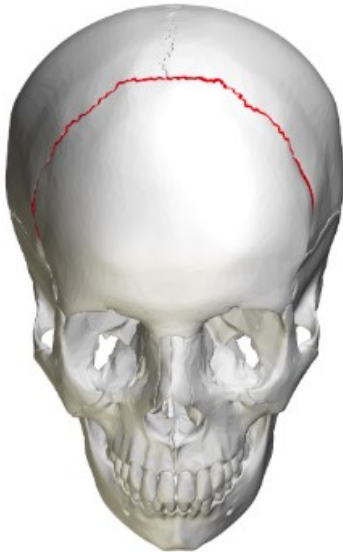
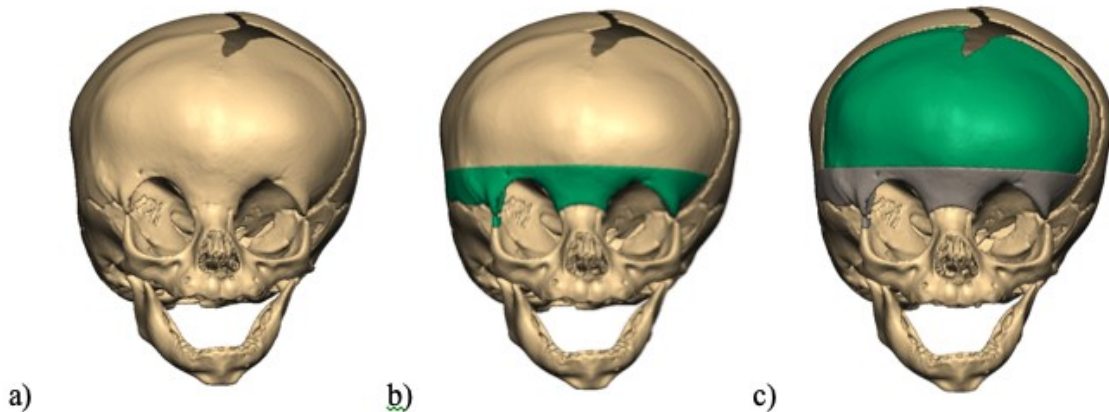


**Figure 1.2** A) Three-dimensional (3D) model of an infant with right-sided UCS. The right coronal suture is fused as demonstrated by the presence of a bony ridge, when compared to the left coronal suture that is patent and depicted as an open space. B) The supra-orbital bar region is highlighted in green. This is the area that is above the eye sockets. C) The supra-orbital bar is shown in grey, and the frontal bones that constitute the forehead region are highlighted in green.



## Chapter 2

**Figure 2.1** CT scans are imported into 3D Slicer with axial, sagittal, and coronal views visible (top row). Panels A to E demonstrate the manual alignment process. The star indicates which view the described changes are best visualized. From A to B, the anterior cranial vault and the sella turcica are aligned with an inferior translation, as best viewed on the sagittal view. From B to C, the frontal bone contours are aligned with an anterior translation, again best viewed on the sagittal view. In panel C, a line that bisects the frontal bones of each skull is imagined at the metopic suture in the axial view. The goal from steps C to D is to rotate the normal skull image in an axial plane so that these lines assume a parallel relationship. Then, the normal skull is translated in the left-right dimension to align the metopic sutures (D to E). Panel E demonstrates the end result of the manual alignment step. Panel F demonstrates the end result after the registration step. It is clear here that the non-synostotic frontal bones (patient's left in this case) align well (white arrow). A subjective assessment of good bony overlap of the non-synostotic frontal bones in the axial slices is the endpoint of the registration step in this workflow. Once registered, the discrepancy in the forehead region on the synostotic side between the two skulls is apparent.

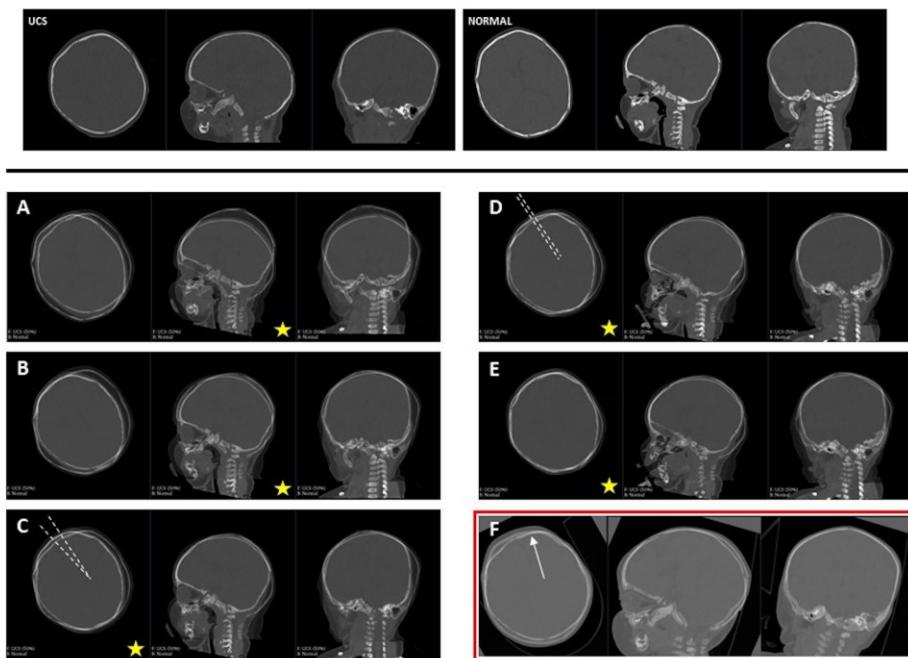


**Figure 2.2** In this image, the frontal bones corresponding to the synstotic side of the UCS skull are segmented. The blue skull is the UCS skull and the beige skull is the age and sex matched control skull. Surface models are generated representing the segmented frontal bones. The point where there is the largest distance between the segments is automatically identified and the distance is calculated in subsequent steps. This represents the area where there is the largest deviation in the UCS skull from a normal control skull.

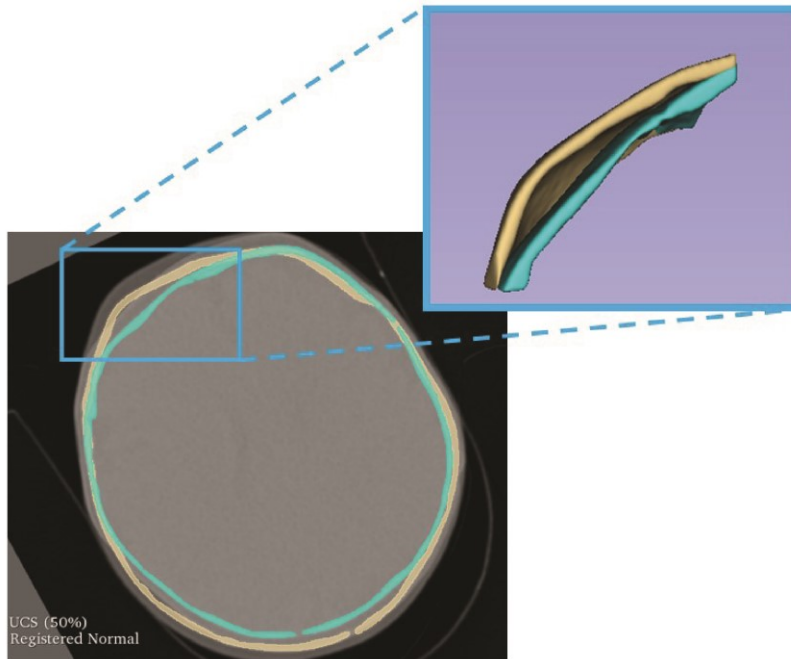


**Figure 2.3** The goals and potential pitfalls of the segmentation step are outlined in this figure, as well as the use of color maps to verify the location where the deformity index is calculated. Panel A shows the worm’s eye view of the segment of frontal bone isolated from the CT scan (top left). Panel B is a color map of the segment of frontal bone taken from the synstotic side in the UCS patient (blue skull), with information regarding the surface distances to the corresponding segment of the normal frontal bone (beige). Warm hues denote a distance further away from the UCS skull, which correspond to areas on the UCS frontal bone that are flattened when compared to the normal skull. Cool hues denote areas between the two skull segments that are close together, corresponding to areas of less deformity. In panel B, it is clear that the deformity index value of 7.329 mm is calculated from within the frontal bone segment, confirming that the value is calculated in the region of interest. In panel C, the same value is derived from a larger segment of the frontal bone. This emphasizes that the deformity index value will be identical between

segments that are limited to the constraints outlined in the workflow. In panel D, the segmentation did not include sufficient frontal bone inferiorly, resulting in a smaller deformity index that is not representative of the true deformity. This is confirmed by the color map, which has warm hues at the inferior edge of the segmentation, and disappears from the same edge when the maximum threshold for the color map is reduced. This confirms that the deformity index was calculated from the edge of the segmentation, is not representative of the region of interest, and the segmentation step would require revision. Finally, panel E demonstrates what may happen if the first constraint is violated and the segment includes areas outside of the region of interest. In this case, the superior orbit of the UCS skull was included in the segmentation, again resulting in an erroneous deformity index that is not representative of the deformity at the frontal bones. In the confirmation step, it is clear that the maximum surface distance of 14.638 mm is derived from the region of the orbit as the warm hues are restricted to the portion of the superior orbit.

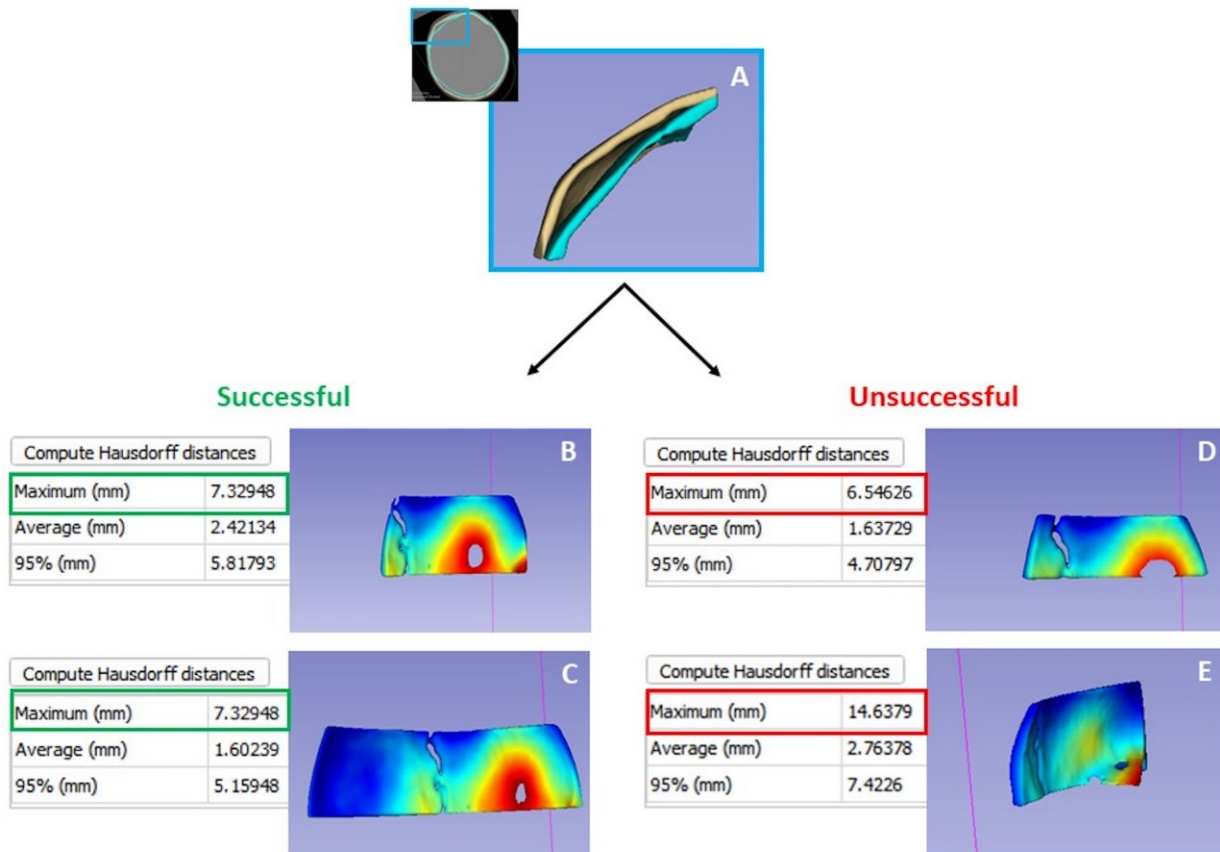


**Figure 2.4** Panel A) depicts the bird's eye view of the skull assigned the smallest surface distance value (1.99 mm), and panel B) depicts the same view of the skull assigned the largest surface distance value (10.36 mm). Skull A has a more symmetrical appearing forehead than skull B, and therefore the assigned index value corresponds with a subjective assessment of frontal bone deformity, at least at the extremes of surface distances.

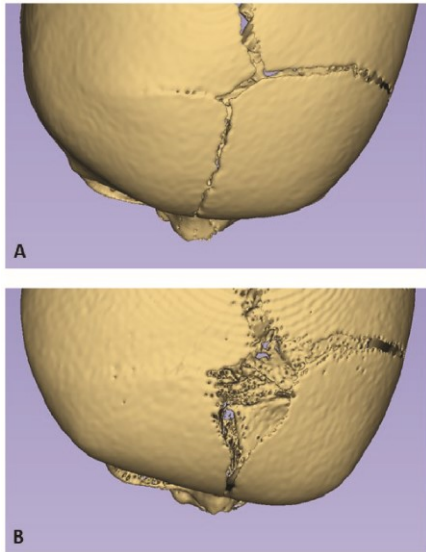


**Figure 2.5** Correlation between the maximum surface distances between the workflow trial one and trial two was 0.93 demonstrating high reliability and a measure that is reproducible.

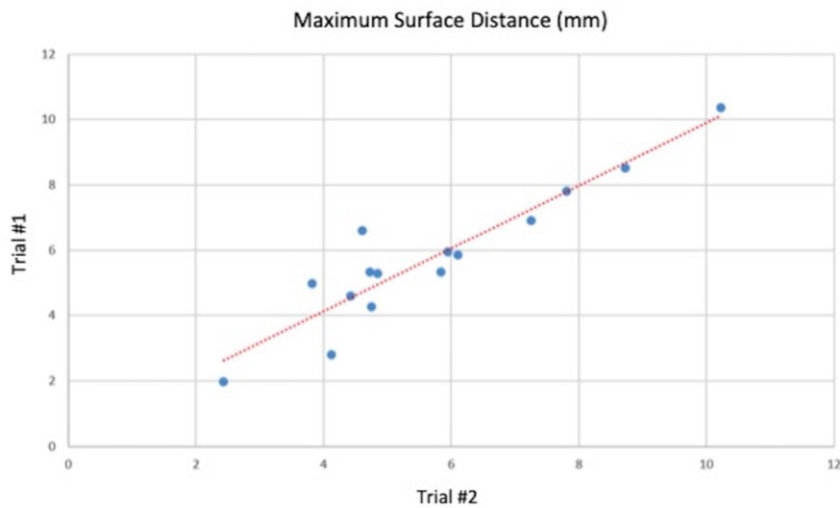


**Figure 2.6** An axial slice of a preoperative (blue) and postoperative (purple) CT scan of a patient with UCS who underwent corrective surgery are registered. Areas where the preoperative and postoperative skull register and align well are displayed in a purple-blue color. The discrepancy between the frontal bones on the synostotic side (patient's right side, top left in figure) is apparent. In this application, the measurement index corresponds to the largest distance between the blue and purple skulls on the synostotic side.

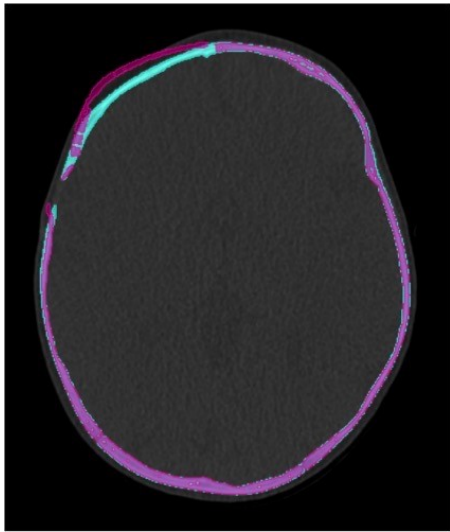
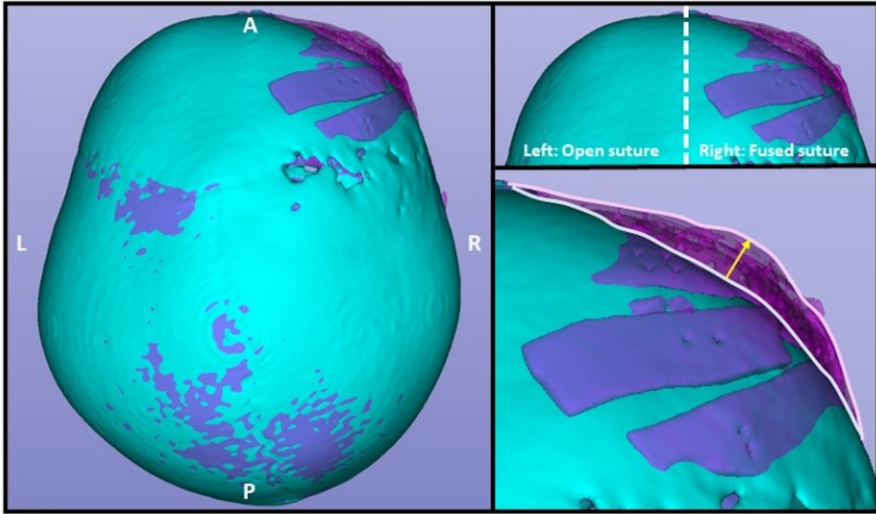


**Figure 2.7** The preoperative (blue) and postoperative (transparent purple) CT scans in a patient with UCS treated with a unilateral FOA are registered in order to appreciate the degree of frontal bone advancement. The postoperative skull is transparent in order to appreciate the forehead contour of the preoperative skull. In the left panel, the improved forehead symmetry of the postoperative skull is noticeable on the bird's eye view. In the top right panel, the non-synostotic (left) and synostotic (right) sides of the forehead are outlined. This patient was treated with a unilateral advancement, meaning only the right sided frontal bones were advanced. In the bottom right panel, the light purple curve outlines the new contour of the forehead in the postoperative skull, compared to the light blue curve, which outlines the preoperative contour. The yellow arrow highlights the degree of advancement visible from this view.



### Chapter 3

**Figure 3.1** Distribution of surface distance values among the UCS skull cohort.

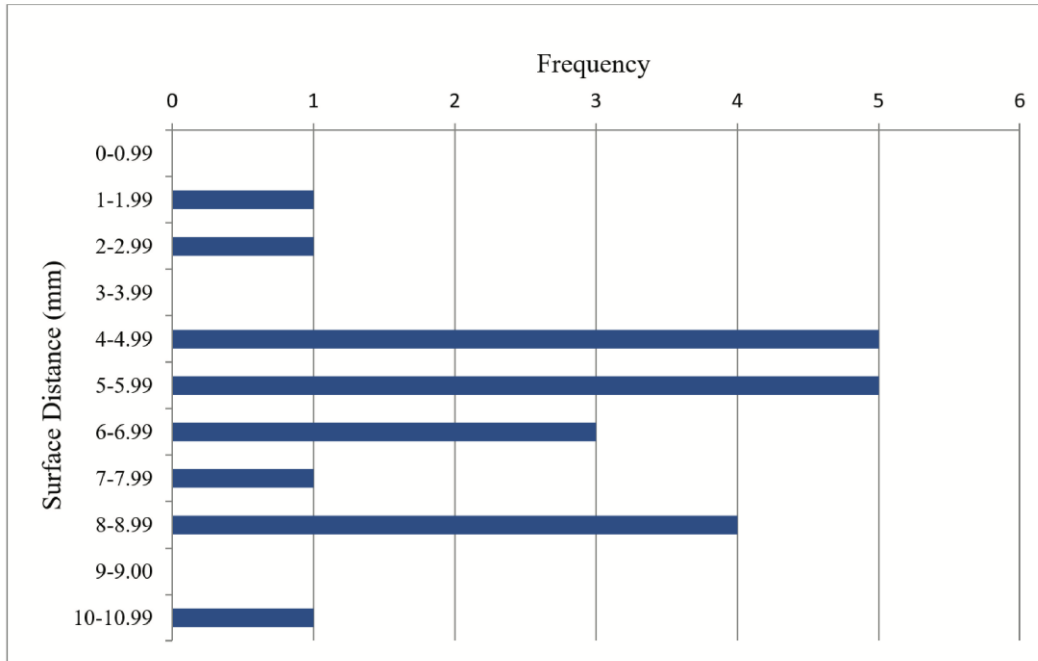


**Figure 3.2** Examples of a skull models as they appeared on the computer screen. The skull on the left is an example of a normal 3D skull model generated for this study. The skull on the right is an example of a UCS 3D skull model generated for this study.

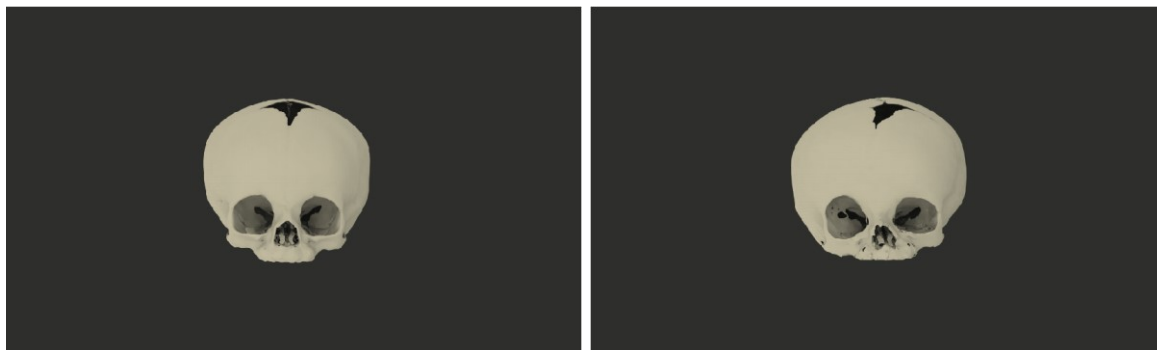


**Figure 3.3** Experimental setup. Skull raters viewed the skull images on a laptop computer screen and were asked to categorize each skull as ‘normal’ or ‘abnormal’. Responses were recorded on

an answer sheet. Each skull was displayed for 0.3 seconds, and raters had 5 seconds to record a response.

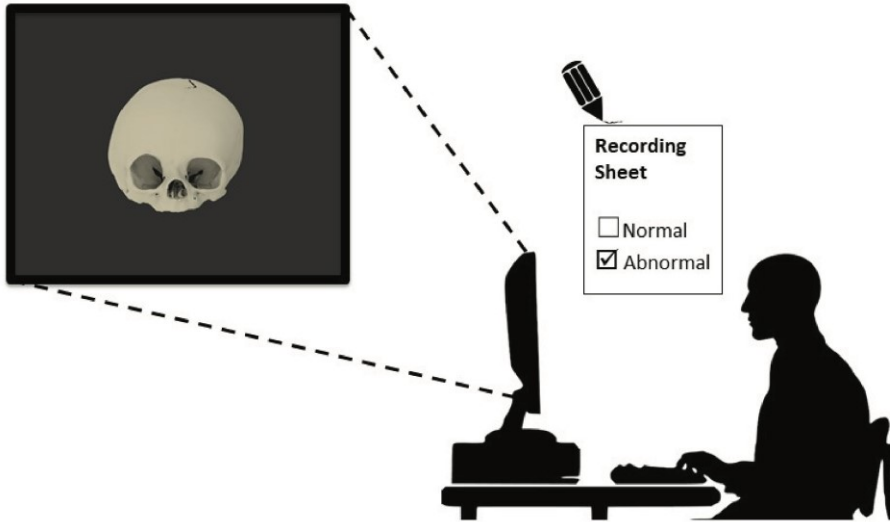


**Figure 3.4** Overview of workflow used to determine surface distance values.

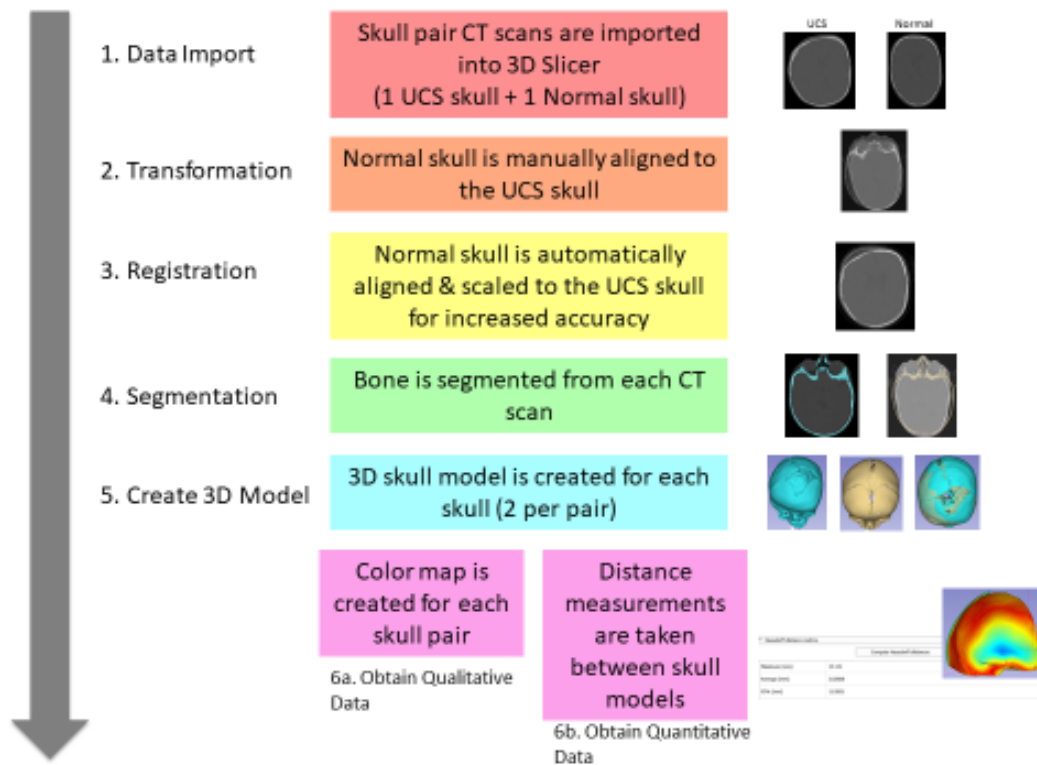
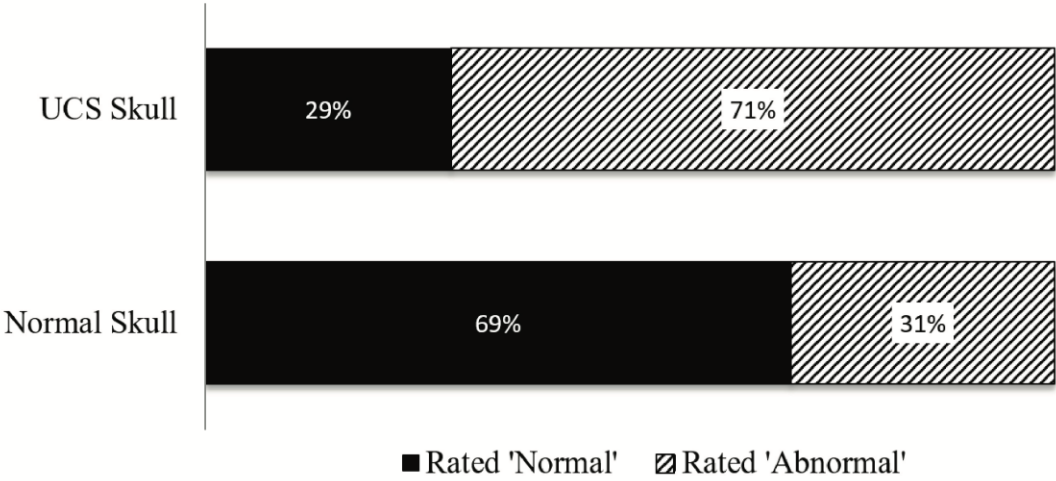


**Figure 3.5** Results of the chi-squared analysis of skull rater responses.



## Chapter 4

**Figure 4.1** The UCS skull (left) is shown in the bird's eye view and frontal view. The normal control skull (right) is shown in the same views. The frontal bone on the side with the fused suture in the UCS skull (pink star) is flattened when compared to the contralateral side and the normal control.

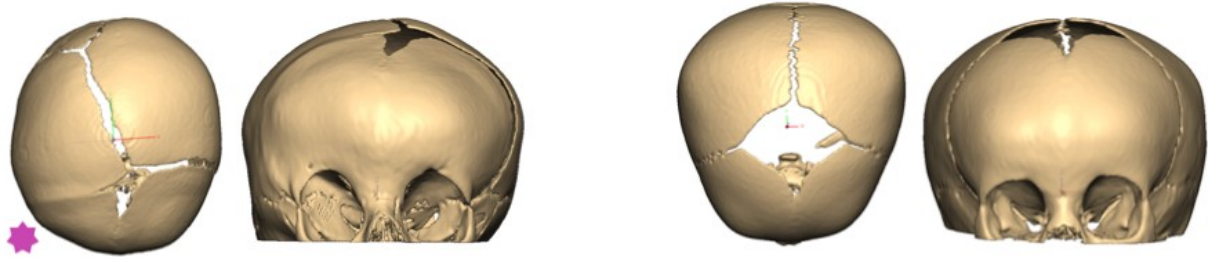


**Figure 4.2** The SOB (green) is virtually selected using the Lasso and Square Select Clay tools.

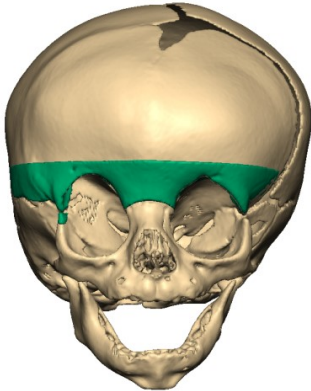


**Figure 4.3** The right and left frontal bones (green) are selected using the lasso and square select clay tools.

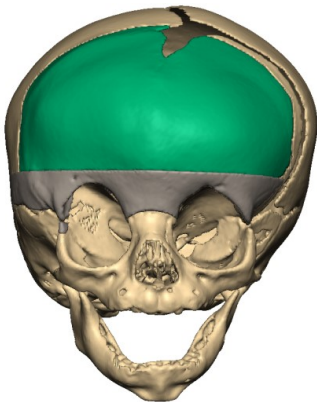


**Figure 4.4** Bone pieces osteotomized in a FOA surgery are removed from the skull model. The resulting skull model is shown on the right. This model is used to build the final reconstruction model. Note - only the frontal bones are removed in the skull pictured on the right. In a FOA procedure, both the SOB and the FBs would be removed, reshaped, and fixated.

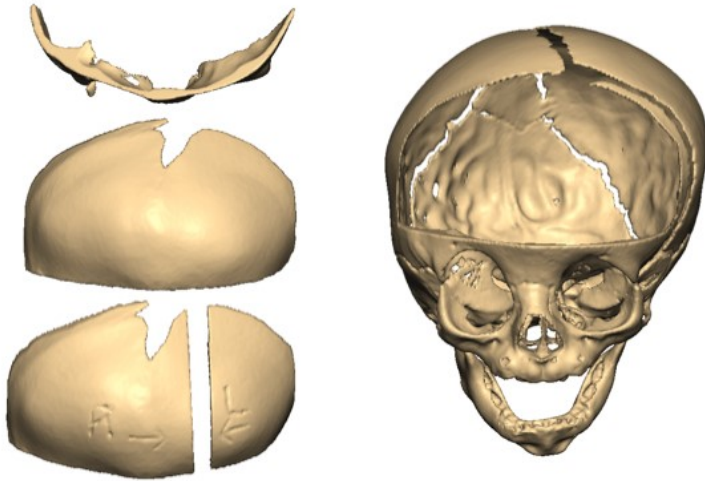


**Figure 4.5** The original SOB from the UCS skull is shown on the left. On the right, the Bend Clay tool is shown altering the shape of the SOB. The area in green is being manipulated virtually.

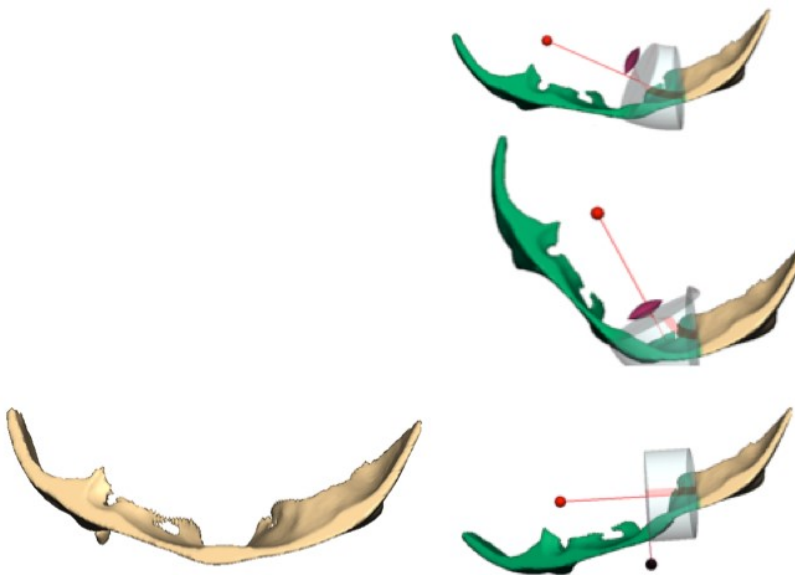


**Figure 4.6** An example of a FOA procedure for UCS is shown. A is the preoperative skull model, and D is the reconstruction model. In B, the SOB is shown being translated anteriorly. In C, the right and left frontal bones are being rotated, and exchanged from right to left.

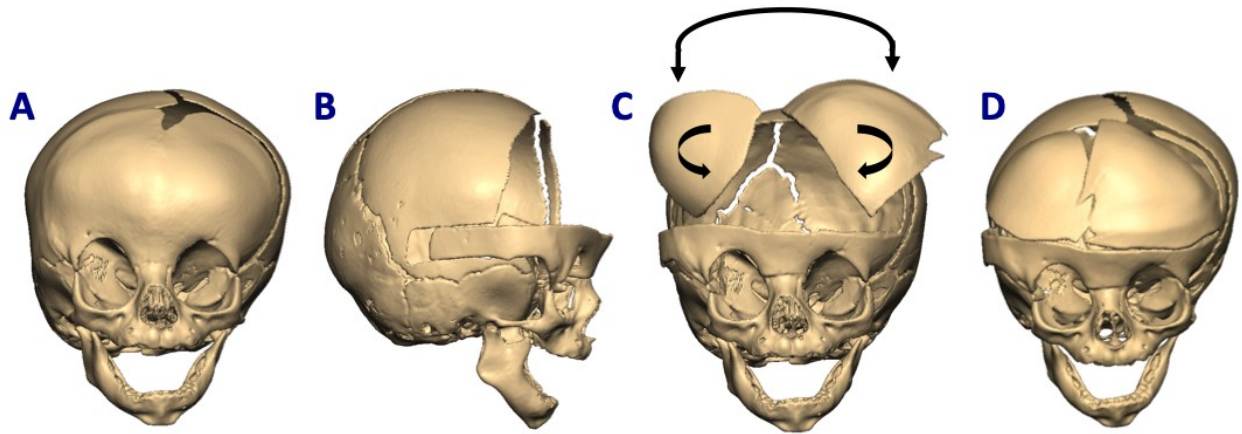


**Figure 4.7** The virtual workflow for a FOA procedure in a patient with UCS is shown. This is one example of how the bone components can be manipulated in order to approximate a normal head shape.

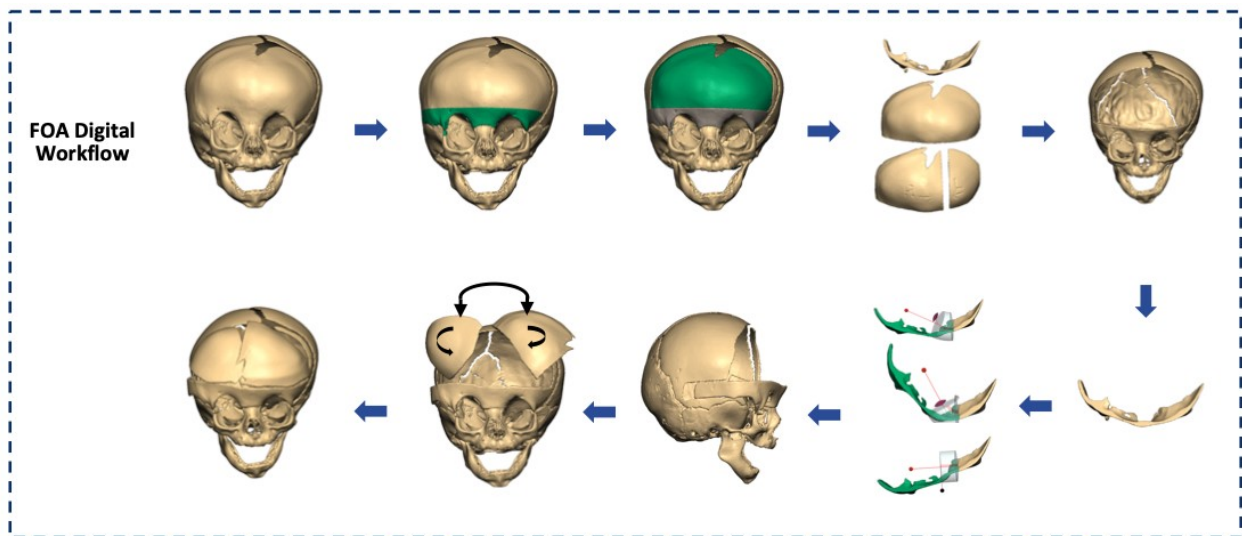


**Figure 4.8** In Panel A, the UCS skull model (grey) and the control skull model (beige) are shown registered to each other. The area at the frontal bones where the grey skull is posteriorly positioned compared to the beige skull is apparent. This region is outlined in Panel B.

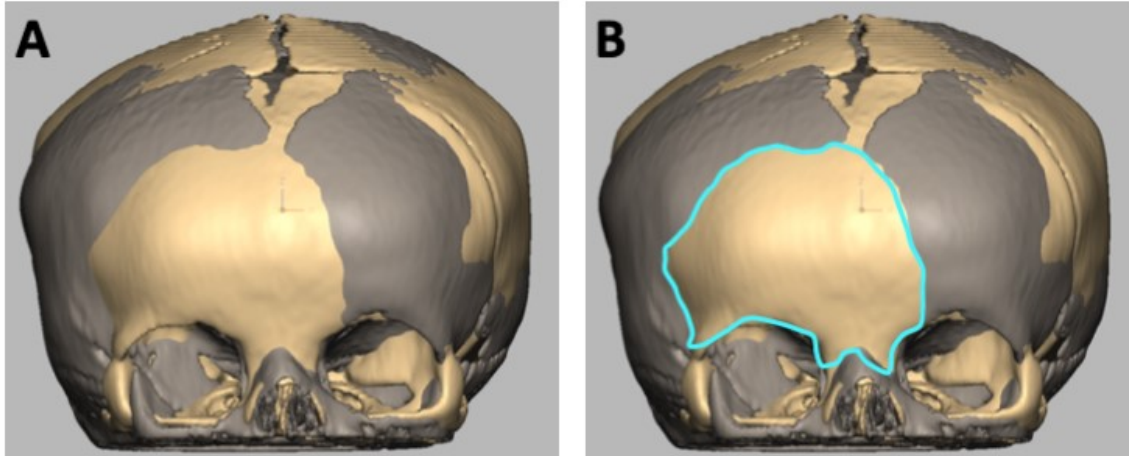


**Figure 4.9** In Panel A, a bird's eye view of the UCS skull and the control skull registered to each other is shown. The red line outlines the contour of the normal skull forehead. In Panel B, a bird's eye view of the UCS skull is shown. In Panel C, the area where the UCS forehead is retruded compared to the control skull is apparent. The white arrow highlights the anterior translation of the frontal bones that a surgeon aims to achieve in UCS with an FOA procedure.

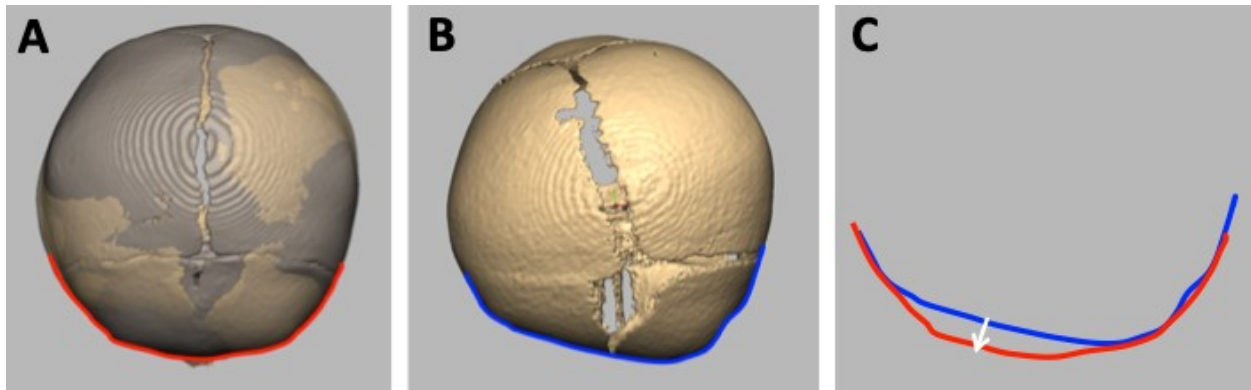


**Figure 4.10** In Panel A, the UCS skull is shown after the control skull is subtracted from it using the Freeform Boolean function. The gaps in the skull model are areas where the normal skull intersected or overlapped with the UCS skull. The FB ROI is highlighted in green in Panel B.

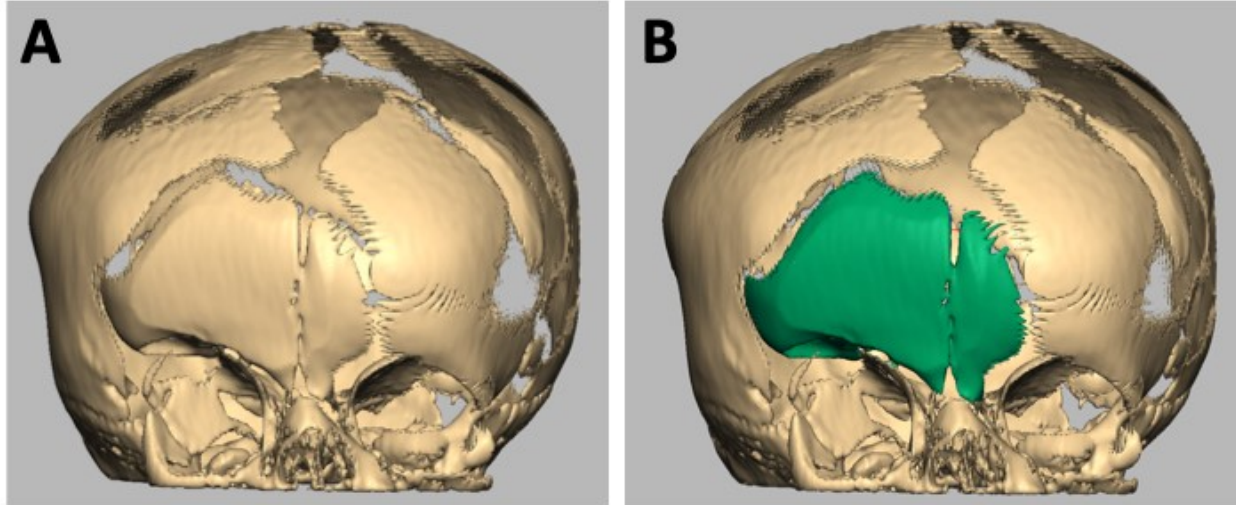


**Figure 4.11** With the SOB ROI defined, the FB ROI (grey) is refined with an inferior margin that does not cross the superior margin of the SOB.

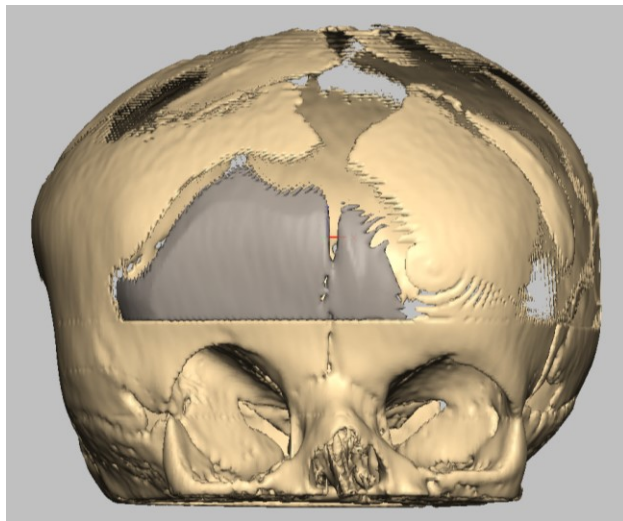


**Figure 4.12** The UCS SOB (beige) is registered to the control SOB (grey). On the patient's left side, which corresponds to the non-synostotic side of the skull, the UCS SOB is registered well to the control SOB. Areas that are well registered have good bony overlap between the grey and the beige skulls. On the patient's right side, corresponding to the synostotic side, the UCS SOB is clearly retruded compared to the control SOB and is not well registered. The distinction between the abnormal and normal components of the UCS SOB (red line) is the point where the UCS SOB transitions from being well registered to the control SOB, to where it is not well registered to the control SOB.

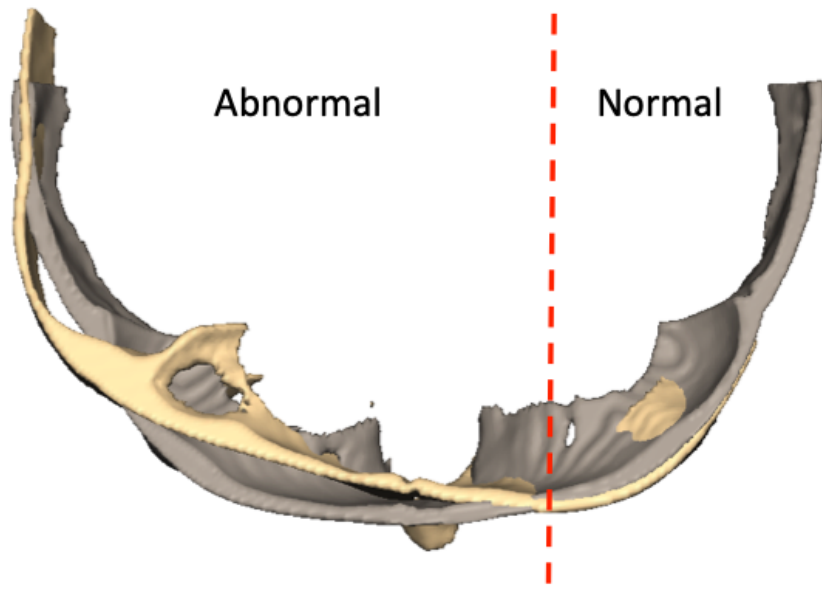


**Figure 4.13** In A, the UCS SOB (beige) and the control SOB (grey) are registered and shown from a bird's eye view. In B, the control SOB is subtracted from the UCS SOB via a Boolean function. Panel C demonstrates the problematic resulting UCS SOB with the various areas of missing bone.

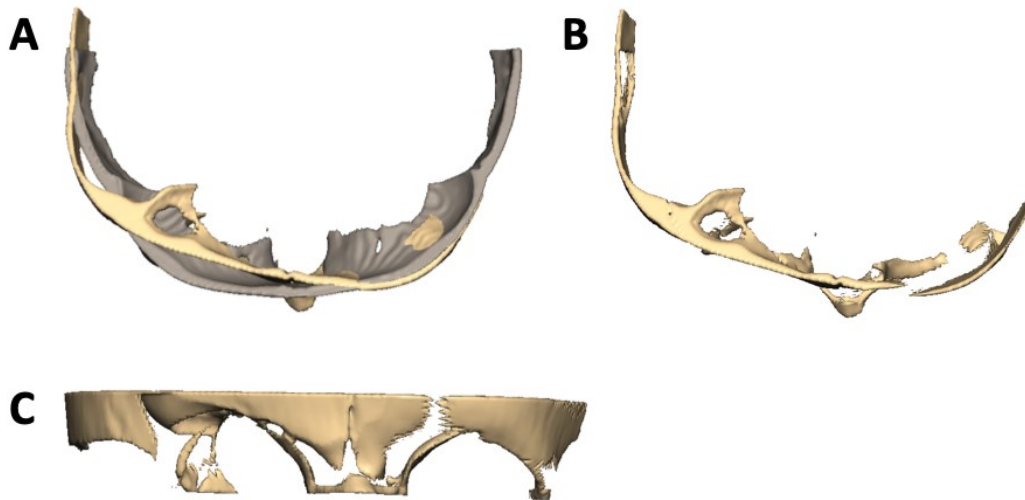


**Figure 4.14** Panel A – the UCS SOB after the control SOB is subtracted from it results in excessive bone loss. The green portion is the abnormal component of the SOB, and the area of interest when recreating a normal SOB. Panel B – subtracting the normal component of the SOB from the abnormal component results in a depression. Panel C – the distinction between the

normal and abnormal SOB components is identified and used as the boundary to select the normal component. Panel D – the abnormal SOB ROI remains and is used in multiple iterations to approximate a normal SOB.

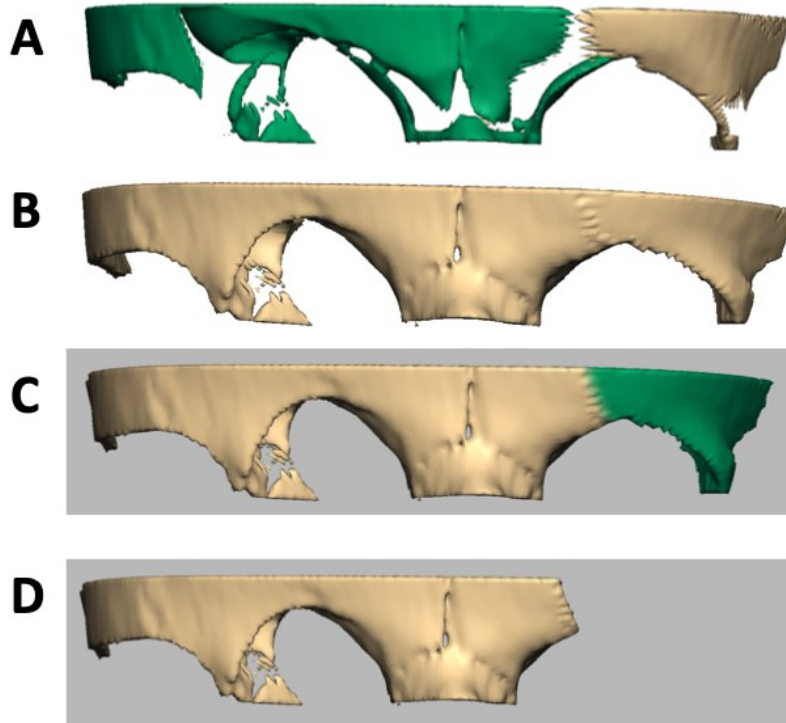


**Figure 4.15** Panel A – the intersection between the normal and abnormal SOB is used to define where to initially bend the SOB. Panel B – The SOB after the first bend. Panel C – the SOB after the second bend. Panel D – the SOB after the third bend. Panel E – the final reconstructed SOB after the fourth bend.

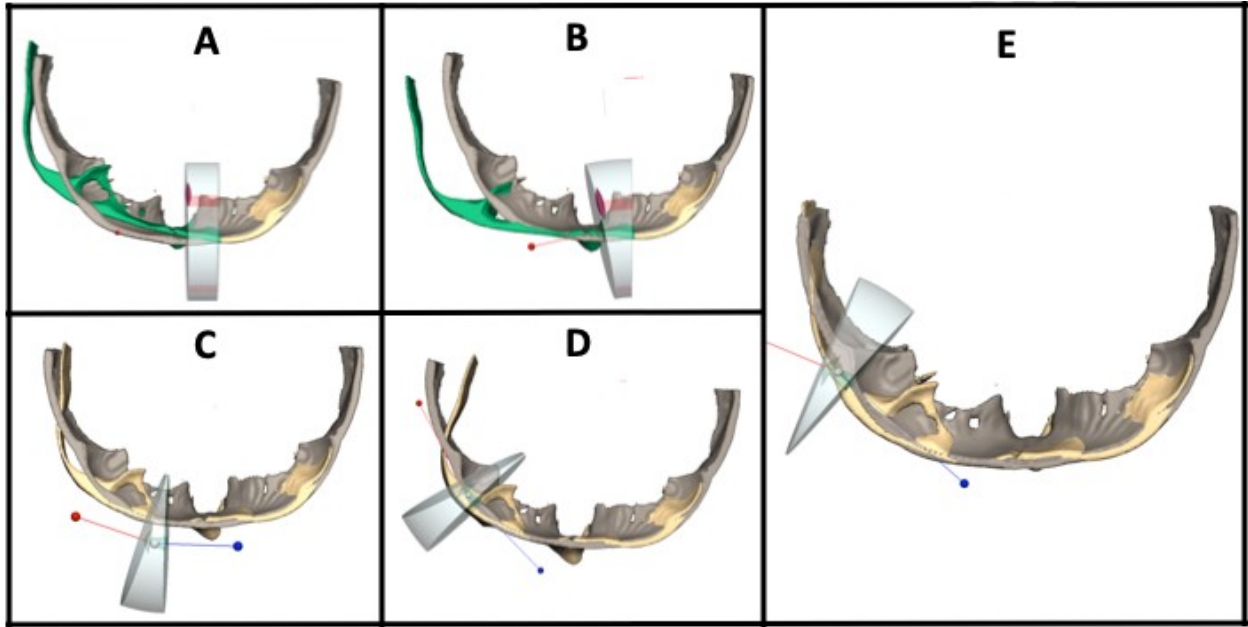


**Figure 4.16** In iteration #3 of the automated workflow, the FB ROI does not make a large visibly noticeable advancement. Panel A depicts the RB ROI. Panel B demonstrates the FB ROI (beige) after the first registration to the control skull (grey). Prior to registration, no part of the beige ROI was visible in front of the control skull. Panel C shows the FB ROI after the tenth and final registration. It is noticeable that the surface area of the beige FB ROI that is in front of the grey control skull has increased when compared to Panel B. This indicates that the FB ROI advanced further between registrations one and ten. Panel D shows the final reconstruction model.

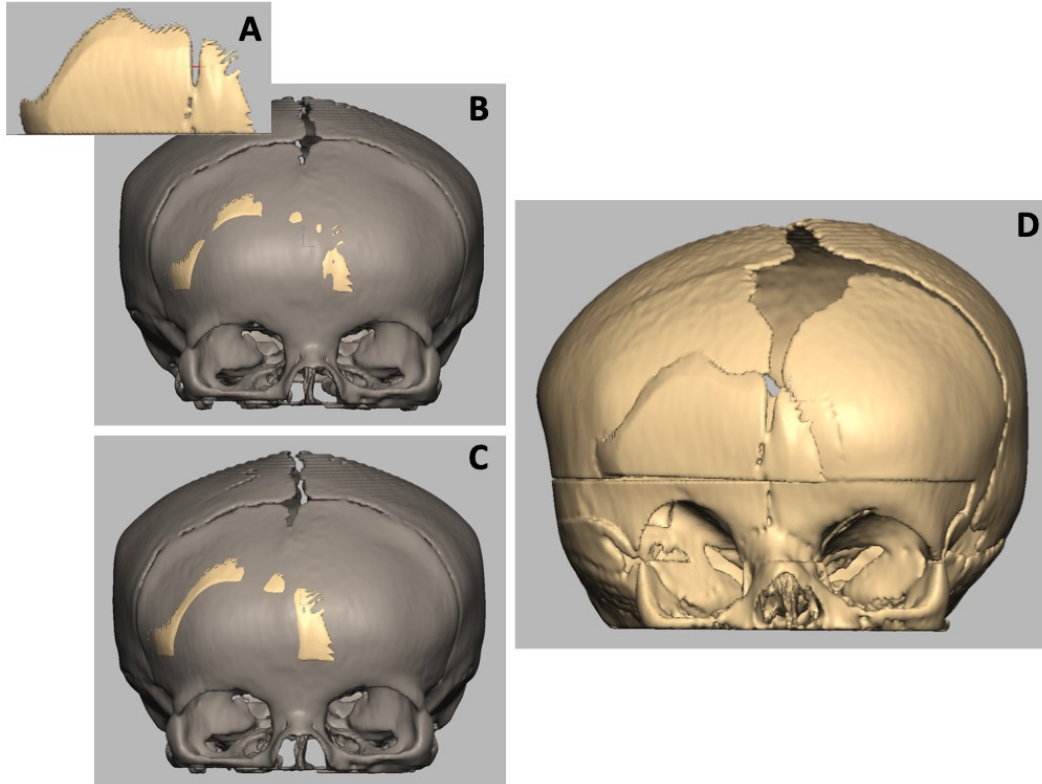


**Figure 4.17** In iteration #2 of the automated workflow, the FB ROI (beige) makes a visibly noticeable advancement, translation, and rotation to approximate the shape of the control skull (grey) forehead. The improved contour of the forehead is noticeable on the worm's eye view of the skull models. In the top left image, the UCS FB ROI (beige) is seen completely posterior to the control skull forehead, which is transparent in these images in order to visualize the FB ROI throughout the registrations. There were no changes made to the SOB in this reconstruction model.

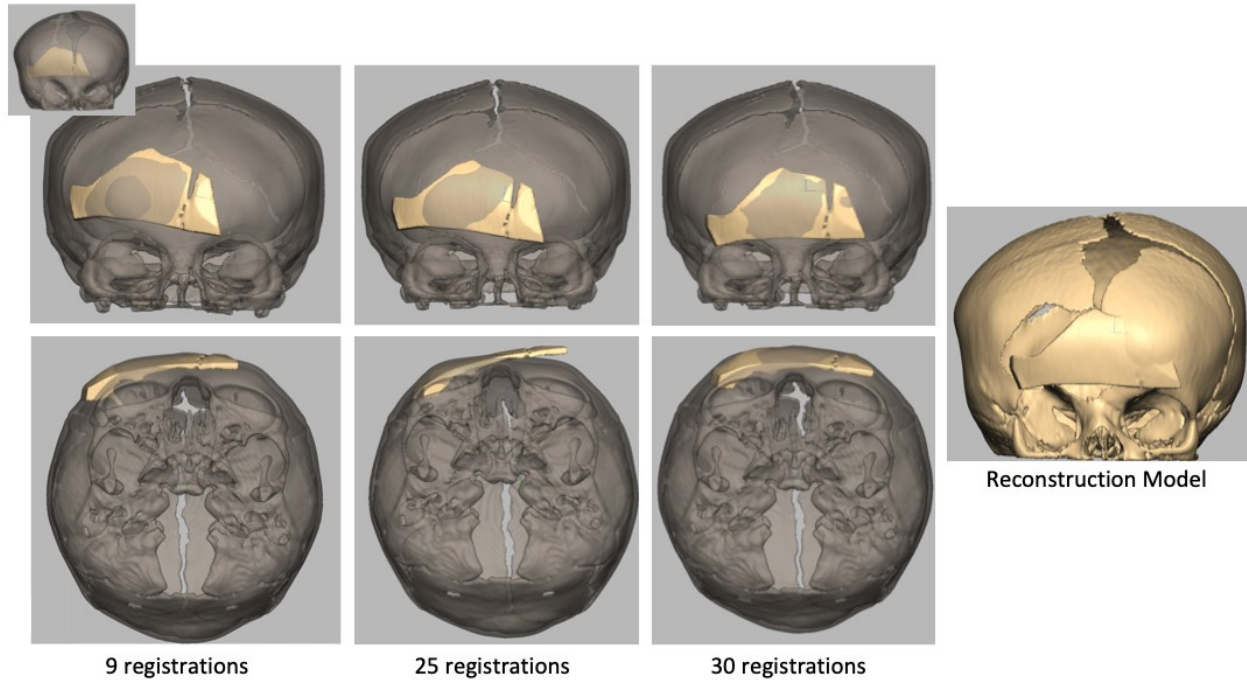


**Figure 4.18** Points A and B represent the right and left SOB of the skull model, and points C and D represent the right and left frontal bones, respectively. These represent the four points where maximum Hausdorff surface distance measurements were taken to analyse the shape of the virtually reconstructed skull.

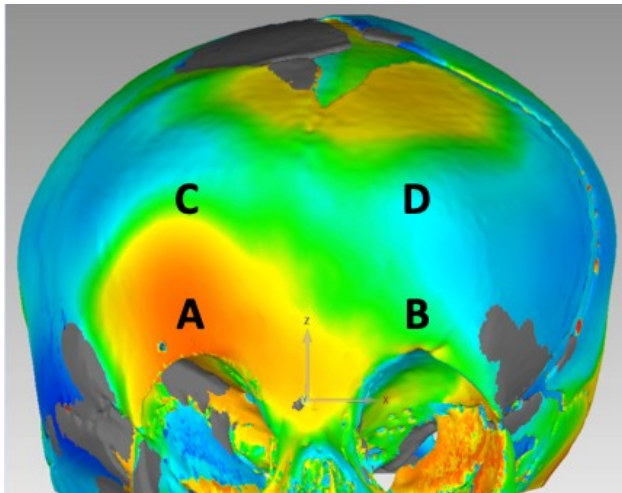


**Figure 4.19** Color maps displaying surface distances values between the preoperative UCS skull model and the control skull (left), and the reconstruction UCS skull model and the control skull (right). Warmer tones represent larger distances between the skull model and a normal skull,

representing areas that are less similar to a normal skull than cooler tones.

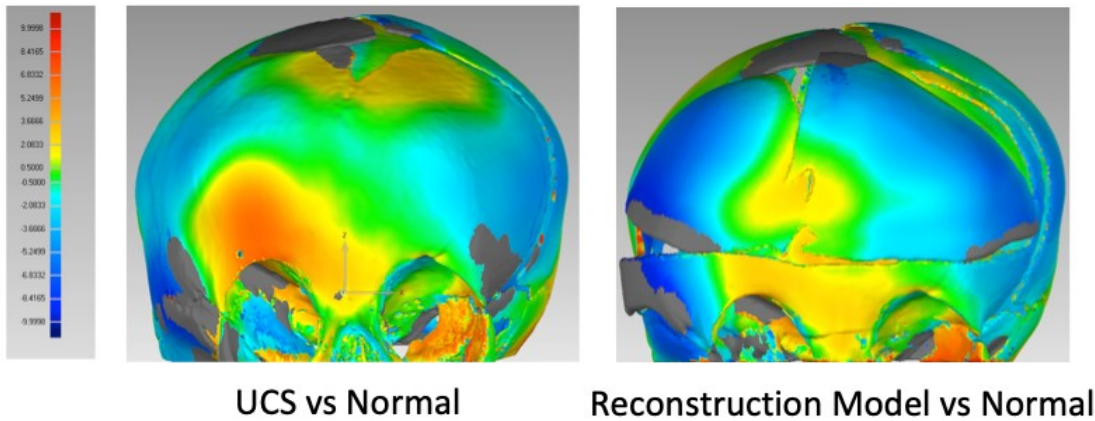


**Figure 4.20** Color maps depicting the maximum surface distances calculated between the preoperative UCS skulls and the reconstruction models demonstrate the virtual surgical changes. Warm tones indicate models that have achieved a larger advancement.

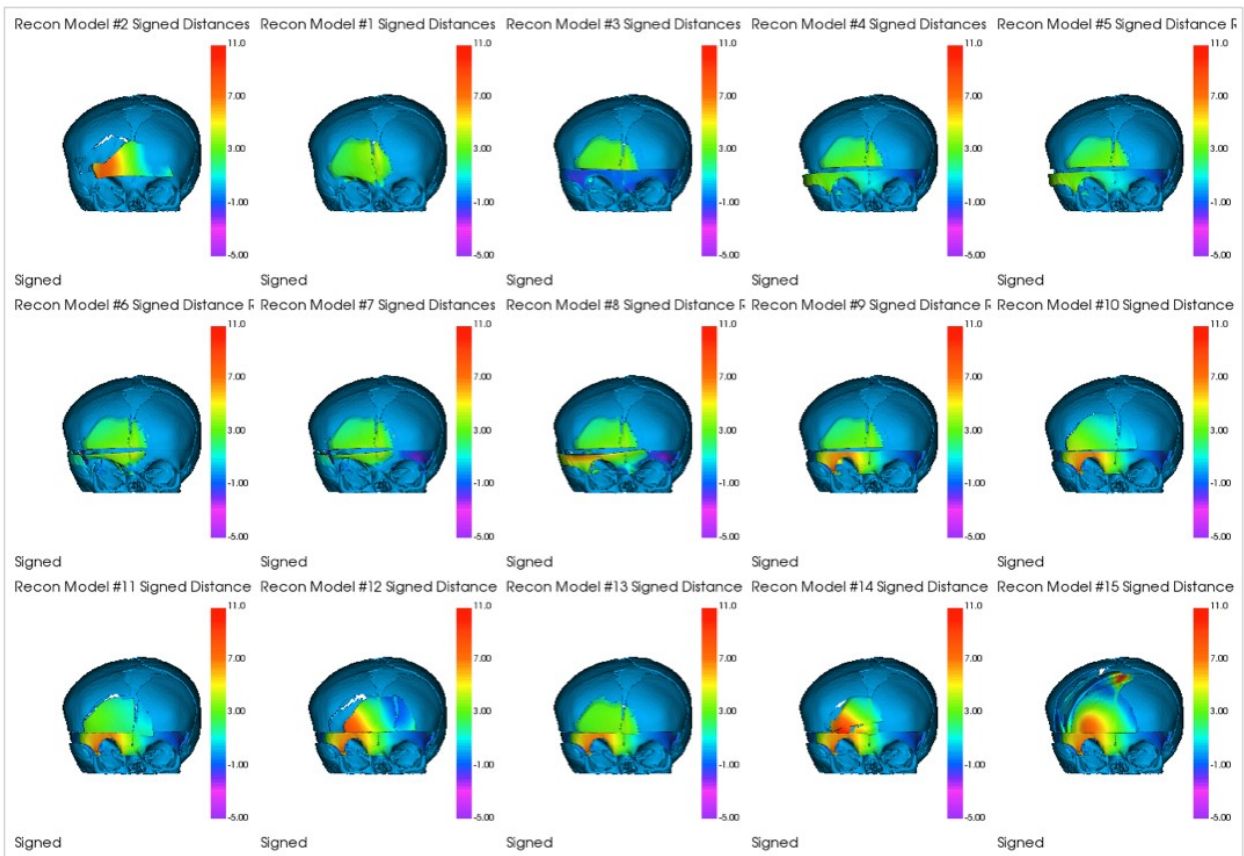


**Figure 4.21** Color maps for the FB ROI for the 15 reconstruction models are shown. Cooler tones indicate a small distance between skulls, and warmer tones indicate a larger distance.

Frontal bones in this figure that are bluer are more similar to a normal reference skull, and frontal bones that have areas of green are less similar to a normal reference.

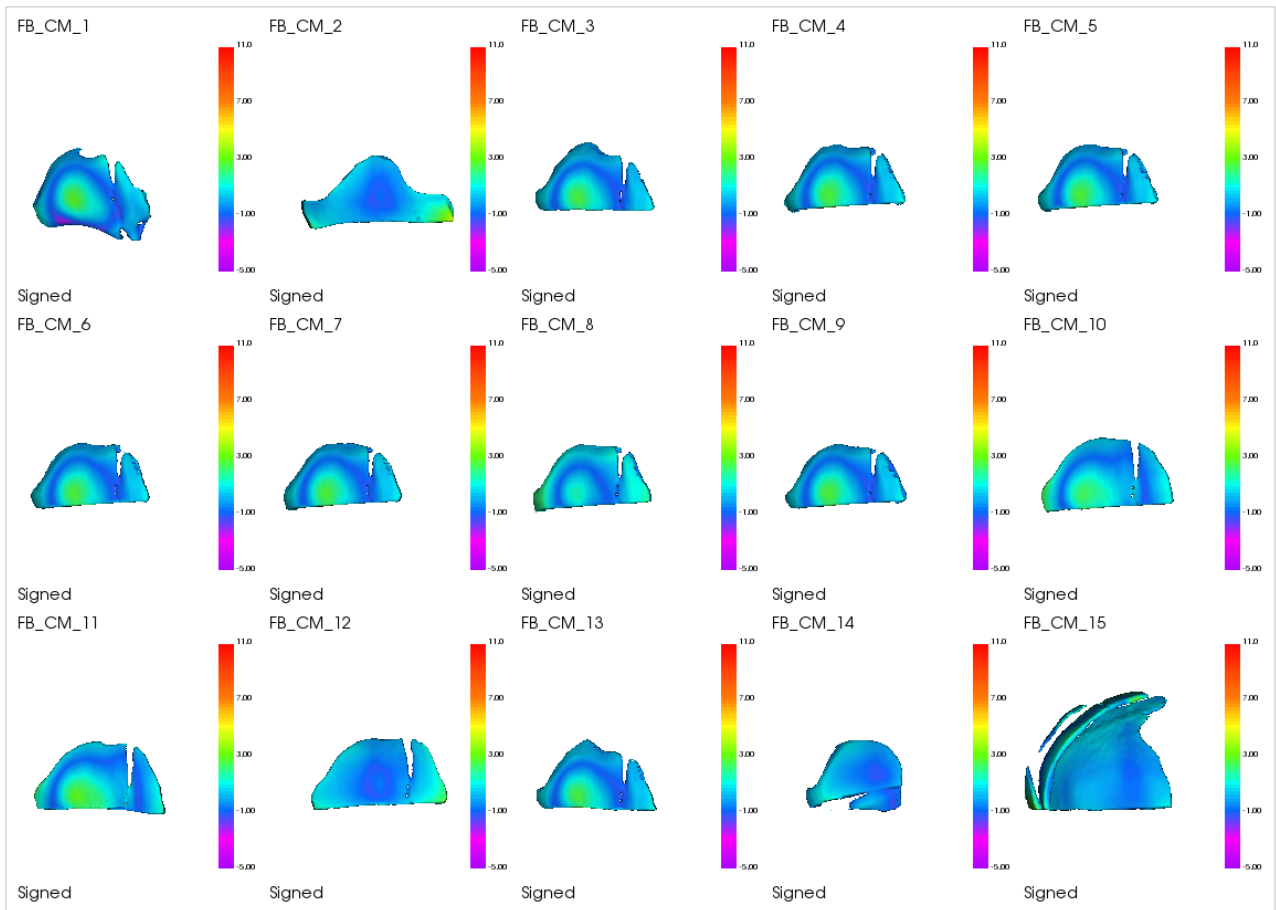


**Figure 4.22** Color maps for the SOB ROI for the 13 reconstruction models that isolated the SOB are shown. Cooler tones indicate a small distance between skulls, and warmer tones indicate a larger distance. Cooler tones indicate similarity to a normal reference skull, and warm tones indicate areas where the SOB was not close in shape to the normal reference.

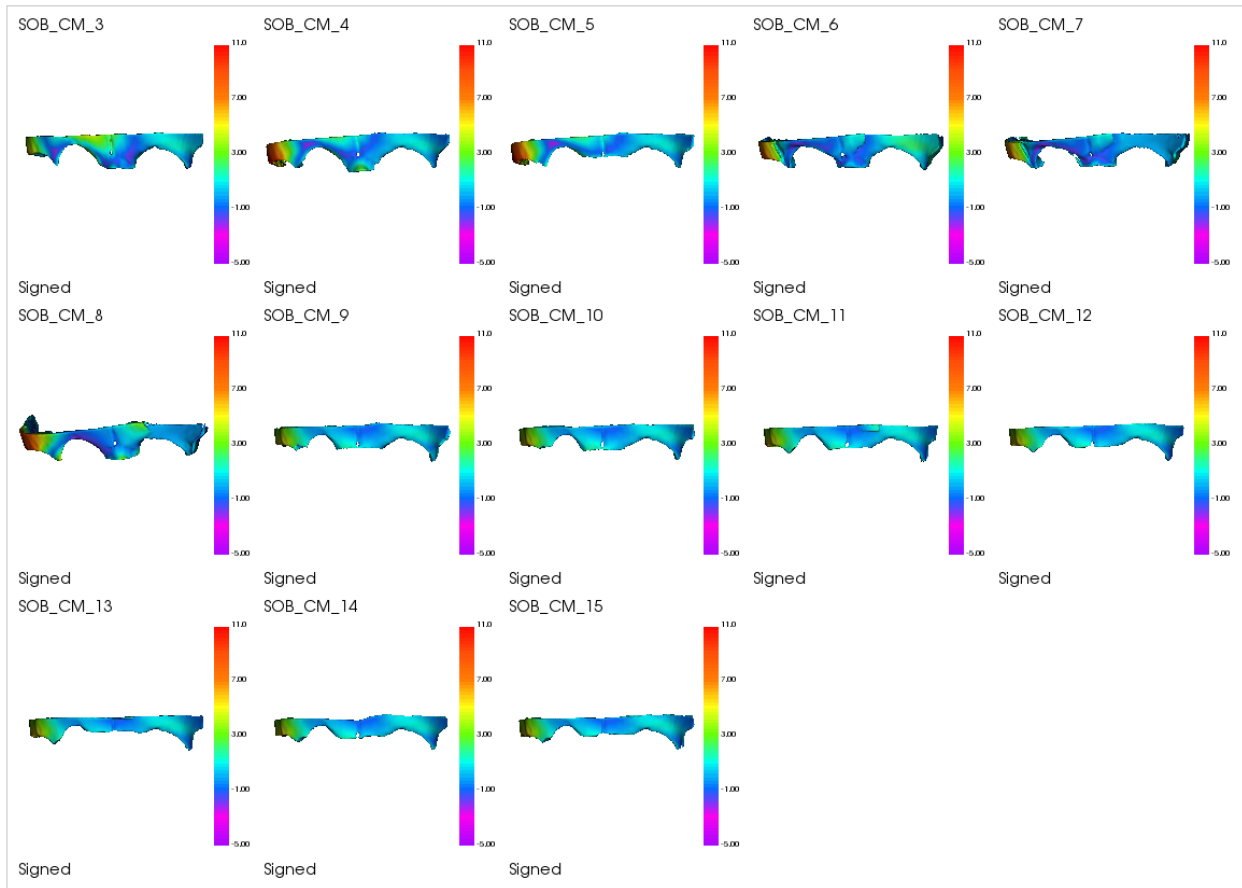


**Figure 4.23** Reconstruction models #5 (top row) and #8 (bottom row) were poor performers among the fifteen automated workflow iterations. The A panels show the reconstruction models, B panels show the comparison to the preoperative skull, and C panels show the comparison to the normal skulls. The FB ROIs when derived and registered fully automatically do not result in a much improved forehead contour.

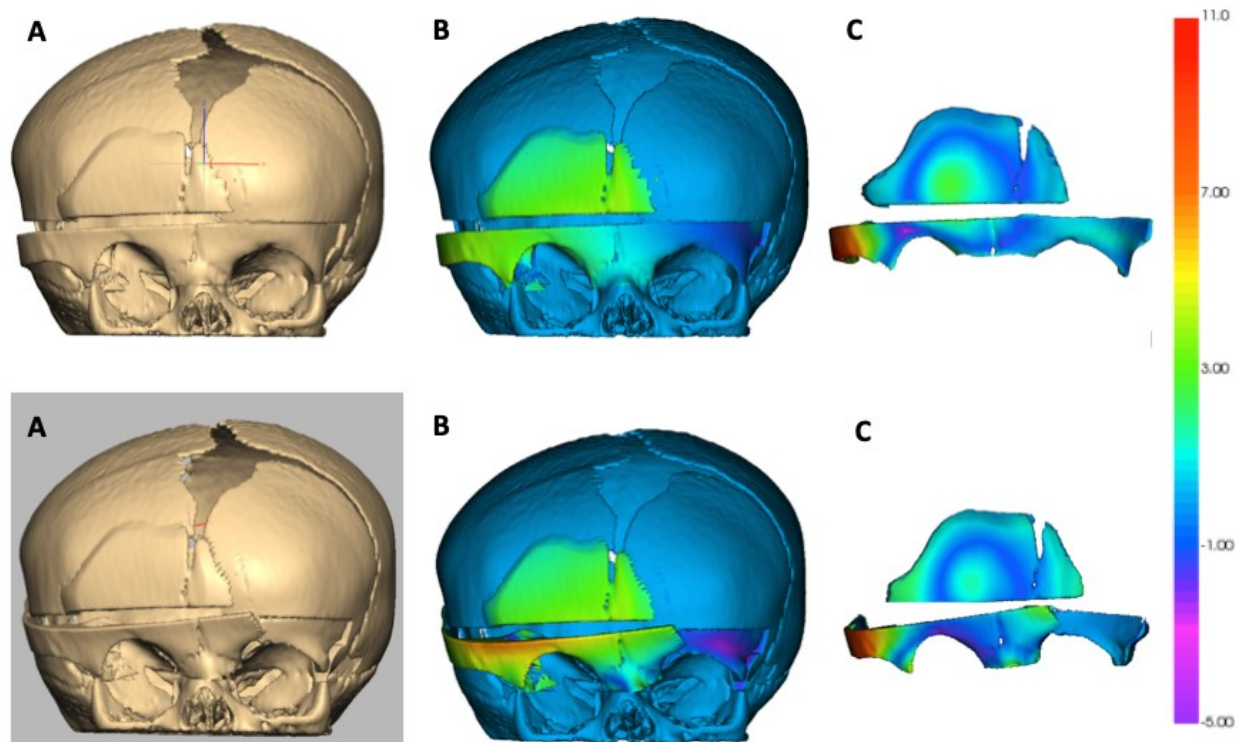


**Figure 4.24** Reconstruction model #12 is displayed (Panel A), along with the comparison between the preoperative skull (Panel B), and the normal skull (Panel C). The edges of the FB region in model #12 are manually smoothed based off the ROI defined by automation. The resultant skull was closer in shape to a normal skull, suggesting the edge smoothing is an important feature to consider in a final algorithm.

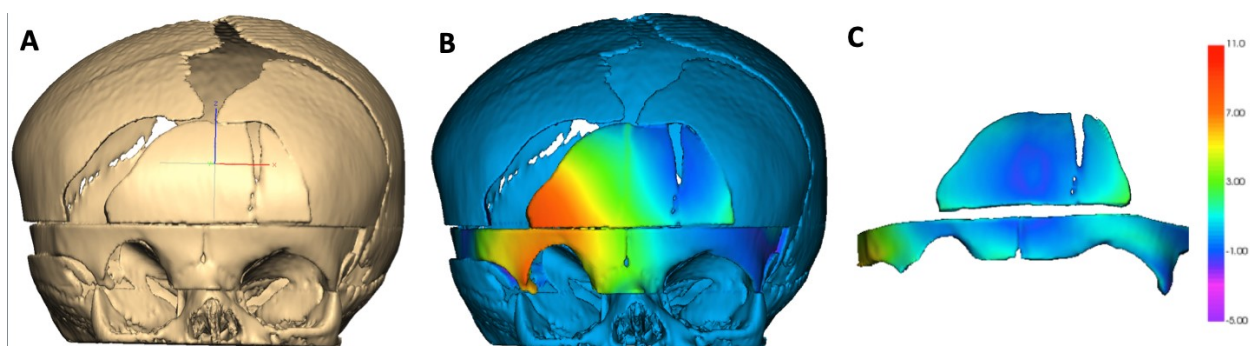


**Figure 4.25** Reconstruction model #7 on the left achieved 4.388 mm of advancement in the virtual FOA compared to Reconstruction model #8 on the right (6.763 mm). However, model #7 was closer in shape to a normal model. The degree of downward rotation of the right SOB in model #8 might account for this discrepancy.

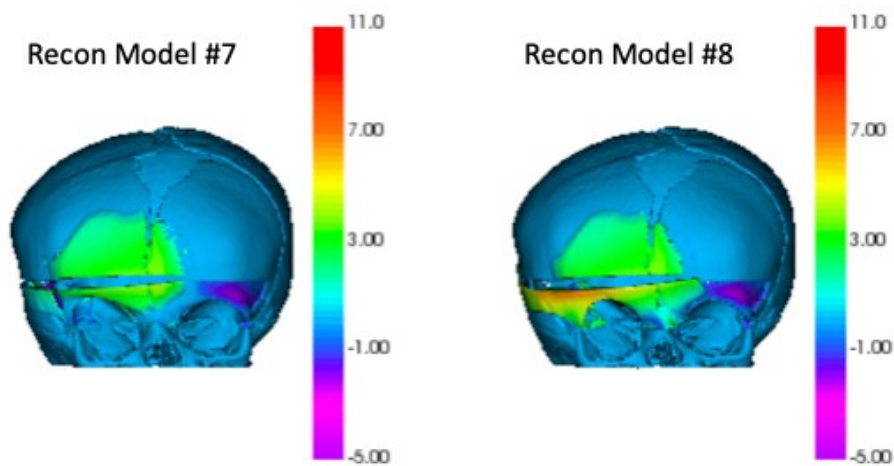
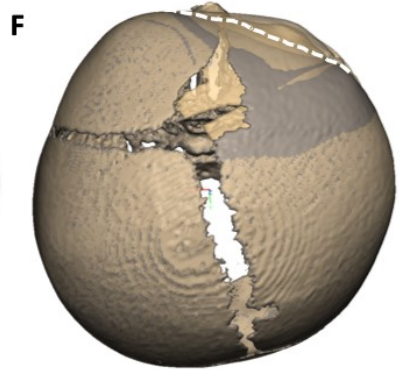
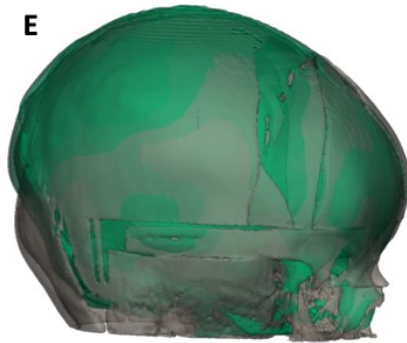
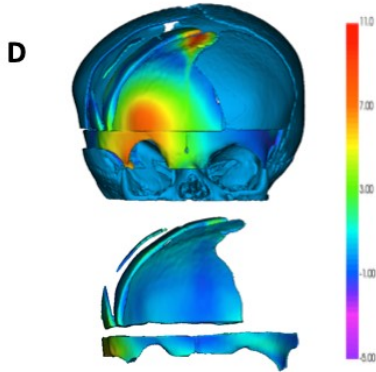
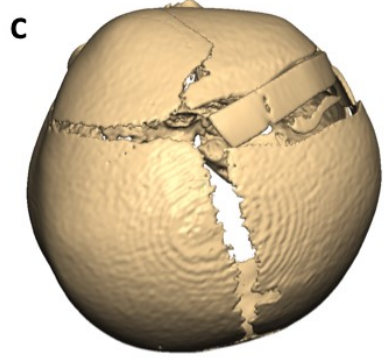
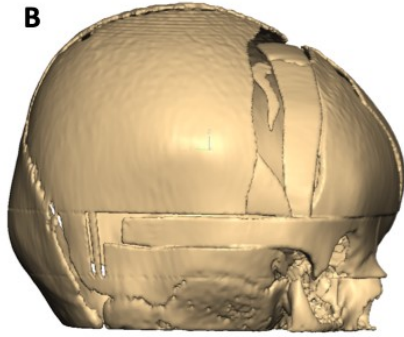
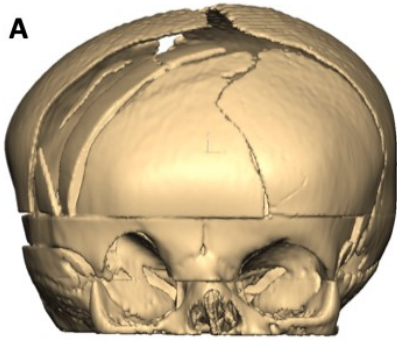


**Figure 4.26** Panel A – A view reconstruction model for iteration #15. Panel B – right lateral view of reconstruction model #15. Panel C – Bird’s eye view of reconstruction model #15. Panel D – Comparison of reconstruction model to preoperative UCS model (top), and the reconstruction model ROIs to the normal skull ROIs (bottom). Panel E – comparison of reconstruction model (grey translucent) to normal skull (green). Panel F – comparison of reconstruction model (beige) to preoperative model (grey). The contour of the preoperative UCS forehead is outlined with the dotted white line.



## **Appendices**

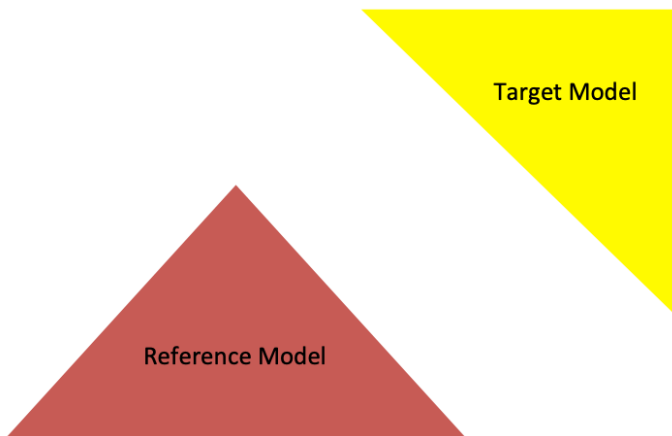
### **Appendix A: Glossary of Terms**

<b>AUC</b>	Area Under the Curve
<b>CAD</b>	Computer Assisted Design
<b>CAM</b>	Computer Assisted Manufacturing
<b>CT</b>	Computed Tomography
<b>CVR</b>	Cranial Vault Reconstruction
<b>ROI</b>	Region of Interest
<b>FB</b>	Frontal Bone
<b>FOA</b>	Fronto-Orbital Advancement
<b>SOB</b>	Supra-orbital Bar
<b>STL</b>	Stereolithography
<b>UCS</b>	Unilateral Coronal Craniosynostosis
<b>VAS</b>	Visual Analogue Scale
<b>VSP</b>	Virtual Surgical Planning

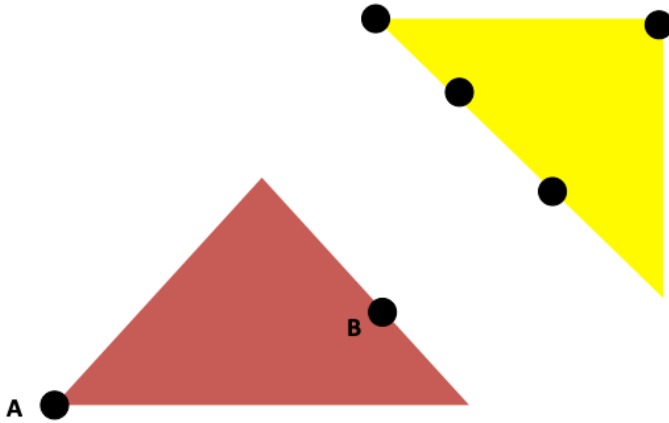
## Appendix B: Hausdorff Surface Distance Explanation

Hausdorff surface distances are used in chapters two, three, and four to quantify the difference between skull models. A common application is using Hausdorff surface distances to quantify the difference between a UCS skull and a normal skull at the frontal bones. The example below demonstrates a simplified explanation of calculating surface distances between two models.

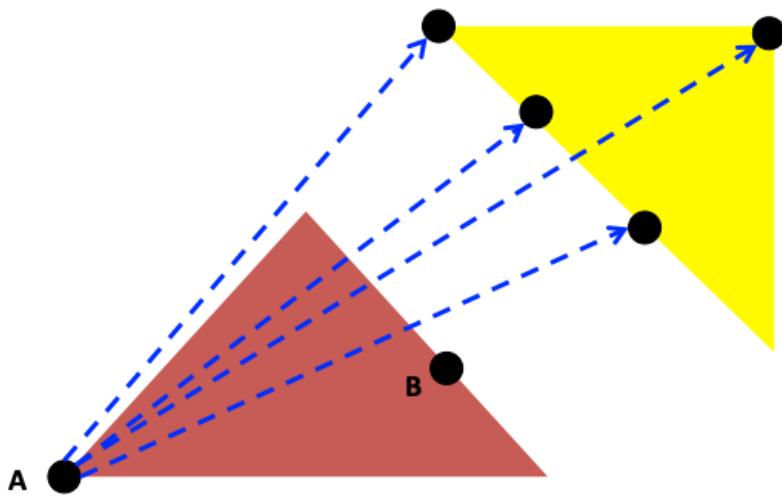
In this demonstration, the two triangles represent two different models. The red triangle is the reference model, and the yellow triangle is the target model. In a comparison between an UCS skull and a control skull, the UCS skull is analogous to the red triangle, and the control skull is analogous to the yellow triangle.



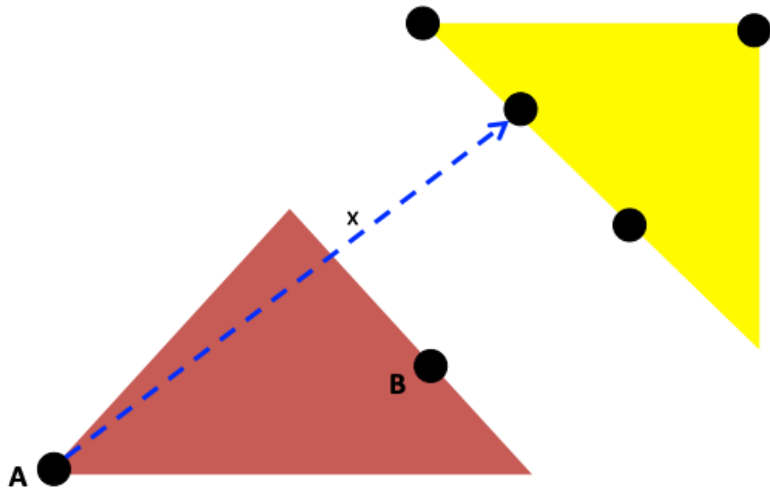
The black circles represent points along the surface of each model. Point A and point B are examples of points along the surface of the reference model or the UCS skull in the analogy. While only a few points are shown in the diagram the maximum Hausdorff surface distance is calculated after analyzing every point along the entire UCS skull, and comparing each point to every point on the normal skull. Therefore, the calculation of a maximum Hausdorff surface distance represents a global analysis of the shapes.



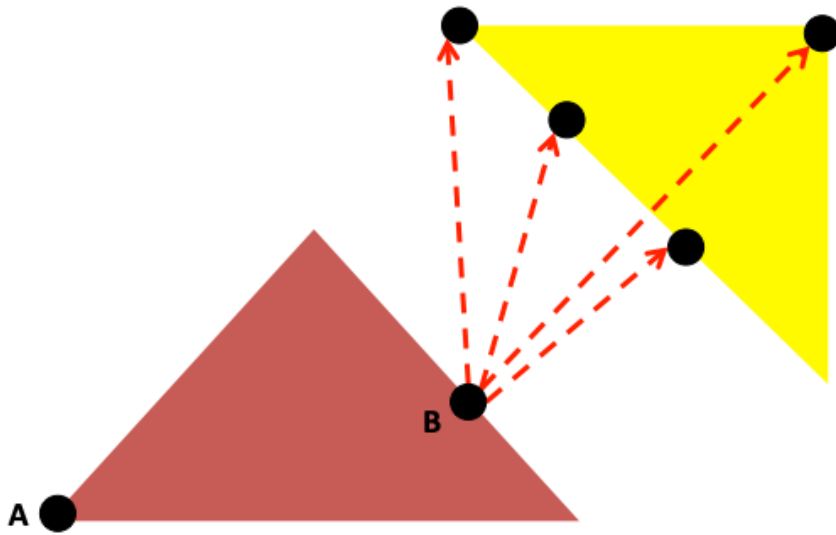
For every point along the surface of the red triangle, the distance to the yellow triangle is calculated. Point A is example of one of these points.



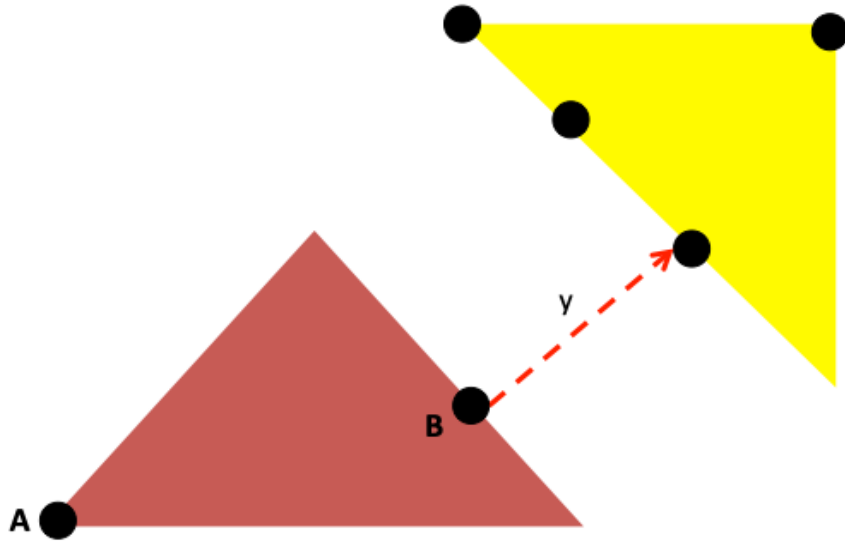
The shortest distance of all of the distances calculated is determined. In this example, that is the distance “x”.



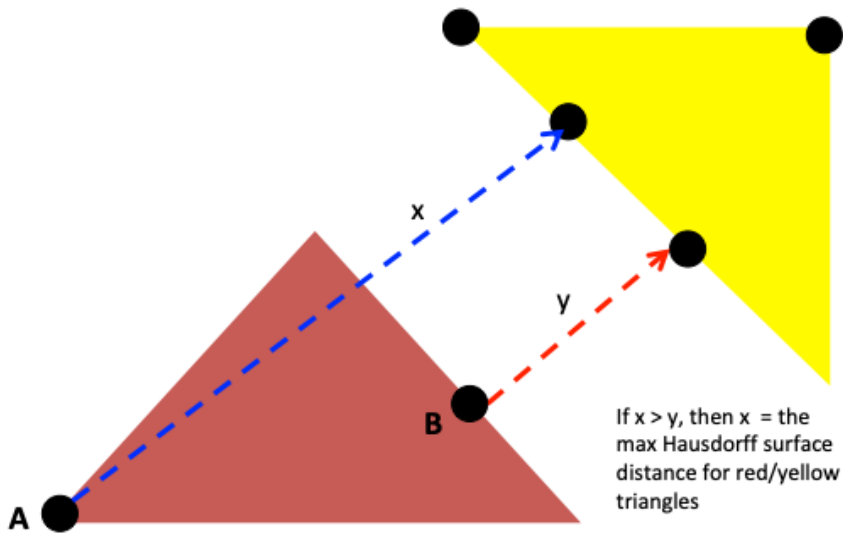
The same process is repeated for all points along the entire surface of the red triangle. Point B is example of another one of these points.



Distance “y” is determined to be the shortest distance from Point B to the yellow triangle.



This is done for every point along the surface of the red triangle. Once all the distances from all the points along the red triangle are calculated, the maximum Hausdorff surface distance is the largest of the calculated distances. In this example, if distance “x” is greater than distance “y”, then distance “x” is the maximum Hausdorff surface distance.



This method allows for the automatic determination of a single point along the UCS skull that deviates the furthest from a normal reference skull. This also eliminates the need to

standardize where measurements are taken from in terms of exact slices when examining CT data, and the need for a landmark based measuring procedure.